



UNIVERSITÀ
DEGLI STUDI
FIRENZE

DOTTORATO DI RICERCA IN FISICA E ASTRONOMIA

CICLO XXX

COORDINATORE Prof. Raffaello D'Alessandro

***Molecular clouds:
magnetohydrodynamics, gravitational collapse
and turbulence***

Settore Scientifico Disciplinare: FIS/05 Astronomia e Astrofisica

Dottoranda

Dott. Claudia Toci

Claudia Toci

Tutori

Dott. Daniele Galli

Daniele Galli

Dott. Andrea Verdini

Andrea Verdini

Coordinatore

Prof. Raffaello D'Alessandro

Raffaello D'Alessandro

Anni 2014/2017

Wild girls always shine.

Contents

Synopsys	i
List of publications	v
1 Introduction	1
1.1 The interstellar medium	1
1.2 Molecular clouds	3
1.2.1 Properties of molecular clouds	5
1.2.2 Shape of molecular clouds	8
1.3 Dense cores	9
1.3.1 From clouds to stars	12
1.4 Turbulence in molecular clouds	14
1.5 Magnetic field in molecular clouds	16
1.6 Virial analysis	18
1.7 Theories of star formation	19
2 Physical description of the interstellar medium	21
2.1 MHD approximation	21
2.1.1 Force-free fields	25
2.2 Ambipolar diffusion and magnetic reconnection	25
2.3 Basics of Turbulence	27
2.3.1 Compressible turbulence and Burgers equation	29
2.3.2 Magnetohydrodynamical turbulence	30
2.4 Outline	31

3	Equilibrium of hydrostatic filamentary structures	33
3.1	Radial density profiles of filamentary clouds	35
3.1.1	Basic equations	35
3.1.2	Isothermal parametrisations	36
3.1.3	Polytropic models	37
3.1.4	Power-law behaviour at large radius	40
3.2	Support against gravity	41
3.2.1	Thermal support	41
3.2.2	Non-thermal support	41
3.3	Radial stability of polytropic filaments	43
3.3.1	Isentropic filaments	45
3.3.2	Non-isentropic filaments	47
3.4	Summary	49
4	Equilibrium of magnetohydrostatic filamentary structures	53
4.1	Magnetized envelopes	54
4.1.1	Non-dimensional equations	56
4.2	Special solutions	58
4.2.1	Force-free fields	58
4.2.2	Constant- β solutions	59
4.2.3	Fiege & Pudritz's models	59
4.3	Cores and envelopes of magnetised filaments	61
4.3.1	Series expansion for small radii	61
4.3.2	Scale-free solutions for large radii	62
4.3.3	Force between magnetised filaments	66
4.4	Summary	68
5	Theoretical and numerical modelling of MHD collapse	71
5.1	The expanding box model for the solar wind	72
5.2	Contracting box model	74
5.3	The ECHO Code	77
5.3.1	Conservative form of MHD equations and code imple- mentations	78

6	Hydrodynamics in contracting volumes	83
6.1	Sub-structure formation in starless cores	84
6.2	Hydrodynamics in comoving coordinates	85
6.3	Linear evolution of fluctuations	86
6.3.1	WKB approximation	88
6.3.2	Special case: free-fall on a point mass	90
6.4	Application to homologous collapse	94
6.4.1	Onset of nonlinearity	95
6.5	Numerical simulations	98
6.6	Summary	99
7	Magnetohydrodynamics in contracting volumes	103
7.1	Numerical setup	105
7.2	Basic quantities	107
7.3	Static case	109
7.4	Contracting clouds simulations	112
7.4.1	Comparison with a static case	114
7.4.2	Comparison between different t_c/t_{nl}	117
7.5	Summary and discussion	121
8	Conclusions	125
8.1	Future perspectives	128
A	Appendix	129
A.1	Appendix A: physical characteristics of a plasma	129
A.2	Appendix B: ECHO code numerical scheme	131
A.3	Appendix C: Gudonov explicit scheme	137
A.4	Appendix D: Upwind Constrained Transport method	139
A.5	Appendix E: free-fall on a star	142
A.6	Appendix F: Homologous collapse of a pressureless sphere	144
	Bibliography	145

Synopsys

The problem of star formation is very complex, as it develops over several time and length scales. Many physical phenomena contribute to the collapse of a molecular cloud from the creation of the first initial density perturbation to the last pre-stellar phase. Up to date there is no complete theoretical framework able to explain all aspects of the star formation process.

Astrophysical context

Stars are forming in the interstellar medium (ISM) inside complexes of gas and dust known as *molecular clouds*, where hydrogen is almost completely in the form of H_2 . Their densest parts, called *cloud cores*, if sufficiently massive can collapse due to their self-gravity and form single protostars, binaries, or stellar clusters. This process lasts for a few million years and occurs on a time scale of the order of the free-fall time (Jeans 1902),

$$t_{\text{ff}} = \left(\frac{3\pi}{32G\rho} \right)^{1/2}, \quad (1)$$

where ρ is the gas density and G is the gravitational constant. The free-fall time is very short ($\sim 5 \times 10^5$ yr) compared to the age of the Milky Way, about 10^{10} yr.

A fundamental open question is the low efficiency of star formation observed in the Galaxy, that naturally leads to the problem of what physical processes regulate the rate at which gas turns to stars.

Similar considerations hold for molecular clouds, characterized by masses that cannot be supported only by thermal pressure. They should be contracting rapidly and forming stars at a very high rate. This is not observed, thus the slow rate of star

formation requires other sources of support against gravity. Large-scale magnetic fields and the turbulence of the interstellar gas are two natural candidates.

The magnetic field of a cloud is difficult to measure. The line-of-sight strength of the field can only be directly determined observing the Zeeman splitting of line transitions, and its plane of the sky direction can be estimated via polarization measurements of background stars, dust emission, or spectral lines. OH Zeeman observations of dark clouds suggest typical magnetic field strengths of order of $10 \mu\text{G}$ or less at the typical densities of molecular clouds, and increasing with density. This value of the magnetic field is sufficient to support clouds.

Pressure support against gravity comes from thermal and turbulent motions in addition to magnetic field pressure. Observationally, widths of lines can be used to probe the thermal and the non-thermal motions. Observations of NH_3 lines show that low-mass dense cores have subsonic gas turbulence, with velocity $\sim 0.1 \text{ km s}^{-1}$ (with a sound speed velocity $\sim 0.2 \text{ km s}^{-1}$), whereas in molecular clouds turbulent velocity is $\sim 1 \text{ km s}^{-1}$, thus supersonic.

There are two differing views of the global state of clouds. In the *quasi-static* view clouds are close to equilibrium, gravitationally bound, virialised and with long lifetimes (several 10^6 yr). The equilibrium against self-gravity is provided by the magnetic field and molecular clouds evolve under gravity, quasi-statically. This process is rather inefficient, in agreement with the low rate of stellar birth. The *dynamic* point of view emphasises the role of supersonic turbulence and lack of equilibrium. In this picture clouds form without reaching an equilibrium in lifetimes of the order of 10^6 yr . The formation of structures is therefore relatively fast and driven by the turbulent enhancement of density perturbations. However, their distribution leads to a low efficiency of star formation.

Recent results from the infrared ESA satellites Herschel (André et al. 2014) and Planck (Planck Collaboration 2016) have revealed that star forming regions are intricate networks of intertwined filaments extending over parsec scales¹(see fig. 1), while polarimetric measurements have shown that the Galactic magnetic field has a well-defined mean direction on the scales of molecular clouds. Star formation takes place when the individual filaments composing a molecular cloud accumulate enough mass per unit length (by accretion from the ambient medium), become gravitationally unstable and fragment into cores, that eventually collapse

¹ $1 \text{ pc} = 3.26 \text{ light years (l.y.)}$ or $3.086 \times 10^{16} \text{ m}$.

into stars and stellar clusters.

Summary of the thesis

After a first part of introduction on the main features of the interstellar medium, where we focus on the properties of molecular clouds and cores, we present the main concepts of plasma physics theory, magnetohydrodynamics and turbulence. We then show original work performed in the analysis of the stability and contraction of molecular clouds, underlining partial conclusions for each argument explored. Finally, we summarise our results in the conclusions of the thesis.

In particular, an overview of the physical characteristics of the interstellar medium is given in Chapter 1. Chapter 2 introduces the physical theories and the equations of magnetohydrodynamics and turbulence applied to the interstellar medium. In the framework of the quasi-static theory is then important to characterise the properties of the stability of filaments in cylindrical symmetry both in an hydrodynamical (HD) and magnetohydrodynamical (MHD) case. In Chapter 3 we show how an isothermal equilibrium model fails to represent the observed radial density profiles of filamentary molecular clouds, underlining the need for other contributions to the stability of the cloud. This support can come from non-thermal motions (turbulence) or from the magnetic field (Toci & Galli 2015a). In Chapter 4 we demonstrate that the introduction of an helical magnetic field (as suggested by observations) can both squeeze or sustain the filament, according to the ratio between the toroidal and the poloidal component of the magnetic field (Toci & Galli 2015b).

The quasi-static and the dynamic view predict different life times for a molecular cloud, thus a study focusing on contractions that occur on different timescales could give results to confront with both the above scenarios. The timescales involved in the problem are the *contracting time*, which induces a growth of fluctuations, the *non-linear time*, which is related to turbulent damping, and the free-fall time, which characterise the gravitational instability (also known as Jeans time). In Chapter 5 we generalise a formalism already known in the literature, the *expanding box model* (Grappin et al. 1993, Verdini & Grappin 2016), that has been extended to the case of a generic collapse with a diagonal metric. We implement the latter metric on the numerical ECHO code to perform 3D numerical simula-

tions. The metric mimics the contraction due to the self-gravity. However, there are two main limitations: the absence of a *Poisson solver* to follow the effect of the gravitation instability, and of feedback effects due to pressure.

In Chapter 6 we show a first analysis made in the HD case, where we perform an analytical study of the growth of density fluctuations in a core during a gravitational collapse. We point out that generically, the non-linear time scale associated with dissipative processes is shorter to the time-scale related to the collapse. This implies that, even if the density fluctuations are amplified during the collapse, they are smeared out by the non-linear effects before being gravitationally unstable. We then verified our theoretical predictions with 3D HD simulations with 512^3 grid points performed using the ECHO code (Toci et al. 2017).

In Chapter 7 we show 3D simulations with 512^3 grid points performed using the ECHO code in MHD cases. We study the collapse along the mean magnetic field direction of a fluid element. This configuration is useful to understand the mass accretion on filaments (or an anisotropic collapse) which occur along the mean magnetic field. Our study focuses on the temporal evolution of physical quantities of a fluid element, in particular on the ones that can be observed in molecular clouds (velocity fluctuations, mean density...). Our results seem to indicate that the ratio between the non linear time t_{NL} and the gravitational time t_c of the system is the key-parameter that sets the time evolution. Indeed, in contractions where $t_c < t_{NL}$ the behaviour of turbulence is "frozen" and fluctuations in the system are amplified without any dissipation effect. If $t_c \sim t_{NL}$ in a first phase fluctuations are not amplified but sustained. However, after some time the size of the fluid element becomes sufficiently small and the effect of contraction dominates. In the case where $t_c > t_{NL}$ dissipation dominates in a first phase and fluctuations decay, however there is always a time where the contraction effect dominates. We also note that, during a contraction, the pressure effect associated with non thermal motions becomes quickly comparable with the thermal pressure. When the two are similar, our model is no more realistic.

Finally, in Chapter 8 we summarise the results we found in previous Chapters and we present some overall conclusions. In particular, one result is that the non-thermal pressure contribution we found in MHD simulations is compatible with the theoretical expectations of quasi-static models. We also outline some guidelines for future improvement.

Publications

Refereed papers

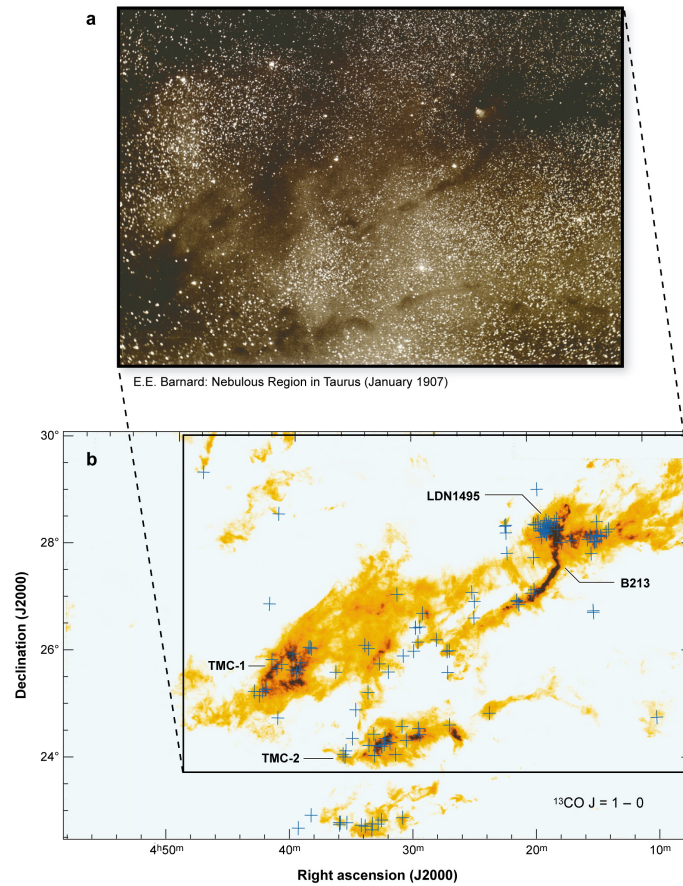
3 papers as 1st author on MNRAS.

- **Toci, C.**, Galli, D.
Polytropic models of filamentary interstellar clouds - I. Structure and stability
2015, MNRAS, 446, 2110T
- **Toci, C.**, Galli, D.
Polytropic models of filamentary interstellar clouds -II. Helical magnetic fields ,
2015, MNRAS, 446, 2118T
- **Toci, C.**, Galli, D., Verdini, A., Del Zanna, L., Landi, S.
Sub-structure formation in starless cores ,
2017, MNRAS, DOI: <https://doi.org/10.1093/mnras/stx2790>

Contributed papers

2 contributions as 1st author on *Il Colle di Galileo*, 1 proceedings on Mem. S.A.It.

- **Toci, C.**, Galli, D.
Polytropic models of filamentary molecular clouds: structure, stability and magnetic fields
Mem. S.A.It proceedings, accepted
- **Toci, C.**, Galli, D.
Space spaghetti in magnetic sauce
2015, *Il Colle di Galileo*, DOI: http://dx.doi.org/10.13128/Colle_Galileo-17690
- **Toci, C.**, Stanga, R.
Binational Heraeus Summer School: Astronomy from 4 perspectives IV - Origins of stars and planets
2017, *Il Colle di Galileo*, DOI: http://dx.doi.org/10.13128/Colle_Galileo-20562




 Bergin EA, Tafalla M. 2007.
Annu. Rev. Astron. Astrophys. 45:339-96

Figure 1: (a) Photographic image of the Taurus molecular cloud (Barnard 1919); (b) ^{13}CO (J=1-0) integrated emission map of the same region obtained using the Five College Radio Astronomy Observatory (FCRAO). Blue crosses mark the location of known stellar and prestellar objects and the emission colour scale ranges from 0.5 to 10 K km s^{-1} (Goldsmith et al. 2008). Figure taken from Bergin & Tafalla (2007).

1

Introduction

In our Milky Way and in all galaxies, molecular clouds are the places where stars form. From the formation of the first bound structures in the Universe to the formation of planetary systems like our Solar System, all these processes are connected to the process of star formation. In the last years, the studies of the nearest star forming clouds (i.e Taurus [Palmeirim et al. 2013](#) or [Henshaw et al. 2017](#)) with the Herschel Space Observatory, the millimetre telescopes like IRAM (30 m) and the interferometers like NOEMA and the Atacama Large Millimeter Array have provided detailed information on the initial and boundary conditions of this process in a wide range of size scales (from few hundreds pc to the milli-pc scales) and wavelength (radio, IR, mm, ..). The all-sky map of the polarized emission from dust at submm wavelengths made by the Planck satellite ([Planck Collaboration 2016](#)) has provided new insight into the structure of the Galactic magnetic field and the properties of dust. Significant progress has been made also in the theoretical interpretation and modelling of the observations thanks to the development of numerical simulations and analytical tools.

1.1 The interstellar medium

The ISM is an important component of galaxies, and represents $\sim 5 - 10\%$ of their masses. It is defined as everything that is in between the stars ([Draine 2011](#)). The ISM is composed of multiple phases, distinguished by whether matter is ionic, atomic, or molecular, and the temperature and density of the matter; it contains also dust and cosmic rays. The most abundant chemical specie is hydrogen, both atomic and molecular, helium and a few percents of heavier elements.

Most of the volume of the ISM is filled by ionized gas, but its total mass is $\sim 25\%$ of the total gas mass (Klessen & Glover 2016). Most of the mass is in regions of neutral atomic gas (H, He) or molecular gas (H_2), in the form of dense molecular clouds that occupy only 1-2% of the total volume of the ISM. The thermal and chemical state of the ISM are described using a number of distinct phases. Field et al. (1969), assuming thermal equilibrium, found two thermally stable solutions: one corresponding to cold, dense ($\sim 20\text{--}50\text{ cm}^{-3}$) gas with $T \sim 100\text{ K}$, now called Cold Neutral Medium (CNM), and another corresponding to warm, diffuse gas with density $\sim 20\text{--}50\text{ cm}^{-3}$ and $T \sim 10^4\text{ K}$ that is now called Warm Neutral Medium (WNM). This model was extended by McKee & Ostriker (1977) who found that supernovae exploding in the ISM would create large, ionized bubbles with very hot gas ($T \sim 10^6\text{ K}$). This hot gas is known as Hot Ionized medium (HIM). Observation for another phase, the Warm Ionized Medium, came from different phenomena, i.e. optical emission lines produced by ionized species such as O^+ and N^+ (Reynolds et al. 1973). This ionised gas has a density of $\sim 0.2\text{--}0.5\text{ cm}^{-3}$ and a temperature of $\sim 10^4\text{ K}$. The last phase is the cold, molecular phase. Its density is 10^3 cm^{-3} and it has a small fractional ionisation $\sim 10^{-6}$ (Caselli et al. 1998). The distribution of this molecular gas in our Milky Way is of interest, as star formation occurs in these regions.

The large range of temperatures suggest that heating and cooling are important physical processes in the ISM. The supernova explosions produce the hottest gas that heats up the ISM by means of shock waves. A second heating mechanism is the ultraviolet radiation of young stars embedded in their parental clouds. Finally, the ionization losses of the flux of cosmic rays are important sources of heating and ionisation both for the diffuse neutral gas and for the gas in molecular clouds. Other dynamical sources of heating are gravitational collapse, ambipolar diffusion heating and turbulent heating.

Radiation is the most efficient way in which the thermal energy of the gas is lost. For high temperature ($10^4\text{--}10^7\text{ K}$) the emission is due to bound-free transition of hydrogen, helium and other elements. Between 10^3 and 10^4 K , where hydrogen is ionised by hot, young stars, the main cooling mechanism is line radiation, the resonance lines of hydrogen or the forbidden line of the oxygen. Below 10^3 K , molecules and interstellar dust play important roles in determining the temperature of the gas. There are two main mechanisms: the first one is the molecular line emission associated with ro-vibrational transitions of asymmetric molecules such as CO, the second one is the re-radiation of the radiation absorbed by the dust grains.

Information on the nature of dust come from the measurements of the spectral shape of the extinction curve that it produces. As a first approximation, individual dust grains

absorb only those photons with wavelengths smaller or comparable than the physical size of the grain but are transparent at longer wavelengths. Measurements of the extinction curve in the Milky Way show that it extends over a large range of wavelengths (Draine 2011). This implies that there must be a wide range of grains present in the ISM. Mathis et al. (1977) reproduced the extinction curve with a mixture of spherical graphite and silicate grains with a power law size distribution between 50 nm and 0.25 μm . Recent studies have improved on this simple description. Another important role of dust grain is to act as a catalyst for the formation of complex molecules (Caselli & Ceccarelli 2012). At a temperature below 10^3 K dust grains survive to photoevaporation and can perform different functions. First of all they absorb ultraviolet and optical light, shielding molecules from the interstellar flux of dissociating radiations.

Neutral hydrogen (HI) is observed for its emission at a wavelength $\lambda = 21$ cm. This line has a very small transition probability, thus it is very narrow. The measure of its Doppler shift provides the total column density of the neutral hydrogen along the line of sight. The HI absorption measurements provide information about the small-scale structure and the velocity dispersion. Many molecular clouds seem to be embedded into massive halos of atomic hydrogen. These HI superclouds that surround GMC have mass ranges $\sim 10^6 - 10^7 M_{\odot}$ and a density of $\sim 10 \text{ cm}^{-3}$ (Elmegreen & Elmegreen 1987).

1.2 Molecular clouds

Molecular clouds are the densest and coldest phase in the Galactic interstellar medium. Gas in these regions is too cold to radiate at visible wavelengths ($T \sim 10$ K), but may be detected through its radio emission in trace molecules such as CO. As their name implies, their masses are mostly made by molecular hydrogen (H_2) and He ($\sim 26\%$), in a range between $10^2 M_{\odot}$ for the smaller clouds and $10^7 M_{\odot}$ for the giant molecular clouds (Dobbs et al. 2014). Molecular hydrogen dominates the masses rather than atomic hydrogen (typical of the rest of the ISM) due to the fact that they are opaque to the UV radiation that elsewhere dissociates the molecules. There is also an external envelope made by H which is warmer and less dense. The first observation has been made with the $^{12}\text{CO} (1-0)$ line at 2.6 mm (Wilson et al. 1970) while subsequent observations at higher angular resolution of high density tracers such as NH_3 , CS, and HCN revealed the denser regions in which stars form (Myers & Benson 1983). Recent observations have shown that the evolution of the chemical complexity is tangled with all the stages of star formation (Caselli & Ceccarelli 2012).

Continuum emission from dust and emission/absorption lines that are emitted by

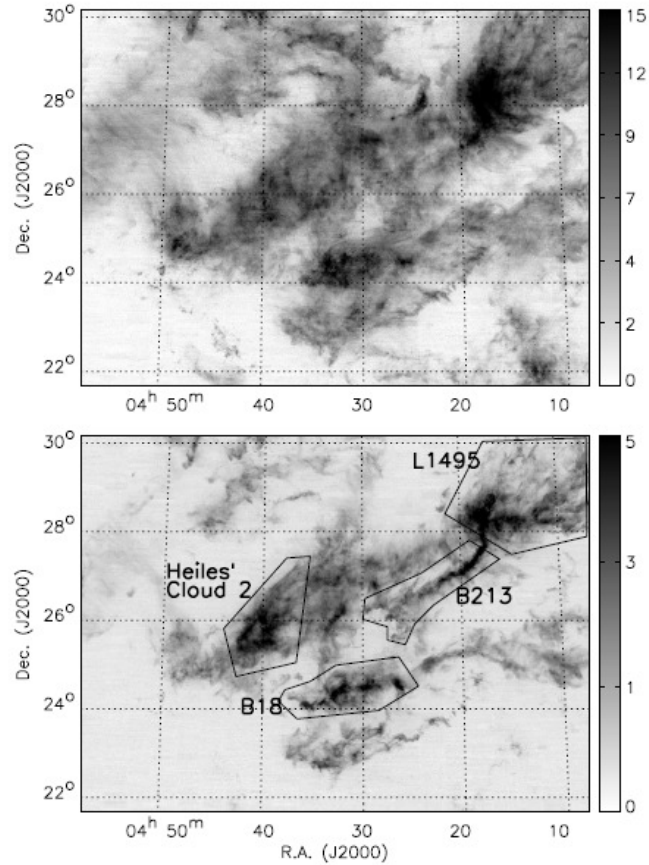


Figure 1.1: Integrated Intensity Images for ^{12}CO (top) and ^{13}CO (bottom). The images are obtained over -5 to 20 km s^{-1} and 3 to km s^{-1} for ^{12}CO and ^{13}CO , respectively. The shading bar on the right shows the integrated intensity scale in K km s^{-1} . The ^{13}CO figure, (Narayanan et al. 2008) also shows overlay outlines of a few well-known regions in Taurus.

molecules such as C, N and O are the main observational tracers of clouds structure because cold H_2 is difficult to observe for its lack of observable rotational transitions. The observations of CO are important also because it can be assumed that wherever CO molecules exist, H_2 molecules should also exist, and hence CO is tracing also the molecular hydrogen. Indeed the excitation process for the CO molecules is via collision with H_2 , thus the density of CO provides a measure of the density of H_2 in clouds. CO observations are sensitive to gas at relatively low density ($n < 10^5 \text{ cm}^{-3}$), since CO freezes out onto dust grains in dense regions, and has a dynamical range of two decades in column density.

For higher column densities the gas becomes colder and then lines become optically thick. The best candidates to map higher density regions of molecular clouds are optically thin emissions lines of isotopes of more common molecules, like ^{13}CO and C^{18}O . Fig. 1.1 shows CO and ^{13}CO maps of the Taurus molecular clouds (Narayanan et al. 2008). The $^{12}\text{CO } J = 1 - 0$ integrated emission is mostly diffuse, while the $^{13}\text{CO } J = 1 - 0$ emission is mostly distributed within high-contrast filaments. Regions where the dust effectively blocks the light from background stars are traditionally known as *dark clouds*.

1.2.1 Properties of molecular clouds

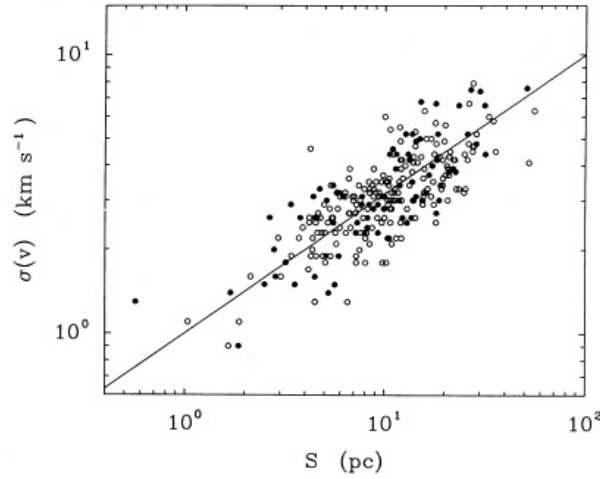


Figure 1.2: Relation of size (S) and velocity dispersion (σ), from the Solomon et al. (1987) study of 273 molecular clouds in the MilkyWay. This fit has a power index of 0.5, the original figure from (Larson 1981) has a power index of 0.38.

Molecular clouds and star formation are strongly correlated on different scales. On the scale of the galaxy, Schmidt (1959) derived an empirical scaling relation between the average surface density of star formation, Σ_{SFR} , and the average surface density of the gas, Σ_{gas} . Kennicutt (1989) found, assuming a constant H_2/CO ratio, in a wide number of galaxies a power-law correlation,

$$\Sigma_{SFR}(M_{\odot} \text{ yr}^{-1} \text{ pc}^{-2}) \propto (\Sigma_{gas}(\text{g pc}^{-2}))^n, \quad (1.1)$$

with an index $n \sim 1.4 \pm 0.15$. There is also a correlation between the SFR and the H_2 density that is currently under investigation (Dobbs et al. 2014). The cloud mass spectrum

is well reproduced, for masses $M > 10^4 M_\odot$, with a power-law $dN/dM \sim M^{-\gamma}$; Solomon et al. (1987) found values for γ in the range 1.5 - 1.8, implying that most of the mass is in large clouds. They also measured the sizes of molecular clouds and evaluated their surface densities $\Sigma_{GMC} \sim 150 M_\odot \text{ pc}^{-2}$ (assuming a fixed CO to H₂ conversion factor). This value can be function of the environments.

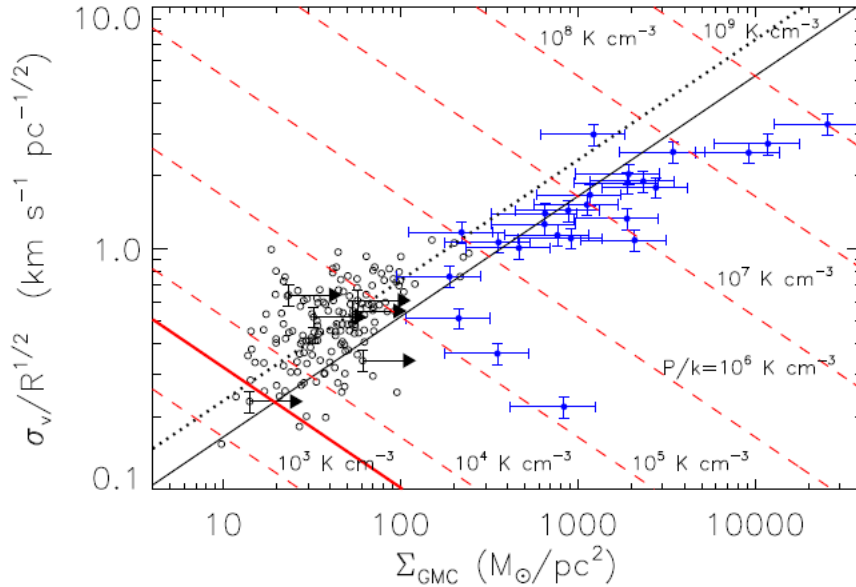


Figure 1.3: The variation of $\sigma/R^{1/2}$ versus the surface density Σ_{GMC} for the Milky Way's GMC from Dobbs et al. (2014). Open circles are points from Heyer et al. (2009) while the blue points are massive cores from Gibson et al. (2009). The solid and dotted black lines are gravitationally bound and marginally bound objects respectively. Red dashed lines are loci of constant turbulent pressure. The mean thermal pressure of the ISM is the solid red line.

From a dynamical point of view molecular clouds are characterised by line-widths wider than the ones resulting from the excitation temperature of the molecules (except on the scale of isolated proto-stellar cores). In addition, observations of molecular clouds seem to indicate correlations between various properties such as clump size, velocity dispersion and mass. Molecular-line studies revealed non-Gaussian line shapes and velocity differences across clouds due to supersonic motions. These motions are inferred to be turbulent from the lack of systematic patterns like rotation, expansion, or infall (there are not P-Cygni line profile observed, Heiles & Katz (1976), and from the existence of a system-

atic power-law relation between the velocity dispersion inside a cloud σ and its physical size L

$$\sigma(\text{km s}^{-1}) = 1.10 L(\text{pc})^{0.38} \quad (1.2)$$

(Larson 1981), which is reminiscent of the classical Kolmogorov law of (incompressible) turbulence (see Section 1.4 and Section 2.3). Solomon et al. (1987) found for the Larson law a power index of ~ 0.5 (see Fig. 1.2). Larson (1981) also noted, using data from different molecular clouds surveys, that the density ρ scales with the cloud size L as $\rho \sim L^\alpha$, too. The value of the exponent is $\alpha \approx -1.15 \pm 0.15$ (Falgarone et al. 1992). A more recent study (Heyer et al. 2009) found an extension of the Larson law,

$$\sigma(\text{km s}^{-1}) = 0.7(\Sigma_{\text{GMC}}/100M_\odot\text{pc}^{-2})^{1/2}(R/1\text{pc})^{1/2}, \quad (1.3)$$

where the velocity dispersion depends on the physical radius R and from the surface density of giant molecular clouds, Σ_{GMC} (see also Fig. 1.3). The kinematics of clouds has a dependence on density: models of compressible supersonic turbulence show that the denser the gas the slower is its velocity. This might arise from the convergence of flows (Padoan et al. 2001). The densest regime corresponds to the dense cores, which are known to have subsonic velocity dispersion. Therefore, dense cores seem to stay at the bottom of the hierarchy of cloud kinematics and to represent structures dominated by dissipation of turbulence (Goodman et al. 1998)

Molecular clouds are well-shielded from UV radiation and this implies that the temperature remains remarkably constant over several orders of magnitude in density (Glover et al. 2015). This has as a consequence that a simple isothermal equation of state is a good approximation for the gas, where pressure P and density ρ are linearly related, with the constant sound speed c_s as a factor, $P = c_s^2 \rho$. The assumption of isothermality breaks down when the gas becomes optically thick and cooling is no more efficient. In the local ISM, this occurs for values of the density above $\sim 10^{10} \text{ cm}^{-3}$ (Klessen & Glover 2016). The equation of state then changes from isothermal to adiabatic with polytropic exponent $\gamma_p = 7/5$.

Despite their low temperature, molecular clouds are sufficiently dense to make their pressure exceed the average ISM pressure by at least an order of magnitude. The typical ISM pressure is around $10^{-13} \text{ erg cm}^{-3}$ (Bowyer et al. 1995), while at a temperature of 10 K and a density of $\sim 10^3 \text{ cm}^{-3}$, the pressure of a typical molecular cloud is larger than $10^{-12} \text{ erg cm}^{-3}$. In order to explain the high pressure observed in GMCs gravitational confinement is traditionally invoked (Williams et al. 2000). However, if only thermal pressure opposes the gravitational attraction given by their large masses, they should be

collapsing very efficiently forming stars in a free-fall time ($\sim 5 \times 10^5$ yr). This is not the case.

A common feature of dark clouds is that they show a hierarchical structure, with smaller subunits appearing within large ones when observed with increasing spatial resolution. To characterize this structure, two different approaches have been generally adopted in the literature, depending on whether the discrete or the continuous nature of the structure is considered. In the first approach, clouds are composed of subunits, referred to as clumps and defined as coherent regions in position-velocity space that may contain significant substructures (Williams et al. 2000). The second one describes clouds as self-similar, at least over some range of scales, thus fractal geometry can be applied. However this hypothesis breaks down at large scales, where the presence of well defined structures like filaments indicates a deviation from self-similarity. Also at small scales, where gravity dominates, this picture is expected to break down. Williams et al. (2000) have proposed a characterisation of structure in terms of clouds, clumps and cores, with clumps defined (as above) by their velocity coherence and cores defined as gravitationally bound, single-peaked regions out of which stars form.

1.2.2 Shape of molecular clouds

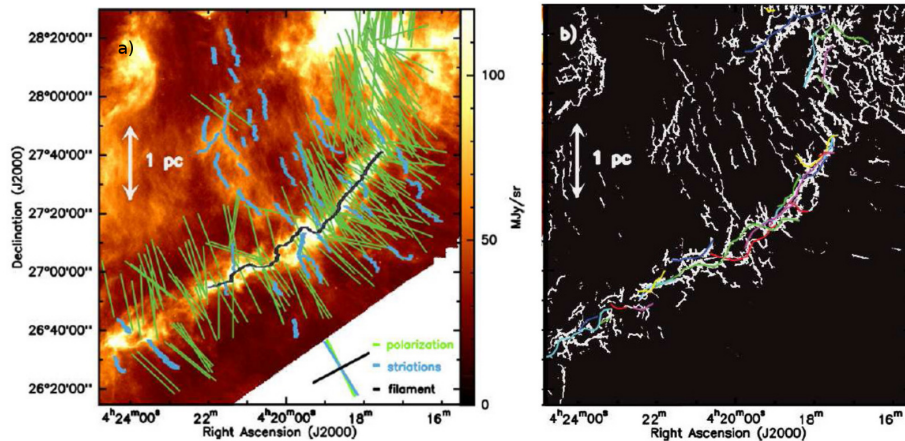


Figure 1.4: Fig. a) Optical and infra-red polarisation vectors tracing the magnetic field orientation displayed over the Herschel/SPIRE 250 μ m image of B211/B213/L1495 region in Taurus. Fig. b) Structure of the Herschel/SPIRE 250 μ m image of B211/B213/L1495 continuum emission. Note that the faint striations are perpendicular to the main filament. From André et al. (2014).

In general, dark clouds have highly irregular edges, and their overall appearance is filamentary and often wind-blown. The presence of long, well-defined filaments was emphasized already a century ago by Barnard in his studies in the Taurus nebula (Bergin & Tafalla 2007). Their importance for star formation has been addressed by many authors with observations, simulations and theoretical models. The Herschel results (André et al. 2014) have pointed out the key role of these structures in star formation process, revealing an intricate network of filamentary structures in every clouds over spatial scales from the entire cloud complexes (≥ 10 pc) to the size of dense cores (≤ 0.1 pc). Filaments appear to be very long, ~ 1 pc or more and quite linear.

Some filaments seem to be associated to a distinct population of smaller filaments (Arzoumanian et al. 2011). The denser, self gravitating filaments tend to be perpendicular to the direction of the local magnetic field (see i.e. Fig. 1.4) while the low-density filaments (also called *striations*) tend to be parallel to the local magnetic field and appear unbounded (Planck Collaboration 2016). Detailed studies, i.e (Arzoumanian et al. 2011), suggest that radial density profiles of the dense, self-gravitating filaments are well reproduced by a flat inner part $\varpi_{flat} = (0.03 \pm 0.02)$ pc and a power-law envelope extending $\sim 10\varpi_{flat}$ until they merge with the surrounding material. Filaments intersections can provide local regions of higher column densities, triggering clustered star formation or high mass star formation.

Gas in filaments is not static, material is falling on the filaments from the surrounding medium, as observed with the CO emission i.e in B211/B213 in the Taurus cloud, with typical velocities of $\sim 0.5 - 1$ km s^{-1} (Palmeirim et al. 2013). The filaments themselves appear to feed material into hubs where star formation is ongoing, as observed in the Serpens South, with infall rates of $10^{-4} - 10^{-3} M_{\odot} \text{ yr}^{-1}$ (Schneider et al. 2010).

1.3 Dense cores

Low-mass dense cores are localised density enhancements of cloud material and are associated with the earliest phases of low-mass star formation. Optically they appear as small, roundish and dark nebulosities (often named in the literature Bok globules or Barnard objects, see i.e *Barnard 68* in Fig. 1.5). They are called "protostellar" or "starless", depending on whether they do or do not contain a protostellar object. Such cores are dense zones of molecular gas of relatively high density which represent the physical and chemical conditions of interstellar gas just after or prior to localized gravitational collapse. (Bergin & Tafalla 2007).

Due to the fact that they are dense objects, they can be identified observationally in

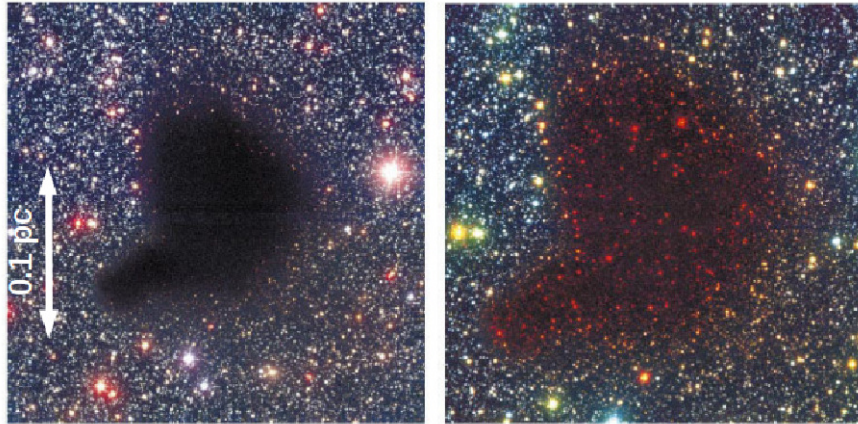


Figure 1.5: Left) B,V,I band ($0.44 \mu\text{m}$, $0.55 \mu\text{m}$, $0.90 \mu\text{m}$, $7' \times 7'$) of the dark molecular cloud B68 taken with ESO's Very Large Telescope (VLT). The cloud is seen in projection against the Galactic bulge. At these optical wavelengths it is completely opaque due to the extinction of background starlight caused by dust. Right) B,I,K band ($2.2 \mu\text{m}$) image. The K band image was obtained with ESO's New Technology Telescope (NTT). At near-IR wavelengths the cloud becomes transparent. From Alves et al. (2001)

molecular clouds as compact opaque objects in optical/infrared light or in sub-millimetre or millimetre continuum emission. In the literature they have been called *dense cores* because they showed emission from NH_3 , excited at densities of $> 10^4 \text{ cm}^{-3}$ (Myers & Benson 1983).

Cores can vary widely in morphology or shape. They can be rather elongated or roundish. Their density structure is typically estimated through the analysis of dust emission or absorption. Three main techniques have been used in the literature: (a) near-IR extinction mapping of background starlight, (b) mapping of millimetre and submillimetre dust continuum emission and (c) mapping of dust absorption against the Galactic mid-IR background emission. A main characteristic of their density profiles is a central flattening.

A simple theoretical model for their density profile is the *Bonnor-Ebert* (BE) spherical profile (Bonnor 1956), a solution of the equation of hydrostatic isothermal equilibrium, characterised by a "plateau" of quasi-constant density n_c at small radii and a power-law r^{-2} decrease at large radii. This approximation often (but not always) provides a good fit to the data (see i.e Fig. 1.6). This could suggest that cores are isothermal spheres supported only by thermal pressure and confined by outer medium. However, several evidences show that even if thermal pressure is an important ingredient in core structure, it is not the only one. Cores are indeed seldom spherical, but they appears in projection

as elliptical objects. In addition, the observed density contrast between the central and the edge density exceeds the maximum value of ~ 14 allowed for stable BE profile, thus other forces are needed. Finally, the pressure required exceeds the observed thermal (plus subsonic non-thermal) pressure of cores, indicating either the presence of other forces or the lack of equilibrium. Magnetically-dominated models produce equilibrium configurations with flattened density profiles and an approximate r^{-2} power-law behaviour at large radii (Lizano & Shu 1989). However, they seem to require a magnetic field strength of $\sim 50 - 150 \mu\text{G}$, significantly higher than observed (we will discuss magnetic fields in Section 1.5). More than 70% of the pre-stellar cores found by Herschel are inside filaments and this suggests that dense cores form mainly by fragmentation along filaments (André et al. 2014).

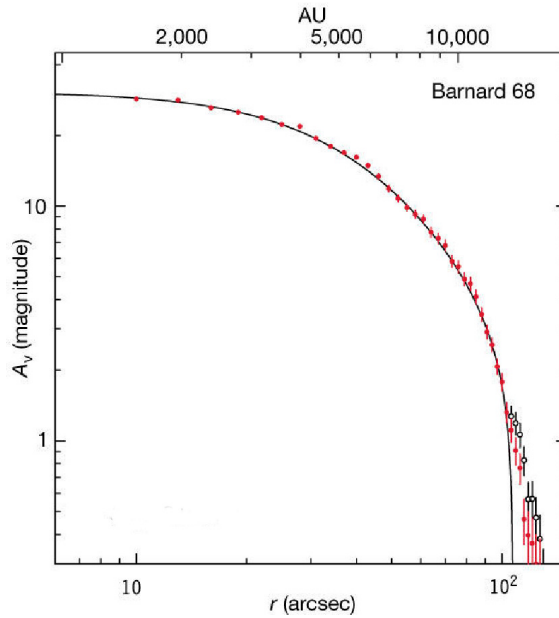


Figure 1.6: Dust column density of the core *Barnard 68* expressed in terms of magnitudes of visual extinction, A_v . The red circles show the data points for the averaged profile of a sub-sample of the data that do not include the cloud’s southeast prominence. The open circles include this prominence. The solid line represents the best fit of a theoretical Bonnor-Ebert sphere to the data. From Alves et al. (2001)

In the ISM the temperature of the dust component and the gas component are in general different. In the case of a core, the kinetic temperature of dust and gas components is regulated by the equilibrium between heating and cooling. At typical core densities ($> 10^4 \text{ cm}^{-3}$), gas and dust are coupled thermally via collisions, thus the two temperatures

are expected to be equal. The dust temperature is evaluated using the balance between the heating by the interstellar radiation field and the cooling due to thermal radiation in the far-IR emitted by grains. Recent studies (see, e.g., André et al. 2014) have shown that the dust temperature T_d falls from ~ 12 K on the exposed surface to ~ 7 K at very small radii, exhibiting an inverse gradient. Also the gas temperature is determined by the balance between heating and cooling. For lower densities, heating is mostly due to the ionisation of cosmic rays, while cooling is due to line radiation from molecules as CO and fine-structure atomic lines. The value of the kinetic temperature T_k , derived from NH₃ transitions, is ~ 10 K. For the higher densities also dust-gas coupling collisions become important and this process can additionally heat or cool the gas according to the difference between the component's temperature (linked to the external UV field). Finally, in contrast with the supersonic velocity dispersion of MC, dense cores have low-velocity internal motions.

1.3.1 From clouds to stars

Prestellar cores are the direct precursors of stars. The process that starts with molecular clouds and ends with stars can be subdivided into observationally different phases (Shu et al. 1987, Andre et al. 2000). A schematic view is reported in Fig.1.7. The first stage is related to the fragmentation of molecular clouds into gravitationally bounded cores, which are supported against gravity by pressure, magnetic field and turbulence. This process possibly involves ambipolar diffusion, dissipation of turbulence or outside impulse (Fig.1.7(a)). When a condensation becomes gravitationally unstable it collapse isothermally forming an opaque, isothermal protostar at the center, with a density of $\sim 10^{10}$ cm⁻³. Material becomes optically thick, thus the heat generated by the collapse is no longer efficiently radiated away. The central region begin to eats up and the collapse pauses. When the temperature reaches ~ 2000 K, molecular hydrogen start to dissociate, absorbing energy. The core becomes unstable again and collapses, building up its mass by accretion from the infalling surrounding medium. Outside the region where the accretion occurs, the material is still hydrostatically supported. Since the inflow region expands outwards, this process is called *inside-out* collapse (Shu 1977). Most of the released gravitational energy is used to dissociate H₂ molecules, then the temperature rises slowly. When all the H₂ is dissociated, the temperature rises and pressure gradients stops the collapse. This second hydrostatic object is the true protostar (Fig.1.7(b)). This process lasts $\sim 10^6$ yr.

The core enters into the *class 0* phase, in which the central object increases its mass by the accretion of infalling material from the outer part. During this phase, material with

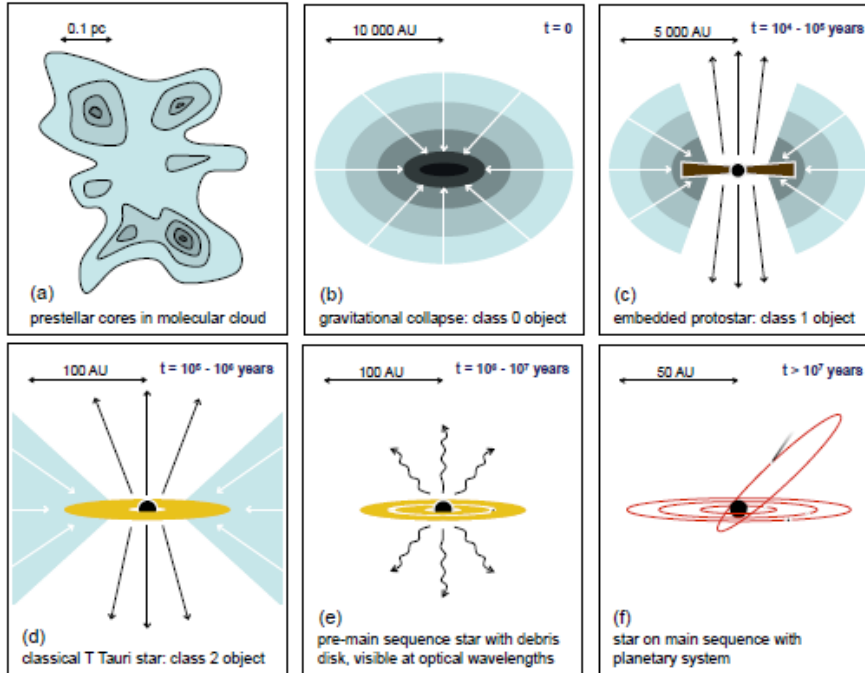


Figure 1.7: View of the star and planet formation process. From Glover et al. (2015)

higher angular momentum starts to form a disk orbiting the protostar. The gas is then transported inwards by viscous processes. In this phase both stars and disk are embedded into their parental cloud, whose mass exceeds the total mass of protostar and disk together. The main contribution to the luminosity comes from accretion and this object is observable at sub-millimetre and millimetre wavelength. This phase lasts for $\sim 3 \times 10^4$ yr (Fig. 1.7(c)).

Later on, protostellar jets start to clear up the envelope. These powerful, bipolar outflows eject only a small fraction of the accreted material. They are believed to remove the exceeding angular momentum of the infalling material. This is called *class I* phase, when the object becomes observable also into optical wavelength and in which the envelope mass is smaller than the star/disk mass. It lasts for $\sim 10^6$ yr.

In the *class II* phase the envelope is dissipated (accreted or dispersed by the outflows, Fig. 1.7(d)). The protostar no longer accretes but it enters into the *pre-main sequence* contraction phase, surrounded by a thin disk (with mass $\sim 10^{-3}$ of the star mass). In this stage planets are believed to form. This phase is also called T-tauri phase. As the time

goes on, the disk is more and more depleted and only a tenuous dusty disk remains (*Class III* phase, Fig.1.7(e)). This disk can survive until the stellar main-sequence phase ($\sim 10^7$ yr) (Fig.1.7(f)).

1.4 Turbulence in molecular clouds

Turbulence is a multiscale phenomenon that transfers energy from large to the smaller scales, with the bulk of the energy remaining in the large scales. The observed linewidths in molecular clouds are always wider than the contribution given by the thermal motions of the molecules, thus another kind of contribution, a *non thermal* motion, is needed. For typical values of MCs $n \sim 100 \text{ cm}^{-3}$, $T \sim 10 \text{ K}$, the viscous dissipation scale is $\sim 0.1 \text{ AU}$ and the Reynolds number is $\sim 10^9$. This high value of the Reynolds number implies that the motion is turbulent. The *Larson's law* is another indication for the presence of turbulent motion in the ISM (see Chapter 1.2.1). Turbulence in the ISM is highly

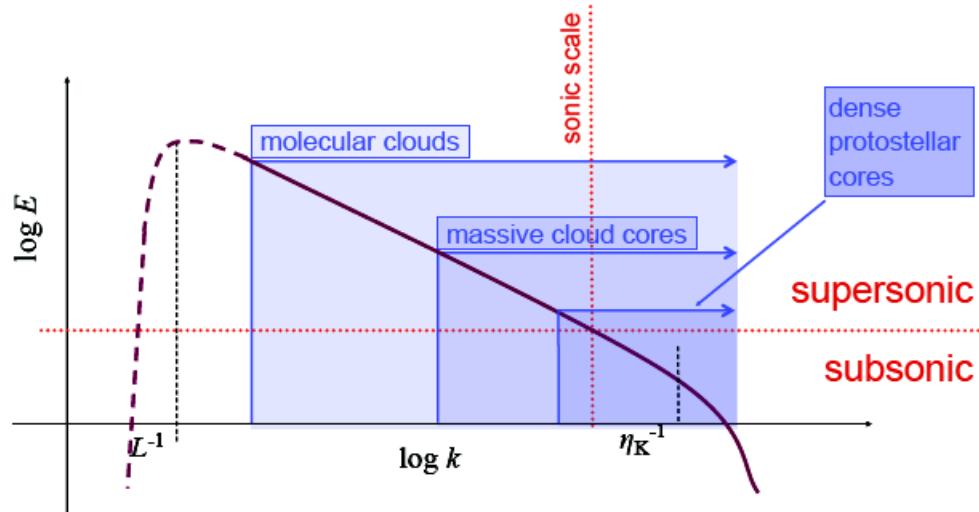


Figure 1.8: Cartoon picture of the turbulent energy spectrum. This cartoon shows the relation between the kinetic energy carried by modes of different wave numbers k and the size of different cloud structures. Turbulence is driven on large scales comparable to the size L of the cloud (not known) and is dissipated on very small scales (not known). From Glover et al. (2015).

compressible, magnetised and multi-phase. At large scales (\sim tens of parsecs) molecular

clouds show motions dominated by supersonic turbulence, with Mach numbers $\mathcal{M} \sim 5 - 20$ (Ballesteros-Paredes et al. 2007), turbulent velocities $\sim \text{few km s}^{-1}$ (the sound speed in the gas is $\sim 0.2 \text{ km s}^{-1}$). These motions are comparable to the typical Alfvén velocities in molecular clouds (Padoan & Nordlund 1999),

$$v_A = \sqrt{\frac{B^2}{4\pi\rho}}, \quad (1.4)$$

where B is the magnetic field strength in the cloud. At small scales dense cores in general have a velocity dispersion where non-thermal, turbulent motions are smaller than the thermal ones (Myers & Benson 1983) and also independent from scales. Goodman et al. (1998) and Caselli et al. (2002) coined the term *coherent core* to describe the fact that non-thermal motions are subsonic and uniform. The cartoon in Fig. 1.8 shows a comparison between the turbulent spectrum and the size of molecular clouds and cores. Goodman et al. (1998) found that the lower density gas around cores, traced using OH and C¹⁸O, has supersonic velocity dispersions that decreases with size as expected in a turbulent flow, while the denser gas of the cores, studied using the NH₃ line emission, shows a thermal, constant width. This implies that a transition to coherence has to occur at some point. Pineda et al. (2010) showed, using a NH₃ map of B5 in Perseus, that the sonic region is surrounded by a region of supersonic turbulence (see Fig. 1.9). The transition between the two regions is sharp and it occurs in less than 0.04 pc. This transition has been observed also in other cores.

In absence of external energy input, supersonic turbulence should decay in a driving scale's sonic time (also called crossing time) $L/\sigma \sim \text{few Myr}$ (Goldreich & Kwan 1974), as demonstrated by simulation conducted for ~ 15 years, both in the hydrodynamical and MHD regime (except the case of imbalanced MHD turbulence, unlikely to occur in MCs, as reported in Ballesteros-Paredes et al. (2007)). Turbulent linewidth are observed in MCs. Since turbulent energy is dissipated, energy has to be re-injected in the gas if MCs have lifetimes much longer than their free-fall times, as found by Blitz & Shu (1980), who estimated a lifetime of $\sim 10 \text{ Myr}$. Several mechanism have been proposed in the literature. If their lifetime is shorter or comparable with the free-fall time (Elmegreen 2000) turbulence doesn't have the time to decay and it must be produced within the cloud itself. Strong density perturbations can be created by supersonic flows in a highly compressible medium.

The strong density inhomogeneities observed in the ISM can be generated also by thermal phase transition or gravitational collapse. A first attempt to analytically derive the density spectrum and a resulting gravitational collapse criterion has been made by

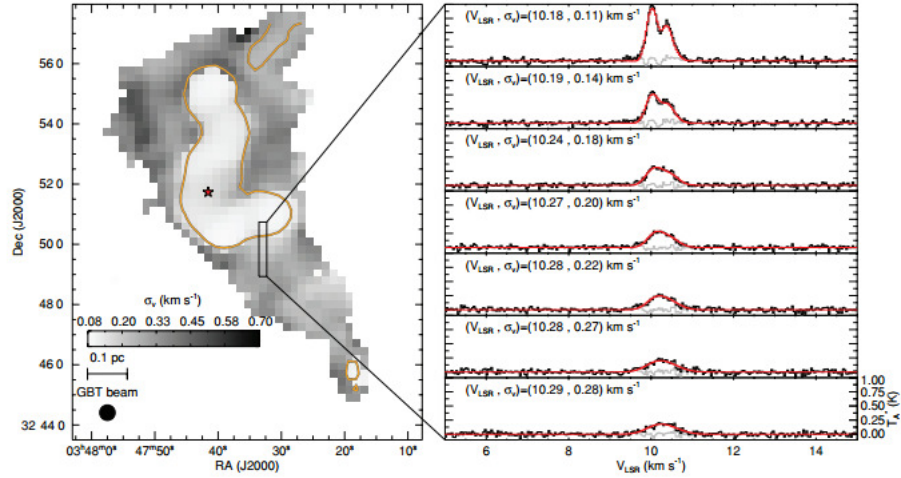


Figure 1.9: Velocity dispersion map derived from fitting all hyperfine components of $\text{NH}_3(1,1)$ along a vertical cut marked by the vertical box in the left panel. The protostar position is shown by the star, and the line shows the contour $T_{peak} = 0.5$ K. The corresponding spectra is presented in the right panel. The centroid velocity and velocity dispersion obtained from the fit are displayed for each position. Top spectra in the right panel display two main hyperfine components clearly separated thanks to their low-velocity dispersion (the coherent core), while when moving to positions outside the core the lines get weaker and broader (evident by the disappearance of the gap between hyperfine components). From Pineda et al. (2010).

Chandrasekhar (1951). In supersonic turbulence energy can be dissipated also via shock waves. They can also transfer energy between different scales, removing the local nature of the incompressible turbulent cascade.

1.5 Magnetic field in molecular clouds

The presence of magnetic fields in the Universe is not well understood. The current paradigm is that magnetic fields in Galactic molecular clouds are the frozen-in fields from the ISM of the Galaxy, which are generated by galactic-scale dynamo amplification of seed fields (Crutcher 2012). The magnetic field of a cloud is probably its most difficult property to measure. The line-of-sight strength of the field can only be directly determined observing the Zeeman splitting of line transitions, like, e.g., the 21 cm line or the OH line, and its plane of the sky direction can be estimated via polarization measurements of background stars, dust emission, or spectral lines. The splitting of the Zeeman component

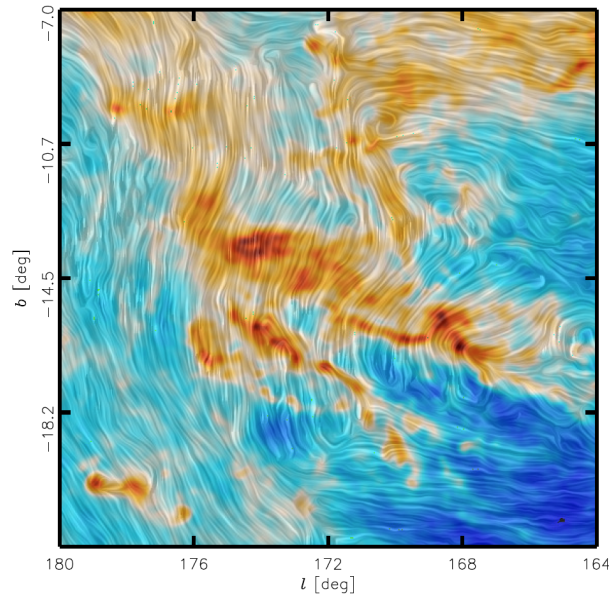


Figure 1.10: Magnetic field (contour) and column density (colour) measured by Planck towards the Taurus molecular cloud. The colours represent column density. The "drapery" pattern indicates the orientation of magnetic field lines, orthogonal to the orientation of the submillimetre polarization (Planck Collaboration 2016).

is proportional to the square of the wavelength and to the strength of the magnetic field. Unfortunately, the magnetic field strength is generally small, implying that the splitting of lines is narrow and often masked by thermal broadening despite the low temperature of molecular clouds and the presence of several transitions in the radio band. Luckily, the line-of-sight component of the magnetic field can be measured using the differential line profile between the two different polarisation of the emitted lines.

Although the magnetic field only acts directly on charged particles (electrons, ions, and charged dust grains), its presence can be felt by the neutral material through collisions. Under most dark cloud conditions, this ion-neutral coupling is highly efficient and, except for the densest regions, the field is expected to be frozen into the gas (Stahler & Palla 2005).

Several atomic and molecular species are tracers of the magnetic field in different regions of the ISM. For the lower density regions, $n \sim 10^2 - 10^3 \text{ cm}^{-3}$, HI is used, while for molecular clouds, $n \sim 10^3 - 10^4 \text{ cm}^{-3}$, the tracer is generally OH. For star forming cores the best tracer is CN. A Bayesian analysis of molecular Zeeman results (Crutcher et al. 2010) suggests that, for any value of the density, the strength of the magnetic field can be

$\sim 5 - 10 \mu\text{G}$. For a comparison, the average strength of Galactic magnetic field is $\sim 5 \mu\text{G}$. In most molecular clouds turbulent and magnetic energies are comparable; in some cases, magnetic energy dominates turbulent energy (Crutcher 2012). The maximum strength of the interstellar magnetic field seems to remain approximately constant at $\sim 10 \mu\text{G}$ up to densities $\sim 300 \text{ cm}^{-3}$. For larger values of the density, the magnetic field strength increases with expected increasing density with a power-law exponent $\kappa \sim 2/3$, expected if gravity dominates the magnetic pressure (Mestel 1966).

Elongated dust grains tend to align their short axis along the magnetic field lines. Their emission is then linearly polarised. When thermal emission from dust grains is observed, the position angle of maximum emission is perpendicular to the magnetic field direction projected on the plane of the sky. In the recent literature, observation made by the Planck Satellite measuring polarisation in extinction from background stars and emission from dust revealed the orientation of the magnetic field averaged along the line of sight and projected on the plane of the sky. These studies (Planck Collaboration 2016) found that regions of higher densities, i.e filaments, have their axis predominantly perpendicular to the magnetic field while regions with lower densities have a magnetic field that appears to be parallel (see i.e Fig. 1.10).

1.6 Virial analysis

The effect of self-gravity on a cloud can be evaluated using a virial theorem analysis. The virial theorem states that

$$\frac{1}{2} \ddot{I} = 2\mathcal{K} + \mathcal{B} + \mathcal{W}, \quad (1.5)$$

where I is the moment of inertia of the cloud, \mathcal{K} is the total kinetic energy of the cloud (thermal plus turbulent), \mathcal{B} is the magnetic energy and \mathcal{W} is the gravity term. The ratios of the various terms considered in the balance are useful to estimate which forces are important during its evolution. Two important ratios are the virial parameter, that consider the value of the internal pressure and bulk motion compared to gravity, and the dimensionless mass to flux ratio, which measures the importance of magnetic field relative to gravity. These ratios are often expressed in terms of masses.

The virial parameter $\alpha_G = M_{\text{virial}}/M_{MC}$ is defined as the ratio between the virial mass of the cloud, $M_{\text{virial}} = 5\sigma^2 R/G$, where σ is the observed velocity dispersion, and the luminous mass of the cloud M_{MC} . For a cloud with uniform density and no surface pressure and no magnetic field $\alpha_g = 1$ correspond to virial equilibrium and $\alpha_G = 2$ to a

cloud that is marginally bound. Solomon et al. (1987) found a correlation between M_{virial} and the CO luminosity, with a coefficient that implies $\alpha_G \sim 1$.

The importance of magnetic forces for the cloud structure is determined by the ratio $\alpha_\Phi = M_{MC}/M_\Phi$, where the critical magnetic mass M_Φ is the mass for which the magnetic energy equals the gravitational energy, $M_\Phi = \Phi/(4\pi^2G)^{1/2}$ and Φ is the value of the magnetic flux threading the cloud (Mouschovias & Spitzer 1976). The magnetic field alone cannot prevent gravitational collapse if $M_{MC} > M_\Phi$ and the cloud is magnetically supercritical, while gravitational collapse is prevented if the cloud is magnetically subcritical, $M_{MC} < M_\Phi$ (McKee & Ostriker 2007). Lizano & Shu (1989) showed that initially subcritical clouds can become supercritical through ambipolar diffusion mechanism. Crutcher (2012) reported a value for $\alpha_\Phi \sim 2 - 3$, thus observed clouds are almost supercritical.

1.7 Theories of star formation

The equilibrium state of molecular clouds and the way they collapse under gravitational forces to form stars is a controversial issue. The typical time scale governing the gravitational collapse of a cloud is the free-fall time (or Jeans time), $t_{\text{ff}} \sim \sqrt{G\rho}$. Associate quantities are the *Jeans length* $\lambda_J \sim \sqrt{c_s^2/G\rho}$ and the *Jeans mass* $M_J \sim c_s^3/\rho^{1/2}G^{3/2}$. Perturbations with a wavelength $\lambda > \lambda_J$ or with masses that exceeds M_J become unstable to gravitational collapse.

The uncertainties on the strength and direction of the magnetic field and the importance of the turbulent motions, together with the wide range of lifetimes of MCs (1 – 10 Myr) have resulted in two differing views of the global state of clouds. In the *quasi-static* view clouds are close to equilibrium, gravitationally bound, virialised and have long lifetimes (several free-fall times: at least 10 Myr). The equilibrium against self-gravity is provided by the magnetic field and molecular clouds evolve under gravity, quasi-statically. If the magnetic field is strong enough to make the cloud subcritical, the magnetic field remains frozen into the matter and gravitational collapse cannot occur. This process is rather inefficient, in agreement with the low rate of star formation. Ambipolar diffusion removes magnetic support against gravity in cores and triggers collapse when they have accumulated enough mass (Shu et al. 1987). Evidence that some molecular clouds are magnetically supercritical goes against this theory.

The *dynamic* point of view emphasises the role of supersonic turbulence and lack of equilibrium. Numerical simulations have shown that turbulence decays in about a dynamical time, so, without continuous energy injection, it cannot provide support. In this picture clouds form from convergent flows and evolve without reaching an equilibrium in

lifetimes of the order of the free-fall time (1 Myr). The formation of structures is therefore driven by the turbulent enhancement of density perturbations. Compressible turbulence forms self-gravitating clumps that collapse as soon as the turbulent cascade produces insufficient support. Once the stars are formed, the molecular cloud is disrupted by feedback processes. The mechanism for this feedback are photoionisation and supernovae. Some simulations suggest that these mechanism can enforce low star formation rates (Vázquez-Semadeni et al. 2010). It remains unclear what mechanism might disrupt GMCs.

Turbulence can also prevent large-scale collapse. Supersonic motions can behave like pressure for structures that have sizes larger than the largest scale of the turbulent motion. It can also induce local compression at scales smaller than that. Mac Low & Klessen (2004) showed using an analytical argument that, regardless of the driving turbulence (internal or external), its effect is to increase the effective Jeans mass as $M_{J,turb} \propto v_{turb}^2$. Turbulence can be parametrised as an additional "pressure" component (Vázquez-Semadeni et al. 1998), a concept that we will address in Chapter 7. However, this is true only if the turbulence is sustained. If it is allowed to decay, the star formation is more efficient because turbulence creates initially dense region and then it decays. Magnetic fields can decrease the star formation efficiency.

2

Physical description of the interstellar medium

Almost all the interstellar medium is in gaseous form, and can be treated as a *fluid* (Shu 1992). A fluid is an idealized continuous medium with certain macroscopic properties such as density, pressure and velocity. The structure of matter at the atomic or molecular level is important only in fixing relations between macroscopic fluid properties such as density and pressure, and in specifying others such as viscosity. The observational evidence of magnetic fields and the ionisation degree already introduced in Chapter 1 allows us to consider the ISM a multicomponent, partially ionised plasma.

A *plasma* is any state of the matter which has enough free, charged particles to have its dynamical behaviour dominated by electromagnetic forces: it is the ensemble of the charged particles and the fields they generate. Note that very low degrees of ionisation are sufficient to make a gas exhibit electromagnetic properties: with a 0.1% ionisation the electrical conductivity of a gas is half of its maximum value and with a 8% ionisation the conductivity is almost equal to the fully ionised value.

Characteristics of a plasma are the *quasi neutrality*, related to the *Debye length* λ_D , the collision frequency ν_c , the plasma frequency ω_p and the *Larmor* frequency ω_L . A definition and description of all these quantities is given in Appendix A.

2.1 MHD approximation

Describing a medium as a fluid or a plasma implies the definition of physical quantities such as:

$$\rho(\mathbf{r}, t) = \text{mass density}, \quad \mathbf{u}(\mathbf{r}, t) = \text{velocity}, \quad P(\mathbf{r}, t) = \text{pressure} \quad (2.1)$$

at a particular place with position \mathbf{r} at time t . In the fluid description of a plasma approximations are necessary to reduce the range of possible parameters. Choosing the plasma *regime* allows to neglect terms that are negligible in the scales considered. A very important regime derived from the collisional one-fluid model is the (classical) magneto-hydrodynamic regime. In order to discuss its validity it is necessary to define a length L and a time τ characteristic for electric and magnetic field dynamics. If U is the plasma fluid velocity's scale value, the MHD regime is defined by the following conditions:

$$U \sim \frac{L}{\tau}; \quad U \ll c, \quad (2.2)$$

where c is the speed of light. The first requirement states that the speed of hydrodynamical and electromagnetic processes have the same order of magnitude, corresponding to a maximum of the mutual interactions. The second one implies that the macroscopic plasma motions are non-relativistic.

The starting point are Maxwell's equations for the electromagnetic field. The first equations are the conservation ones, both of which are divergence conditions for the fields. Conservation of magnetic flux, \mathbf{B} , given by:

$$\nabla \cdot \mathbf{B} = 0, \quad (2.3)$$

is given by the fact that there are no charge-like sources for the magnetic field (or, in other words, there are no magnetic monopoles). The electric field, has a source term, instead. Its strength, \mathbf{E} , follows the conservation law

$$\nabla \cdot \mathbf{E} = 4\pi\rho_e, \quad (2.4)$$

where ρ_e is the charge density. The other two equations are the time-dependent equation for the evolution of the field components, first for the induction field:

$$\nabla \times \mathbf{E} = -\frac{1}{c} \frac{\partial \mathbf{B}}{\partial t}, \quad (2.5)$$

and Maxwell-Ampère's law:

$$\nabla \times \mathbf{B} = \frac{1}{c} \frac{\partial \mathbf{E}}{\partial t} + \frac{4\pi}{c} \mathbf{J}, \quad (2.6)$$

where $\frac{1}{c} \frac{\partial \mathbf{E}}{\partial t}$ is the displacement current and \mathbf{J} is the charge current. The displacement current can be neglected in the MHD regime (it implies also that MHD is a low frequency

regime, due to the fact that the displacement current becomes important only when the electric field varies rapidly with time). Because plasma cannot support any internal fields, the charges cannot separate and the current is determined only by the magnetic field.

Our purpose is to study equilibrium states and the dynamics of self-gravitating objects, so we need to introduce and define also the *gravitational potential* \mathcal{V} , in order to consider the gravitational force in the force balance. The gravitational potential is related to the density through Poisson's equation,

$$\nabla^2 \mathcal{V} = 4\pi G \rho. \quad (2.7)$$

where G is the gravitational constant. The equations of MHD then become:

$$\frac{\partial \rho}{\partial t} + \nabla \cdot (\rho \mathbf{u}) = 0 \quad \text{mass continuity,} \quad (2.8)$$

$$\rho \frac{d\mathbf{u}}{dt} = \frac{1}{4\pi} (\nabla \times \mathbf{B}) \times \mathbf{B} - \nabla P - \rho \nabla \mathcal{V} + \zeta \left[\nabla^2 \mathbf{u} + \frac{\nabla(\nabla \cdot \mathbf{u})}{3} \right], \quad \text{Navier-Stokes equation,} \quad (2.9)$$

$$\nabla \times \mathbf{E} = -\frac{\partial \mathbf{B}}{\partial t} \quad \text{Faraday's law,} \quad (2.10)$$

$$\nabla \times \mathbf{B} = \frac{4\pi}{c} \mathbf{J} \quad \text{Ampère's law,} \quad (2.11)$$

$$\nabla \cdot \mathbf{B} = 0, \quad \text{no magnetic monopoles} \quad (2.12)$$

$$\mathbf{E} + \frac{\mathbf{u}}{c} \times \mathbf{B} = \eta \mathbf{J} \quad \text{resistive Ohm's law,} \quad (2.13)$$

where $\zeta = \nu/\rho$ is the kinetic viscosity and η is the electrical resistivity of the plasma and d/dt the convective derivative. If the plasma is sufficiently collision dominated for the fluid picture to apply, but the resistivity appearing in equation (2.13) is negligible, the right-hand side of eq.(2.13) may be neglected:

$$\mathbf{E} + \frac{\mathbf{u}}{c} \times \mathbf{B} = 0 \quad \text{ideal Ohm's law.} \quad (2.14)$$

This equation means that there is no electric field in the rest frame of the fluid. These equations, with the ideal Ohm's law and $\zeta = 0$ in eq. (2.9), constitute the *ideal* MHD equations, which is usually contracted to MHD. The inclusion of eq. (2.13) and $\zeta \neq 0$ is called *resistive* MHD. Note that an energy equation or an equation of state (EOS) is needed to close the system. In this work we will use two different equations of state, the *isothermal* EOS

$$P = c_s^2 \rho, \quad (2.15)$$

and a *polytropic* EOS. In particular, we will assume that the relation between the pressure and the density has a simple power-law form:

$$P = \hat{K}\rho^{1+1/n} \quad (2.16)$$

where \hat{n} is called the *polytropic index*. It is one of the most generally used forms for the (EOS), especially in thermodynamics¹. In this work we will use a different notation for the polytropic equation, in order to follow the definitions of Li & Shu (1996) and Galli et al. (1999).

$$\frac{dP}{d\rho} = K\rho^{-(1-\gamma_p)}, \quad (2.17)$$

where γ_p is the *polytropic exponent*, $\gamma_p = 1 + 1/n$. In the limit of $\gamma_p \rightarrow 0$ (or $n \rightarrow -1$), the EOS becomes *logatropic*, $P \sim \ln\rho$, a form first used by Lizano & Shu (1989) to mimic the non-thermal support in molecular clouds associated with the observed supersonic line widths. The MHD equations have to be solved given some initial and boundary conditions.

The ideal Ohm's law couples the fluid to the fields. In this case, the Alfvén theorem proves that the magnetic flux is conserved². This means that the field lines are *frozen* into the fluid, thus that the magnetic field topology is an invariant. Using the resistive Ohm's law even a small value of resistivity will allow the field lines to diffuse and its topology will be not conserved.

It can be shown that ideal MHD possesses the following conservation properties³:

- conservation of mass;
- conservation of momentum;
- conservation of energy (both mechanical and electromagnetic);
- conservation of magnetic flux.

A very important parameter is β , the relative importance of plasma kinetic to magnetic

¹The polytropic index is usually indicated as γ and is equal to the ratio of the specific heats. For a perfect gas, one composed of identical particles with only translational degrees of freedom and no additional correlations in the distribution function, this ratio is 5/3. In our study, we denote the polytropic exponent as γ_p to indicate a generic index in the pressure-density relation applicable to a variety of situations relevant for molecular clouds and cores.

²See, e.g., Stahler & Palla (2005) or Chiuderi & Velli (2015) for a demonstration.

³For a complete study see i.e Stahler & Palla (2005) or Chiuderi & Velli (2015).

pressures, defined as

$$\beta = \frac{P}{(B^2/8\pi)} = \frac{2}{3} \frac{E_{th}}{E_{mag}}. \quad (2.18)$$

The thermal energy density is $E_{th} = 3/2P$ and the magnetic energy density is $E_{mag} = B^2/8\pi$. If $\beta \gg 1$ the system is dominated by hydrodynamical effects, while when $\beta \ll 1$ magnetic effects are dominant.

2.1.1 Force-free fields

If the Lorentz force dominates the pressure gradient and the gravitational force in eq. (2.9), the force balance reduces to

$$\frac{1}{c} \mathbf{J} \times \mathbf{B} = 0. \quad (2.19)$$

The electric current flows along magnetic field lines and, since it is given by Ampere's Law (2.11), eq. (2.19) can be written as

$$\nabla \times \mathbf{B} = \kappa \mathbf{B} \quad (2.20)$$

where κ is some function of position and it is required to be constant along each field line. Indeed, taking the divergence of eq. (2.20) the left-hand side vanishes identically and the right-hand side reduces to $\mathbf{B} \cdot \nabla \kappa = 0$, which implies that \mathbf{B} lies on surface of constant κ (as does also \mathbf{j}).

2.2 Ambipolar diffusion and magnetic reconnection

In the quasi-static scenario (See Section 1.7) MCs resist self-gravity through both thermal pressure and magnetic forces. There are two ways by which an initially stable cloud, like a starless dense core, can dissipate magnetic field and evolve to the point of collapse: ambipolar diffusion and magnetic reconnection. However, only the charged species sense the magnetic field. Electrons and ions, gyrating around \mathbf{B} , collide with the neutrals, and the drag resulting on the latter helps to counteract gravity. The drag force per unit volume between the neutral and the charged components is related the product of the density and relative velocity of that species. If the cloud's level of ionization is sufficiently low, these relative speeds become appreciable. The neutrals then gradually drift across magnetic field lines in response to gravity. As a consequence there is a loss

of magnetic flux, the contribution of the cloud's magnetic field to the stability decreases, and then the cloud contracts until it eventually becomes unstable to collapse.

Electrons and ions must be moving at very nearly the same velocity. For a cloud of size L , then $L/|\mathbf{u}_i - \mathbf{u}_e|$ is much longer than the time over which the cloud evolves. For a dense core with $L = 0.1$ pc, $B = 30\mu$ G, $n_{\text{H}_2} = 10^4$ cm $^{-3}$, and $n_e = 5 \times 10^{-8}n_{\text{H}_2}$, this time is of order 10^{10} yr. Electrons and ions can be considered as a single plasma drifting relative to the neutrals. the drift velocity $\mathbf{v}_{\text{drift}} = \mathbf{u}_i - \mathbf{u}_e$ resulting in a modification of the Ohm's equation,

$$\frac{\partial \mathbf{B}}{\partial t} = \nabla \times (\mathbf{u}_i \times \mathbf{B}) = \nabla \times (\mathbf{u} \times \mathbf{B}) + \nabla \times (\mathbf{v}_{\text{drift}} \times \mathbf{B}). \quad (2.21)$$

This equation shows that flux freezing still holds if the conductivity is large enough, but implies that the electrons and ions are tied to \mathbf{B} , while the neutral atoms and molecules in the cloud slip past.

The drift velocity introduces also a relevant time scale, $\tau_{ad} \sim L/|\mathbf{v}_{\text{drift}}|$,

$$\tau_{ad} \sim 3 \times 10^6 \text{ yr} \left(\frac{n_{\text{H}_2}}{10^4 \text{ cm}^{-3}} \right)^{3/2} \left(\frac{B}{30 \mu\text{G}} \right)^{-2} \left(\frac{L}{0.1 \text{ pc}} \right)^2. \quad (2.22)$$

Comparing this result to the estimate for cloud lifetimes ($10^6 - 10^7$ yr), we see that $\mathbf{v}_{\text{drift}}$ is indeed significant. In the quasi-static view ambipolar diffusion is the main process setting the rate at which dense cores evolve prior to their collapse. Fig. 2.1 shows the comparison between the relevant dynamical timescales, that is the free-fall and ambipolar diffusion times, with the chemical timescales, depending on cosmic rays and freeze-out of molecules. The free-fall timescale is given by Eq. (1), the ambipolar diffusion timescale assumes a degree of ionisation $= 2 \times 10^{-8}(n_{\text{H}_2}/10^5 \text{ cm}^{-3})^{-1/2}$, the cosmic-ray timescale has a constant dependence on the density while freeze-out has linear dependence on the density. The ambipolar diffusion time is the longest time-scale while the free-fall time is the shortest. The chemical time-scales are important to estimate the degree of ionisation, which is related to the flux of cosmic rays, and the density of molecular clouds.

The assumption that the ion-electron plasma acts like a perfectly conducting fluid can break down. At sufficiently high densities, the field being dragged undergoes *magnetic reconnection*. This process effectively destroys magnetic flux before it can be transported onto the star and its disk. Reconnection usually occurs whenever field lines of opposite direction are pressed together, but it is sufficient that the component of \mathbf{B} along some given direction changes sign when moving across the associated current sheet. Magnetic energy is dissipated as heat within a restricted region. Here, antiparallel lines annihilate one

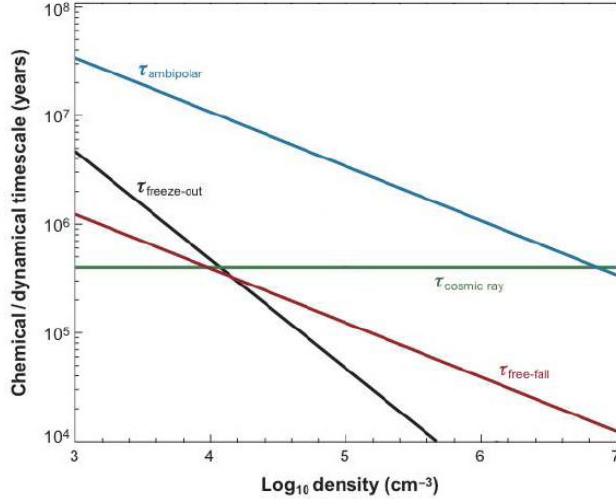


Figure 2.1: Plot of various chemical and dynamical timescales shown as a function of the H_2 volume density. In this plot, the cosmic-ray timescale is set by the time for any change from an equilibrium state to be reset by cosmic-ray powered chemistry. Figure taken from Bergin & Tafalla (2007).

another, changing the field topology. From a mathematical perspective, the last, Ohmic term in the MHD equation (2.13) increases until it becomes dominant, regardless of the specific conductivity value. This process occurs on time-scales shorter than the ambipolar diffusion, thus the associated time-scale for molecular clouds evolution is comparable with the one given by the dynamic theory of MCs formation.

2.3 Basics of Turbulence

In the theory of star formation turbulence is an important ingredient, as already described in the previous Chapter. Thanks to theoretical efforts and numerical simulations significant progress has been made in understanding the effects of turbulence in MC, cores and SF. The classical picture of incompressible turbulence (Kolmogorov 1941) is a good description for turbulent flows with velocity fluctuations that are smaller than the speed of sound. For subsonic turbulent flows density fluctuations are negligible.

The key-assumption made by Richardson (1920) is that the kinetic energy is injected into the system on some well-defined, large scale L , and that it cascades through a sequence of eddies of decreasing size until the size of the eddies becomes comparable to

the mean free path. The kinetic energy associated with eddy motion is converted into heat (random thermal motion) and dissipated away (see e.g the review by Glover et al. 2015).

In the hydrodynamical case, one need to consider the continuity and Navier-Stokes equations,

$$\frac{\partial \rho}{\partial t} + \mathbf{u} \cdot \nabla \rho = -\rho \nabla \cdot \mathbf{u}, \quad (2.23)$$

$$\frac{\partial \mathbf{u}}{\partial t} + \mathbf{u} \cdot \nabla \mathbf{u} = -\frac{\nabla P}{\rho} - \nabla \mathcal{V} + \zeta \left[\nabla^2 \mathbf{u} + \frac{\nabla(\nabla \cdot \mathbf{u})}{3} \right], \quad (2.24)$$

coupled with Poisson's eq. (2.7) and the EOS (i.e. 2.15 or 2.17); $\zeta = \nu/\rho$ is the kinetic viscosity over density in the units $\text{cm}^2 \text{s}^{-1}$. In the Navier Stokes equation, the second term on the left is called the *advective* term, and represents the transport of momentum by the component of the velocity and it is responsible for non linear interactions. The pressure gradient term counteracts pressure and density gradients across the flow while the *viscous*, diffusive term, tends to smear out velocity gradients in order to produce a uniform flow (see e.g the review by Vazquez-Semadeni 2012).

At any spatial scale ℓ the spatial derivative ∇ can be approximated as $\sim \ell^{-1}$, thus advection and viscous terms can be compared. If u_ℓ is the typical velocity fluctuation on scale ℓ

$$(\mathbf{u} \cdot \nabla) \mathbf{u} \approx \frac{u_\ell^2}{\ell} \quad \text{and} \quad \zeta \nabla^2 \mathbf{u} \approx \zeta \frac{u_\ell}{\ell^2}. \quad (2.25)$$

This ratio defines the dimensionless *Reynolds number* on that scale,

$$\mathcal{R} = \frac{u_\ell \ell}{\zeta}. \quad (2.26)$$

A flow becomes unstable and changes from being laminar to turbulent if the Reynolds number exceeds a critical value $\mathcal{R}_{e,cr} \approx \text{few } 10^3$. In the ISM, the Reynolds number can easily exceed this values of several order of magnitude, as reported into the Introduction, indicating that the ISM is highly turbulent.

Turbulence is an unsolved problem. In Kolmogorov's picture turbulence forms eddies on a wide range of different length scales after some driving mechanism injects energy on some larger injection scale L . The energy contained in large eddies is transported down to smaller and smaller ones in an inviscid way until it reaches scales that are small enough so that molecular diffusion becomes important. Kinetic energy turns into random thermal motion and may be radiated away. An estimate of the energy cascade rate through eddies of size ℓ is

$$\epsilon \approx \frac{u_\ell^2}{t_\ell} \approx \frac{u_\ell^3}{\ell} \quad (2.27)$$

where ϵ_ℓ is the flux of energy flowing from the scale ℓ to smaller scale in an eddy turnover time. When ϵ is constant, energy is transferred to smaller scales without being dissipated. This defines the *inertial range* of the turbulent cascade. It ends when the local Reynolds number approaches unity at a dissipation scale ℓ_d . The inertial range covers the scale between $L > \ell > \ell_d$. An estimate of the size of the inertial range can be obtained using the requirement that $\mathcal{R} \sim 1$ on the dissipation scale, thus $L/\ell_d \sim \mathcal{R}^{3/4}$. A constant cascade rate implies that the typical eddy velocity changes with eddy scale as $u_\ell = \epsilon \ell^{1/3}$, which leads to the Komogorov spectrum for isotropic incompressible turbulence E_{1D} (Kolmogorov 1941),

$$E_{1D} \sim \epsilon^{2/3} k^{-5/3}. \quad (2.28)$$

Observations of nearby molecular clouds are in agreement with this picture of the turbulent cascade. The energy seems to be carried by large-scale modes, indicating that the turbulent velocity field in these clouds is driven by external sources (see e.g the review by Glover et al. (2015)).

However, observed turbulent velocities in molecular clouds are in general not small compared to c_s (as pointed out in the Introduction, molecular clouds have sonic Mach numbers of $\mathcal{M}_s \sim 5$, while cores are transonic or subsonic, with $0.5 < M_s < 1$). Therefore Kolmogorov theory cannot be strictly applied. The gas is compressible and energy at a given scale can be also dissipated via shocks, rather than be conserved through intermediate scales until it reaches the dissipation scale.

2.3.1 Compressible turbulence and Burgers equation

In the limit of highly compressible turbulence the flow can be described as a network of interacting shock fronts. If pressure gradients can be neglected ($u > c_s$) we obtain the *Burgers turbulence* (Frisch & Bec 2001). Burgers (1948) simplified the Navier-Stokes eq. (2.24) by dropping the pressure term and studied the non-linear partial equation in one spatial dimension,

$$\frac{\partial u}{\partial t} + u \frac{\partial u}{\partial x} = \zeta \frac{\partial^2 u}{\partial x^2}. \quad (2.29)$$

This simplification makes possible to study the transition between the linear and the non linear phase. However, it has been shown that the homogeneous Burger's equation does not exhibit chaotic features like sensitivity to initial conditions (Hopf 1950), which are characteristic of turbulence.

2.3.2 Magnetohydrodynamical turbulence

Molecular clouds are magnetised, being embedded in the Galactic magnetic field. Turbulence in a magnetised system is different from the unmagnetised case because there are additional wave families and non-linear couplings involved. The energy spectrum of MHD turbulence is not well constrained. The presence of a strong magnetic field \mathbf{B} makes the system anisotropic.

The classical theory has been made by Iroshnikov (1963) and Kraichnan & Nagarajan (1967). In this theory eddies can travel along field lines and then the interaction time is reduced, weakening the cascade. The time between two interactions is $t_A \sim (kv_A)^{-1}$, while the change in velocity is estimated from the non-linear advection term $\delta u_\ell / u_\ell \propto u_\ell / v_A$. Assuming a constant energy flux at all scale it can be found that $u_\ell \propto \ell^{1/4}$ and that the energy spectrum $E(k) \propto k^{-3/2}$ (see e.g the review of Hennebelle & Falgarone 2012). This is the spectra for MHD turbulence under the assumption that the eddies are isotropic, i.e. have the same spatial extension in the parallel and perpendicular directions. However, numerical results and observational data indicate that in MHD turbulence the energy transfer occurs predominantly in the direction perpendicular to the field (see e.g Biskamp 2003).

Goldreich & Sridhar (1995) introduced for incompressible MHD turbulence the idea of a critically balanced anisotropic cascade (i.e $k_{\parallel} v_A \sim u k_{\perp}$). They suggested that as the energy cascades to smaller scales, turbulent eddies progressively become elongated along field lines. The energy transfer time is different from the Iroshnikov-Kraichnan estimate, and equal to the Kolmogorov one. The field-perpendicular energy spectrum is predicted to be $E(k_{\perp}) \propto k_{\perp}^{-5/3}$.

The above phenomenologies help to understand the main feature of the turbulent dynamics. However, the research field is still active with new emerging phenomenology that need to be verified. Unfortunately, for the case compressible gas and moderate or strong magnetic fields, that describe molecular clouds state, there is no conceptual theory as above to characterize the energy transfer between scales.

2.4 Outline

In the next Chapters we will describe our original work. This thesis focus on the study of the stability and contraction of molecular clouds. In particular, Chapter 3 and Chapter 4 focus on the stability of molecular clouds. In both Chapters we suppose that the evolution of filamentary molecular clouds can be described as a series of hydrostatic (Chapter 3 Toci & Galli 2015a) or magnetostatic (Chapter 4 Toci & Galli 2015b) models, and we studied their radial density profiles and stability properties. Beside the quasi-static evolution, molecular clouds start to contract. We are interested in understanding the phase of dynamical collapse and, in particular, the evolution of the physical properties of a fluid element during this process. In Chapter 5 we describe the theoretical and numerical framework needed to describe the contraction of a cloud and the implementations we made. In Chapter 6 we applied our scheme to study the growth of density perturbations and the formation of sub-structures and fragment in pre-stellar cores (Toci et al. 2017). In Chapter 7 we show the analysis performed for the case of a contraction of a fluid element along a mean magnetic field, in order to study the mass accretion of filaments, and we compute numerically the time-evolution of the relevant physical quantities (density contrast, velocity fluctuations..). Conclusions and future improvements are described in Chapter 8.

3

Equilibrium of hydrostatic filamentary structures

The filamentary structure of molecular clouds has recently received considerable attention, as shown in the Introduction. From a theoretical point of view origin, the physical state (whether they are or are not into some kind of equilibrium) and evolution of interstellar filaments still have to be fully understood. However, observationally, star forming cores are found in filaments that are predicted to be gravitationally unstable on the basis of equilibrium models, thus some kind of equilibrium theory could be a reliable description for these clouds. In this Chapter we will analyse the radial density profiles of filamentary clouds and their stability with respect to collapse. We will also use the observed properties (from [Arzoumanian et al. 2011](#)) to draw some conclusions on the relative importance of various mechanisms of radial support (or confinement) of these clouds.

Theoretical studies focused on different kinds of possible physical states for filaments, as reported in [Andre et al. \(2000\)](#), i.e. a) structure in a HD or MHD somehow stable equilibrium, b) equilibria with a considerable amount of radial accretion, c) collapsing and fragmenting systems that are the product of unstable equilibria, and d) highly dynamical systems that are not reproducible with equilibrium models. A parametrisation of the radial density profile that reproduces the basic observed features is a softened power-law profile

$$\rho(\varpi) = \frac{\rho_c}{[1 + (\varpi/\varpi_{\text{flat}})^2]^{\alpha/2}}, \quad (3.1)$$

where ρ_c is the central density, ϖ is the radial distance from the cylinder axis and α is a parameter. For $\alpha = 4$, [Stodólkiewicz \(1963\)](#) and [Ostriker \(1964b\)](#) found that eq. (3.1) is an exact solution of the equation of hydrostatic equilibrium for a self-gravitating isothermal cylinder, hereafter referred to as the isothermal density profile. In this case $\varpi_{\text{flat}} = (2c_s^2/\pi G\rho_c)$, where c_s is the isothermal sound speed.

Arzoumanian et al. (2011), in her study with the *Herschel* satellite mapped different clouds, IC5146, Aquila and Polaris, found that the power-law slope α is significantly different from $\alpha = 4$: on average, $\alpha = 1.6 \pm 0.3$. This implies that the gas in these filaments obeys a non-isothermal equation of state, and then a case relaxing the hypothesis of thermal support should be explored. We will show in Sect. 3.2.1 that filamentary clouds' radial density profiles are well reproduced by assuming an equations of state "softer" than isothermal. This means that they are unlikely to be thermally supported, in agreement with recent observations. In this case, as shown by Viala & Horedt (1974b) the behaviour of cylindrical clouds with respect to gravitational instability becomes essentially analogous to that of spherical clouds (see Sect. 3.3).

In order to obtain some properties of basic hydrostatic equilibrium theory that are relevant in real molecular clouds we multiply Poisson's eq. (2.7) written for a cylinder of infinite length by ϖ , then we integrate from the center to the outer radius $\hat{\varpi}$, obtaining the self-gravitational force per unit mass $F_{g,cyl}$,

$$F_{g,cyl} = \left. \frac{d\mathcal{V}}{d\varpi} \right|_{\varpi=\hat{\varpi}} = 2 \frac{G\mu_{\text{line}}}{\hat{\varpi}} \propto \frac{1}{\hat{\varpi}}, \quad (3.2)$$

where μ_{line} is the mass per unit length. The pressure gradient force per unit mass, F_p , using a polytropic EOS $p \propto \rho^{\gamma_p}$ (See also eq. (2.16)), is

$$F_p = \frac{1}{\rho} \frac{\partial P}{\partial \varpi} \propto \hat{\varpi}^{1-2\gamma_p}, \quad (3.3)$$

showing that the ratio between the two forces depends on γ_p , as $F_p/f_{g,cyl} \propto \hat{\varpi}^{2-2\gamma_p}$. This implies that, if $\gamma_p > 1$, pressure forces will give support against self gravity at some radius $\hat{\varpi}$, while if $\gamma_p < 1$ filaments will undergo radial collapse indefinitely once started. The critical case $\gamma_p = 1$ represents hydrostatic equilibrium if the two forces are equal. Then we can find for an isothermal cylinder of infinite radius a finite mass per unit length,

$$\mu_{\text{iso}} = \int 2\pi\rho_{\text{iso}}\varpi d\varpi = \frac{2c_s^2}{G} = 16.5 \left(\frac{T}{10 \text{ K}} \right) M_{\odot} \text{ pc}^{-1}. \quad (3.4)$$

In this case the critical mass per unit length depends only on the gas temperature. With similar considerations, for a spherical cloud $\gamma_{p,crit} = 4/3$ while for a sheet $\gamma_{p,crit} = 0$. Sheet-like clouds always have an equilibrium configuration because the internal pressure gradient can always be sufficiently strong to stop the gravitational collapse independently from the initial configuration, as shown by Miyama et al. (1987).

The radial collapse of isothermal cylinders cannot be halted for $\mu_{\text{line}} > \mu_{\text{iso}}$, thus equi-

librium states are never possible, while if $\mu_{\text{line}} < \mu_{\text{iso}}$ gravity will never dominate and collapse will halt at some finite radius. This has been pointed out by McCrea (1957). In his work he found a fundamental difference between the behaviour of *isothermal* spherical and cylindrical interstellar clouds with respect to gravitational collapse: while for a spherical cloud of given mass and temperature there is a maximum value of the external pressure for which an equilibrium state is possible (the Bonnor-Ebert criterion), a cylindrical cloud can be in equilibrium for any value of the external pressure, provided its mass per unit length is smaller than a maximum value. Thus filamentary (or sheet-like) clouds must first break up into fragments of roughly the same size in all directions before gravitational collapse (and therefore star formation) can take place.

In particular, we will perform an analysis of the stability of filamentary clouds in analogy with the theoretical studies of spherical clouds made by McKee & Holliman (1999), underlying the need for non-isentropic models in order to reproduce the observed large density contrasts. The stability properties of polytropic cylinders can be characterised, as in the case of spherical polytropes, with the polytropic exponent γ_p , that determines the spatial properties of the filament, and with the adiabatic exponent γ , that characterises the temporal response of the cloud to adiabatic perturbations.

3.1 Radial density profiles of filamentary clouds

3.1.1 Basic equations

Neglecting magnetic fields, the structure and evolution of a self-gravitating filament is governed by the force equation

$$(\mathbf{u} \cdot \nabla)\mathbf{u} = -\nabla\mathcal{V} - \frac{1}{\rho}\nabla p, \quad (3.5)$$

and Poisson's equation

$$\nabla^2\mathcal{V} = 4\pi G\rho. \quad (3.6)$$

The left-hand side term in eq. (3.5) represents the contribution of dynamical motions on the momentum balance. These are the laminar and turbulent flows related to the formation of the filament and/or produced by the gravitational field of the filament itself. In a cylindrical coordinate system with the z axis along the filament's axis and the ϖ axis in the radial direction, assuming azimuthal symmetry ($\partial/\partial\varphi = 0$), and neglecting rotation,

the component of the left-hand side of eq. (3.5), that is only radial, reads

$$(\mathbf{u} \cdot \nabla)\mathbf{u} = \left(u_{\varpi} \frac{\partial u_{\varpi}}{\partial \varpi} + u_z \frac{\partial u_{\varpi}}{\partial z} \right) \hat{\mathbf{e}}_{\varpi}. \quad (3.7)$$

The first term in eq. (3.7) represents an external ram-pressure compressing the filament. For a filament that is building its mass by accretion from the surrounding medium, then u_{ϖ} is negative and decreases inward ($u_{\varpi} = 0$ by symmetry on the filament's axis). The internal pressure dominates over the accretion ram pressure if u_{ϖ} becomes subsonic inside the filament, where \mathbf{u} is expected to be mostly parallel to the filament's axis (as e.g. the simulations of Gómez & Vázquez-Semadeni 2014). Accretion ram-pressure can be neglected in the central parts of a filament, even if it may be important in the envelope¹. For those reasons, a picture of the structure of filamentary clouds in terms of hydrostatic equilibrium models does not necessarily require that the velocity field is zero everywhere. During the growth of the varicose (or sausage) gravitational instability, when significant radial and longitudinal gas flows can occur (see e.g. Gehman et al. 1996), the velocity term in eq. (3.5) cannot be neglected. These motions may trigger the formation of dense prestellar cores as observed e.g. in the SDC13 infrared dark cloud by Peretto et al. (2014).

3.1.2 Isothermal parametrisations

Isothermal cylinders have been used to successfully model observations of limited spatial extent of intensity radial profiles. As an example, the Stodólkiewicz-Ostriker density profile is compatible with observations of molecular line emission in L1517 (Hacar & Tafalla 2011), and from the 850 μm emission in the filamentary dark cloud G11.1 1-0.12 (Johnstone et al. 2003) up to ~ 0.2 pc. Fischera & Martin (2012) have modelled the surface brightness profiles of 4 filaments observed by *Herschel* in the IC5146 region using truncated isothermal cylinders. Their analysis has been done in the range to $\sim 1'$ radial distance from the emission peak on both sides of the filament (corresponding to 0.13 pc at the distance of 460 pc). In this range, the column density profiles obtained by eq. (3.1) with $\alpha = 2$ or $\alpha = 4$, or by a gaussian profile, are all indistinguishable (see e.g. Fig. 4 of Arzoumanian et al. 2011). The sub-millimetre emission of interstellar filaments has been mapped up to the radial distances from the filament's axis where the structures merge with

¹However, for a Larson-Penson type of accretion, u_{ϖ} approaches a constant value at large radii and the accretion ram-pressure drops to zero. The second term in eq. (3.7) is negligible if the accretion velocity u_{ϖ} does not change significantly along the filament, and vanishes in cylindrical symmetry ($\partial/\partial z = 0$).

the ambient medium thanks to the large dynamical range allowed by the *Herschel* Space Observatory (~ 0.4 pc for B211/213, [Palmeirim et al. 2013](#); ~ 1 pc for IC5112, [Arzoumanian et al. 2011](#)). At large radii the observations are generally not well reproduced by isothermal cylinders. The Stódołkiewicz-Ostriker profile is no longer a good model because deviations from the observed density profiles become evident. In fact, as already mentioned before, a first reason for this deviation is that the density profiles at large radii are characterised by power-law exponents α close to ~ 2 , rather than 4. A second one is that the mass per unit length can be in some cases larger than the maximum value allowed for an isothermal cylinder (eq. 3.4). We will examine these aspects in the following sections.

3.1.3 Polytropic models

As already introduced in Chap. 2, a more general class of hydrostatic models for filamentary clouds is represented by polytropic cylinders ([Ostriker 1964b](#), [Viala & Horedt 1974b](#)), in which the gas pressure (from thermal or non-thermal motions) is parametrised by a polytropic EOS, as shown in eq. (2.16)

$$p = K\rho^{\gamma_p}. \quad (3.8)$$

The constant K is a measure of the cloud's entropy (a limit case for a polytropic EOS is an isothermal gas, in which $K = c_s^2$). Usually, the *polytropic exponent* is $\gamma_p = 1 + 1/n$, where the *polytropic index* n can have values in the range $n \leq -1$ or $n > 0$ (the range $-1 < n < 0$ corresponds to negative values of γ_p and is therefore unphysical). For $0 \leq \gamma_p \leq 1$ ($n \leq -1$) polytropic cylinders have infinite radii and infinite mass per unit length, whereas for $\gamma_p > 1$ ($n > 0$) the density and pressure become zero at some finite radius and therefore have finite masses per unit length. For $\gamma_p = 1$ ($n \rightarrow -\infty$) the gas is isothermal, whereas for $\gamma_p \rightarrow 0$ ($n = -1$) the equation of state becomes “logatropic”, $p \propto \ln \rho$ ([Lizano & Shu 1989](#)). This latter form has been used to model the non-thermal support in molecular clouds in which supersonic line widths are observed. Logatropic cylinders have infinite radius and infinite mass per unit length ([Fiege & Pudritz 2000](#)). Negative index polytropes ($0 \leq \gamma_p < 1$) were first used as models for thermally-supported interstellar clouds heated by an external flux of photons or cosmic rays [Shu et al. \(1972\)](#). On the other hand, the polytropic temperature $T \propto (p/\rho)^{1/2}$ can be considered a measure of the contribution of non-thermal (turbulent) motions to the support of the cloud. In this case negative index polytropes reproduce the observed increase of non-thermal line width with size observed in molecular clouds. The critical mass per unit length of eq. (3.4) can be generalised to

include the presence of non thermal gas motions. Then $\mu_{\text{line,vir}} = 2\sigma_{\text{tot}}^2/G$, also known as virial mass per unit length, and $\sigma_{\text{tot}} = \sqrt{c_s^2 + \sigma^2}$ is the total velocity dispersion (thermal plus non thermal motions).

Using the polytropic EOS (3.8), the equation of hydrostatic equilibrium eq. (3.5) with the advective term set equal to 0 reduces to the standard cylindrical Lane-Emden equation

$$\frac{1}{\xi} \frac{d}{d\xi} \left(\xi \frac{d\theta}{d\xi} \right) = \pm \theta^n, \quad (3.9)$$

for the non-dimensional density θ and radius ξ defined by

$$\varpi = \varpi_0 \xi = \left[\frac{\mp(1+n)K}{4\pi G \rho_c^{1-1/n}} \right]^{1/2} \xi, \quad \rho = \rho_c \theta^n. \quad (3.10)$$

In eq. (3.9) and (3.10) the upper (lower) sign is for $0 \leq \gamma_p < 1$ ($\gamma_p > 1$), and the subscripts “c” and “s” label values at the center (axis of the cylinder) and at the surface of the filament, respectively. Special cases have already been solved in numerical and analytical models. In fact, solutions of eq. (3.9) with boundary conditions $\theta = 1$ and $d\theta/d\xi = 0$ at $\xi = 0$ have already been obtained by [Viala & Horedt \(1974a\)](#) for $0 < \gamma_p < 1$, by [Stodólkiewicz \(1963\)](#) and [Ostriker \(1964b\)](#) for $\gamma_p = 1$, and by [Ostriker \(1964b\)](#) for $\gamma_p > 1$. The mass per unit length μ is defined as

$$\mu = 2\pi \int_0^{\varpi_s} \rho \varpi d\varpi = \mp \frac{(1+n)K\rho_c^{1/n}}{2G} \xi_s \theta'_s, \quad (3.11)$$

where eq. (3.9) has been used to simplify the integral.

Different models can have different units of measure, thus for a comparison between different models for the radial density profiles, a normalisation of the radial coordinate ϖ to the same length scale is necessary. To the lowest order in a series expansion for small radii, the density profile of polytropic filaments is $\rho(\varpi) \approx \rho_c(1 - \varpi^2/\varpi_{\text{core}}^2 + \dots)$. The “core radius” ϖ_{core} is then

$$\varpi_{\text{core}} = \frac{2\varpi_0}{\sqrt{\mp n}} = \left(\frac{1+n}{n} \right)^{1/2} \frac{\sigma_c}{(\pi G \rho_c)^{1/2}}, \quad (3.12)$$

where $\sigma_c = (p_c/\rho_c)^{1/2}$ is the velocity dispersion on the filament’s axis². An observational value is $\sigma_c \approx 0.26 \text{ km s}^{-1}$ ([Arzoumanian et al. 2013](#)) and then using the fiducial value

²A comparison with an analogous series expansion of the softened power-law profile (eq. 3.1) leads to the identification $\varpi_{\text{core}} = (2/\alpha)^{1/2} \varpi_{\text{flat}}$. Since $\alpha \approx 2$, $\varpi_{\text{core}} \approx \varpi_{\text{flat}}$.

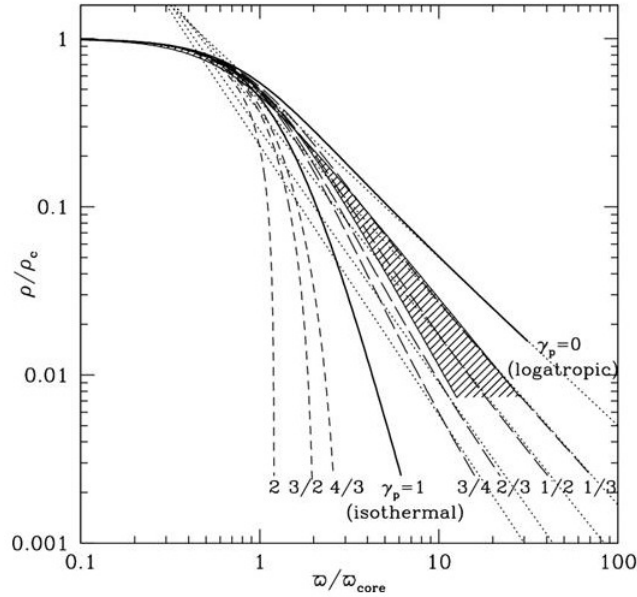


Figure 3.1: density profiles (normalised to the central density ρ_c) of polytropic cylinders with $\gamma_p = 2, 3/2, 4/3$ ($n = 1, 2$ and 3 , *short-dashed* lines, from left to right) and $\gamma_p = 1/3, 1/2, 2/3$ and $3/4$ ($n = -3/2, -2, -3$ and -4 , *long-dashed* lines, from right to left). The *thick solid* lines show the density profiles of an isothermal ($\gamma_p = 1$, or $n = \pm\infty$) and a logatropic ($\gamma_p = 0$, or $n = -1$) cylinder. *Dotted* lines are the singular solutions given by eq. (3.14). The radius is normalised to the core radius ϖ_{core} defined by eq. (3.12). The hatched area corresponds to the observed mean density profile of filaments in IC5146, given by eq. (3.1) with $\alpha = 1.6 \pm 0.3$. From Toci & Galli (2015a).

$n_c \approx 2 \times 10^4 \text{ cm}^{-3}$ and setting $n = -2$ the core radius is

$$\varpi_{\text{core}} \approx 0.047 \left(\frac{\sigma_c}{0.26 \text{ km s}^{-1}} \right) \left(\frac{n_c}{2 \times 10^4 \text{ cm}^{-3}} \right)^{-1/2} \text{ pc}. \quad (3.13)$$

Fig. 3.1 shows a comparison between the density profiles of various cylindrical polytropes of positive and negative index, as function of radius normalised to ϖ_{core} . The longitudinally averaged density profiles of the filaments in IC5146, given by eq. (3.1) with $\alpha = 1.6 \pm 0.3$ (Arzoumanian et al. 2011), are well reproduced by cylindrical polytropes with $1/3 \lesssim \gamma_p \lesssim 2/3$ ($-3 \lesssim n \lesssim -3/2$) at least over the observed radial extent of the filaments (from $\varpi \approx 0.1 \varpi_{\text{core}}$ to $\varpi \approx 10 \varpi_{\text{core}}$). Overall, the single value $\gamma_p \approx 1/2$ ($n = -2$) provides a good fit to the data, at least for this sample of filaments. We will discuss the implications of these results in Sect. 3.2.2.

3.1.4 Power-law behaviour at large radius

Other kind of solutions can be obtained from eq. (3.9) in addition to the regular one. These solutions are singular (or scale-free) solutions for $0 \leq \gamma_p < 1$ ($n < -1$), and have a power-law behaviour intermediate between $\rho \propto \varpi^{-1}$ (for $\gamma_p = 0$) and $\rho \propto \varpi^{-2}$ (for $\gamma_p \rightarrow 1$), given by

$$\rho(\varpi) = \left[\frac{(1-n)^2 \pi G}{-(1+n)K} \right]^{n/(1-n)} \varpi^{2n/(1-n)}, \quad (3.14)$$

as found by [Viala & Horedt \(1974b\)](#). The mass per unit length of these models is

$$\begin{aligned} \mu(\varpi) &= (1-n)\pi \left[\frac{(1-n)^2 \pi G}{-(1+n)K} \right]^{n/(1-n)} \varpi^{2/(1-n)} \\ &= (1-n)\pi \varpi^2 \rho(\varpi), \end{aligned} \quad (3.15)$$

that reaches the constant value $\mu \rightarrow a^2/G$ if $\gamma_p \rightarrow 1$.

The scale-free solutions are reported in [Fig. 3.1](#) along with the regular solutions. As shown by [Fig. 3.1](#), these solutions are the asymptotic behaviour around which the regular solutions oscillate with decreasing amplitude for $\varpi \rightarrow \infty$. This asymptotic behaviour is followed by both polytropic spheres and cylinders.

However, a spherical singular solution exists also for $\gamma_p = 1$ (the singular isothermal sphere), while this is not true in cylindrical geometry³. In fact, while for spheres the amplitude of the oscillatory component decreases as $\varpi^{-1/2}$ for $\gamma_p = 1$, for cylinders it reaches a constant value for $\gamma_p \rightarrow 1$, and the period of oscillation becomes infinite: the isothermal cylinder converges to the singular solution eq. (3.14) only at infinite radius.

For these reasons, if a quasi-isothermal filamentary clouds goes through an evolutionary stage independent of the initial and boundary conditions, but still far from the ultimate equilibrium state, a radial density profile closer to $\rho \propto \varpi^{-2}$ rather than $\rho \propto \varpi^{-4}$ should be expected. An example of this behaviour is in the self-similar collapse solutions of quasi-isothermal filaments by [Kawachi & Hanawa \(1998\)](#).

³For a logatropic equation of state, a singular solution exist in cylindrical geometry but not in spherical geometry, instead.

3.2 Support against gravity

3.2.1 Thermal support

The isothermal Stódołkiewicz-Ostriker profile can be used as a reference to probe if the gas is not isothermal, and to give an estimate of the non isothermal pressure contribution. If a deviation from the isothermal density profile is observed, it is an indication of temperature gradients increasing outwards that produce a larger thermal pressure gradient than an isothermal gas. Models of radiative transfer of the infrared emission support this hypothesis. For example, [Stepnik et al. \(2003\)](#) found significant radial gradients in the dust density profiles. Whereas [Palmeirim et al. \(2013\)](#) found that the dust temperature T_d increases outward from $\sim 10\text{--}12$ K on the axis to ~ 14 K at $\varpi \approx 0.5$ pc in the B211 filament. [Ysard et al. \(2013\)](#) found the same behaviour to ~ 18 K in the L1506 filament.

The gas temperature T_g should have gradients as well, and they could be also larger. As already reported in the Introduction, the temperature of gas and dust can be different, depending on the coupling of the dust and gas temperatures. At the typical densities on the filament's axis ($\sim 10^4 \text{ cm}^{-3}$) a small coupling is expected, and then the gas should be significantly hotter than the dust in the outer regions (see e.g. [Galli et al. 2002](#)). The magnitude of the gradient observed in the gas temperature can be measured using the polytropic models of Sect. 3.1.3 to reproduce observational data. Fig. 3.2 shows the radial behaviour of polytropic temperature $T \propto (p/\rho)^{1/2}$ for the same models shown in Fig. 3.1. In the range of polytropic exponents that fit the density profiles of observed filaments in IC5146, the polytropic temperature increases by a factor $\sim 5\text{--}12$ from the filament's axis to the boundary, fixed at $\rho_s \approx 10^{-2}\rho_c$ or $\varpi_s \approx 10 \varpi_{\text{core}}$ (that leads to a radius of about 1 pc, where the filaments merge with the ambient medium).

The polytropic temperature can also give an estimate of the gas temperature. With this identification the expected filament's surface temperature is $T_s \sim 70\text{--}170$ K, assuming a central temperature $T_c = 14$ K as observed from Herschel data. Such high temperature are not observed, in fact gradients of gas temperature in prestellar cores, as reported in the Introduction, are much shallower in agreement with the predictions of theoretical models. Therefore, thermal pressure cannot be the only support and other contribution are needed.

3.2.2 Non-thermal support

Other contributions to the stability of the cloud can come from pressure due to turbulence and magnetic field (large-scale or wave-like). Again, we can use polytropic EOS

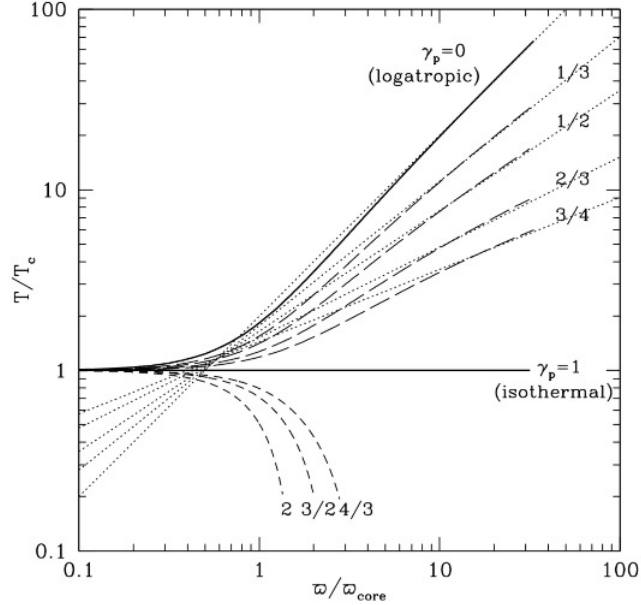


Figure 3.2: Radial profiles of the polytropic temperature T (normalised to the central temperature value T_c) of polytropic cylinders with values of γ_p (or n) as in Fig. 3.1. The *thick solid* lines show the temperature profiles of an isothermal ($\gamma_p = 1$, or $n = \pm\infty$) and a logatropic ($\gamma_p = 0$, or $n = -1$) cylinder. *Dotted* lines correspond to the singular solutions given by eq. (3.14). The radius is normalised to the core radius ϖ_{core} as in Fig. 3.1. From Toci & Galli (2015a).

to model their effects under the hypothesis that their contributions can be modelled as isotropic pressure components.

As an example, a work made by Walén (1944) showed that in the limit of small amplitude and small wavelength, and adding the hypothesis of negligible damping, Alfvén waves behave as a polytropic gas with $\gamma_p = 1/2$, a value that can be consistent with the observations, as shown in Sect. 3.1.3. This may imply that the filaments observed by *Herschel* are radially supported against gravitational collapse by non-thermal motions associated to Alfvénic “turbulence”. This contribution can be modelled as a superposition of hydromagnetic (magnetosonic) waves (Fatuzzo & Adams 1993).

Supposing that small-amplitude Alfvén waves ($\gamma_p = 1/2$ polytropic law) are a major contribution to the the pressure, observationally molecular transitions should have a non-thermal line width increasing by a factor ~ 3 from the axis to the filament boundary, and a behaviour at large radii $\sim \rho^{-1/4}$ (or $\varpi^{1/3}$). At the state of the art the available

date cannot allow any conclusion on the strength and spatial distribution of non-thermal motions within filamentary clouds. Hacar & Tafalla (2011) found that in L1517 the non-thermal line width of molecular transitions like C¹⁸O and SO is everywhere subsonic ($\sigma_{\text{nt}} < a$) and almost uniform, with velocity dispersion $\sigma_{\text{nt}} = 0.1 \pm 0.04 \text{ km s}^{-1}$ across the sampled region. In the B213 filament Qian et al. (2012) found that the velocity dispersion on the axis of is slightly supersonic ($\sigma_{\text{nt}} \approx 0.3 \text{ km s}^{-1}$), while millimetre line observations showed that self-gravitating filaments have intrinsic, suprathreshold linewidths $\sigma_{\text{nt}} \gtrsim a$ (Arzoumanian et al. 2013). In a case slightly different as massive filament like DR21 ($N_c \approx 10^{23} \text{ cm}^{-2}$, $\mu \approx 4 \times 10^3 M_\odot \text{ pc}^{-1}$) Schneider et al. (2010) found that the velocity dispersion increases towards the filament's axis, where it reaches $\sigma_{\text{nt}} \approx 1 \text{ km s}^{-1}$, while condensations in the filaments showed a lower velocity dispersions.

Numerical simulations and analytic considerations have found that the polytropic exponent of MHD turbulence depends on the dominant wave mode via the Alfvén Mach number \mathcal{M}_A , going from $\gamma_p \approx 1/2$ at low \mathcal{M}_A , where the slow mode dominates, to $\gamma_p \approx 2$ at large \mathcal{M}_A , where the slow and fast mode are comparable. For all these reasons, the representation of magnetohydrodynamic turbulence in terms of small-amplitude Alfvén waves is an oversimplification, even if useful to have an idea of the strength of this kind of contribution.

As shown in Sect. 3.1, negative-index cylindrical polytropes with appropriate values of γ_p are able to reproduce the observed radial density profiles of filaments and predict a core radius $\varpi_{\text{core}} \propto \sigma_c / \rho_c^{1/2}$. This result is in agreement with the observed uniformity of filament widths if σ_c scales as the square root of the central density, $\sigma_c \propto \rho_c^{1/2}$. Due to the fact that the central column density is $N_c \propto \rho_c \varpi_{\text{core}}$, we have that $\sigma_c \propto N_c^{1/2}$, since ϖ_{core} is constant. Observations (Arzoumanian et al. 2013) of filaments with central column densities above $\sim 10^{22} \text{ cm}^{-2}$ are in agreement with this trend. Theoretical studies found that the relation $\sigma \propto \rho^{1/2}$ is a good characterisation for the behaviour of the turbulent pressure during the relaxation processes leading to virialization in a strongly self-gravitating collapse flow, according to the numerical simulations of Vázquez-Semadeni et al. (1998). This could imply that, at least in the more massive filaments, the gas in the central parts is still undergoing turbulent dissipation (perhaps following accretion, as suggested by Hennebelle & André 2013).

3.3 Radial stability of polytropic filaments

Polytropic solutions in cylindrical symmetry are unstable to longitudinal perturbations of wavelength larger than some critical value. This perturbation is known as varicose (or

sausage) gravitational instability (Ostriker 1964a); This perturbation (and also its magnetic variant) can lead to the fragmentation of a filamentary cloud to a necklace of equally spaced dense cores, as observed i.e in high mass star formation by Fontani et al. (2016), and therefore it could be a promising mechanism for star formation. However, in analogy with the Bonnor-Ebert stability criterion in the case of spherical symmetry, it is important to determine the conditions for radial stability with respect to collapse to a line mass.

From the observations, stability considerations are usually derived using a comparison with the mass per unit length of the isothermal cylinder, μ_{iso} (eq. 3.4). However, as reported before, the stability properties of an isothermal cylinder are different from those of polytropic cylinders with $\gamma_p < 1$, because its mass per unit length reaches the finite value μ^{iso} as the radius of the cylinder increases to infinity, while for $\gamma_p < 1$ the mass increases with radius.

As a consequence, an isothermal filament is always radially stable: if a pressure p_s applied over an isothermal cylinder with fixed $\mu < \mu_{\text{iso}}$ increases, it induces in the filament a contraction, reducing its radius ϖ_s and core radius ϖ_{core} as $p_s^{-1/2}$, while its central density ρ_c grows as p_s^{-1} , but otherwise maintaining the same shape of the density profile. Conversely, for $0 \leq \gamma_p < 1$, also cylindrical polytropes become unstable if the external pressure becomes larger than some critical value. The instability extends to $\gamma_p = 4/3$ for spheres (the classical Bonnor-Ebert instability) but not for cylinders.

In analogy with the spherical case, the stability of polytropic cylindrical clouds to radial perturbations can be studied by solving the equation of radial motion for small perturbations. This equation becomes (Breysse et al. 2014)

$$\frac{d^2 h}{d\varpi^2} + \frac{3 - 4q}{\varpi} \frac{dh}{d\varpi} + \left[\frac{\omega^2}{f^2} + 8 \left(\frac{1}{\gamma} - 1 \right) q \right] \frac{h}{\varpi^2} = 0, \quad (3.16)$$

where $h = \delta\varpi/\varpi$ is the relative amplitude of the perturbation, ω is the frequency of the oscillations, γ is the adiabatic exponent, and we have defined

$$q \equiv \frac{G\mu\rho}{2p} = -\frac{(1+n)\xi\theta'}{4\theta}, \quad (3.17)$$

and

$$f \equiv \frac{1}{\varpi} \left(\frac{\gamma p}{\rho} \right)^{1/2} = \frac{(4\pi G\rho_c)^{1/2}}{\xi} \left(\frac{\mp\gamma\theta}{1+n} \right)^{1/2}. \quad (3.18)$$

In order to obtain eq. (3.16) we assumed for simplicity that the perturbations occur adiabatically, $\delta p/p = \gamma \delta\rho/\rho$. It is important to notice that the adiabatic exponent γ that is related to the response of the cloud to small perturbations is not necessarily equal to the

polytropic exponent characterising the equilibrium structure discussed in Sec. 3.1. Only if the perturbation occurs on a time much longer than the characteristic time for internal redistribution of entropy, the adiabatic exponent γ is equal to γ_p (see examples and discussion in Sect. 3.3.2).

3.3.1 Isentropic filaments

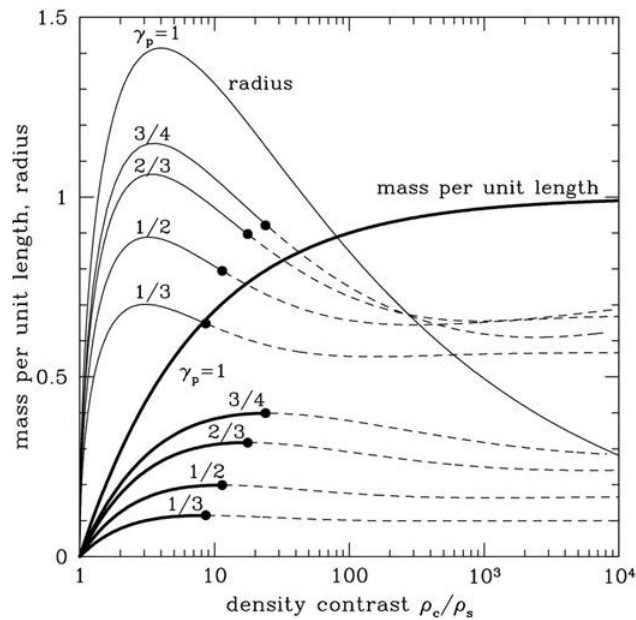


Figure 3.3: Mass per unit length μ (*thick curves*) and radius ϖ_s (*thin curves*) of cylindrical polytropes bounded a fixed external pressure as function of the density contrast ρ_c/ρ_s . The cases shown are, from bottom to top, $\gamma_p = 1/3, 1/2, 2/3, 3/4$ and 1 ($n = -1.5, -2, -3, -4$ and ∞). Dots on each curve indicate critical points. The stable and unstable parts of each sequence are shown by *solid* and *dashed* curves, respectively. The radius ϖ_s is in units of $[p_s/(4\pi G\rho_s^2)]^{1/2}$, the mass per unit length μ in units of $2p_s/G\rho_s$. From Toci & Galli (2015a).

The first case we analyse is an isentropic clouds, in which the entropy is both spatially uniform and constant during an adiabatic perturbation, and then we set $\gamma = \gamma_p$. Our goal is to obtain the condition of marginal stability, we set $\omega = 0$ and we solve eq. (3.16) imposing the boundary condition $dh/d\xi = 0$ at $\xi = 0$ to obtain the condition for h to remain finite on the axis (since eq. 3.16 is linear and homogeneous, the value of h at $\xi = 0$ is arbitrary). For any fixed value of the polytropic exponent γ_p , the critical point ξ_{cr} can

be determined setting the radius at which the Lagrangian variation in the pressure at the boundary is equal to zero,

$$\left(\frac{\delta p}{p}\right)_{\xi=\xi_{\text{cr}}} = -\gamma \left(2h + \varpi \frac{dh}{d\varpi}\right)_{\xi=\xi_{\text{cr}}} = 0. \quad (3.19)$$

If $\xi > \xi_{\text{cr}}$, the filament is unstable to radial collapse. At the critical point the density contrast is $(\rho_c/\rho_s)_{\text{cr}} = \theta_{\text{cr}}^{-n}$ and the mass per unit length is

$$\mu_{\text{cr}} = q_{\text{cr}} \left(\frac{2p_s}{G\rho_s}\right), \quad (3.20)$$

where

$$q_{\text{cr}} = -\frac{(1+n)\xi_{\text{cr}}\theta'_{\text{cr}}}{4\theta_{\text{cr}}}. \quad (3.21)$$

The values of ξ_{cr} , $(\rho_c/\rho_s)_{\text{cr}}$, and q_{cr} for different polytropes are listed in Table 3.1. Using the same value of the ratio p_s/ρ_s , the marginally stable configuration with the largest mass per unit length is the isothermal filament with $\gamma_p = 1$, for which $q_{\text{cr}} = 1$ and $\mu_{\text{cr}} = \mu_{\text{iso}}$. At the opposite end, the logatropic filament with $\gamma_p = 0$ has $q_{\text{cr}} = 0$. Thus, if we fix the values of the surface pressure and density, filaments with increasingly “softer” equations of state can support less and less mass per unit length, as found in the case of spherical polytropes (McKee & Holliman 1999).

Fig. 3.3 shows the radius and the mass per unit length of cylindrical polytropes with various values of γ_p between $\gamma_p = 1/3$ and 1 (from $n = -3/2$ to $-\infty$) as function of ρ_c/ρ_s and the position of the critical point on both sets of curves. The stability properties of polytropic filaments with $0 \leq \gamma_p < 1$ for the same value of the entropy parameter K and the ratio p_s/ρ_s are qualitatively similar: increasing ρ_c/ρ_s the filament first expands then contracts, until the filament becomes unstable when ρ_c/ρ_s becomes larger than the critical value listed in Table 3.1. Equilibria can be found above this critical value, but they are unstable to radial collapse. The instability occurs for increasingly larger values of ρ_c/ρ_s when γ_p increases (for $\gamma_p = 1$, the critical point is at $\xi_{\text{cr}} = \infty$). Using *Herschel* data of several filamentary clouds is possible to have an estimation of the central temperature, which is ~ 10 K. Computing the correspondent sound speed c_s^2 , the estimated mass per unit length is larger than μ_{iso} . Even if prestellar cores are mostly found in filaments that have $\mu > \mu_{\text{iso}}$, and that is considered a marker of the presence of gravitational instability (André et al. 2014), the fact that isothermal filaments have mass per unit line larger than μ_{iso} makes difficult to justify their formation by accretion (or by other processes).

Let us consider as an example the evolution of an isothermal filament with $\mu < \mu_{\text{iso}}$,

that is confined by an external constant pressure $p_s = c_s^2 \rho_s$. It increases its mass per unit length and, for our hypothesis, its temperature is uniform and constant with time. As the mass μ increases, the filament becomes more and more condensed at the centre, due to the fact that its density contrast ρ_c/ρ_s increases as $(1 - \mu/\mu_{\text{iso}})^{-2}$. At the same time, the flat core region shrinks as $(1 - \mu/\mu_{\text{iso}})$, and the outer radius first expands then contracts as $[(1 - \mu/\mu_{\text{iso}})(\mu/\mu_{\text{iso}})]^{1/2}$ (Fischera & Martin 2012). As $\mu \rightarrow \mu_{\text{iso}}$, the filament approaches a delta-like line mass of zero radius and infinite density on the axis. At the same time, while the filament evolves, it is subject to the varicose instability and can fragment into a chain of cores, but can never reach a stage with $\mu > \mu_{\text{cr}}$. This is different for non-isothermal filaments. In fact, for actual filaments the ratio p_s/ρ_s in eq. (3.20) is much larger than c_s^2 , the value expected for isothermal gas. If filamentary clouds are pressure bounded, p_s must be equal to the pressure exerted on the filament by the surrounding intercloud medium, where the dominant component of the pressure is due to turbulent motions.

Table 3.1: Critical points for isentropic cylindrical polytropes. Fixing the the values of the surface pressure and density, the marginally stable configuration with the largest mass per unit length is the isothermal filament, with $q_{\text{cr}} = 1$, while the logatropic filament with has $q_{\text{cr}} = 0$. This implies that filaments with increasingly “softer” equations of state can support less and less mass per unit length. From Toci & Galli (2015a).

n	γ_p	ξ_{cr}	$(\rho_c/\rho_s)_{\text{cr}}$	q_{cr}
-1	0	6.62	6.05	0
-1.01	0.0099	6.59	6.10	0.0272
-1.5	1/3	5.52	8.61	0.115
-2	1/2	4.93	11.4	0.199
-3	2/3	4.28	17.6	0.317
-4	3/4	3.92	23.9	0.399
-5	0.8	3.68	32.8	0.459
-10	0.9	3.13	80.0	0.626
-20	0.95	2.76	228	0.752
-30	0.967	2.60	441	0.812
-40	0.975	2.50	701	0.846
$-\infty$	1	∞	∞	1

3.3.2 Non-isentropic filaments

In Sect. 3.1 we showed that filamentary clouds are well reproduced by cylindrical polytropes with $1/3 \lesssim \gamma_p \lesssim 2/3$. For this reason their density contrast cannot exceed the

value $\rho_c/\rho_s = 8.61\text{--}17.6$ (see Table 3.1) or they would collapse to a line mass. However, observational results reported in Sect. 3.1 show that the density contrasts measured by *Herschel* are of the order of ~ 100 . In analogy with the case of spherical clouds, this limitation can be overcome if the cloud is non-isentropic ($\gamma \neq \gamma_p$).

McKee & Holliman (1999) found that the assumption of isentropy (adopted in most studies of polytropes) is in general not valid for molecular clouds. This comes from the fact that a contribution to the pressure supporting the cloud against its self-gravity may be provided by non-thermal components whose behaviour is not isentropic: for example, small-amplitude Alfvén waves have $\gamma_p = 1/2$ and $\gamma = 3/2$. Non-isentropic polytropes can be stable for larger density contrasts than isentropic clouds. We can reduce the range in analysis because polytropes with $\gamma < \gamma_p$ are convectively unstable according to the Schwarzschild criterion, and then we will study only values of $\gamma > \gamma_p$. In order to find the critical point ξ_{cr} of non-isentropic cylindrical polytropes, eq. (3.16) is solved for a fixed γ_p and arbitrary $\gamma > \gamma_p$. The results are shown in Table 3.2, listing the values of ξ_{cr} , $(\rho_c/\rho_s)_{\text{cr}}$ and q_{cr} for polytropes with $\gamma_p = 1/3, 1/2$ and $2/3$ for various values of γ . Like the case of spherical polytropes, the critical points go to larger and larger values of the density contrast ρ_c/ρ_s as γ increases. At a threshold value γ_∞ , the critical point reaches $\xi_{\text{cr}} = \infty$ and the density profile approaches that of a singular polytropic cylinder. The value of $q_{\text{cr}} = q_\infty$ at this point can be easily determined substituting eq. (3.14) into eq. (3.16),

$$q_\infty = \frac{\gamma_p}{2(2 - \gamma_p)}. \quad (3.22)$$

The threshold value of the adiabatic exponent, γ_∞ can also be obtained in an analytical way. For a singular polytropic cylinder, eq. (3.16) with $\omega = 0$ has constant coefficients, and the characteristic equation has two real and negative roots if γ is larger than

$$\gamma_\infty = \gamma_p(2 - \gamma_p), \quad (3.23)$$

corresponding to h exponentially decreasing with ξ . The values of q_∞ and γ_∞ for $\gamma_p = 1/3, 1/2$ and $2/3$ are also listed in Table 3.2. Non-isentropic polytropes are more stable than their isentropic counterparts as they can support larger centre-to-surface density contrasts. For $\gamma > \gamma_\infty$, polytropic filaments are unconditionally stable for any ρ_c/ρ_s .

In Fig. 3.4 are summarised the stability properties of cylindrical polytropes in the γ_p – γ plane. In cylindrical geometry the polytropic exponent $\gamma_p = 1$ is a critical value that has the same role of $\gamma_p = 4/3$ for spherical polytropes: while spheres with $\gamma_p > 4/3$ are unconditionally stable to small perturbations, cylinders become stable already for $\gamma_p > 1$ (McCrea 1957). In the case $\gamma_p = 1/2$, a value in agreement with the observed radial

Table 3.2: Stability of non-isentropic cylindrical polytropes. The critical points goes to larger and larger values of the density contrast ρ_c/ρ_s as γ increases. The density profile approaches the one of a singular polytropic cylinder at a threshold value γ_∞ , where the critical point reaches $\xi_{\text{cr}} = \infty$. From Toci & Galli (2015a).

$\gamma_p = 1/3$			
γ	ξ_{cr}	$(\rho_c/\rho_s)_{\text{cr}}$	q_{cr}
1/3	5.52	8.61	0.115
0.4	10.3	20.2	0.111
$\gamma_\infty = 5/9$	∞	∞	$q_\infty = 1/10$
$\gamma_p = 1/2$			
γ	ξ_{cr}	$(\rho_c/\rho_s)_{\text{cr}}$	q_{cr}
1/2	4.93	11.4	0.199
0.6	10.7	38.0	0.188
0.7	124	1096	0.163
$\gamma_\infty = 3/4$	∞	∞	$q_\infty = 1/6$
$\gamma_p = 2/3$			
γ	ξ_{cr}	$(\rho_c/\rho_s)_{\text{cr}}$	q_{cr}
2/3	4.28	17.6	0.317
0.7	5.18	25.2	0.316
0.8	14.1	153	0.282
$\gamma_\infty = 8/9$	∞	∞	$q_\infty = 1/4$

density profiles of filamentary clouds, the threshold value for stability (from eq. 3.23) is $\gamma_\infty = 3/4$. In the case of a “soft” equation of state the stability condition is almost the same for cylinders and spheres: for $\gamma_p \ll 1$, a first-order approximation gives $\gamma_\infty \approx 2\gamma_p$ for cylinders and $\gamma_\infty \approx (16/9)\gamma_p$ for spheres. For larger values of γ_p , cylinders are intrinsically more stable than spheres in the γ_p - γ plane. A pressure-bounded isothermal cylinder, for example, is always stable with respect to an arbitrary increase in the external pressure, whereas an isothermal sphere is not. For the range of polytropic exponents allowed by the observations of the radial density profiles ($1/3 \lesssim \gamma_p \lesssim 2/3$, see Sect. 2), the stability properties of cylindrical and spherical clouds are very similar.

3.4 Summary

In this Chapter we presented an analysis of filamentary clouds’ stability in analogy with the theoretical studies of spherical clouds made by McKee & Holliman (1999) but

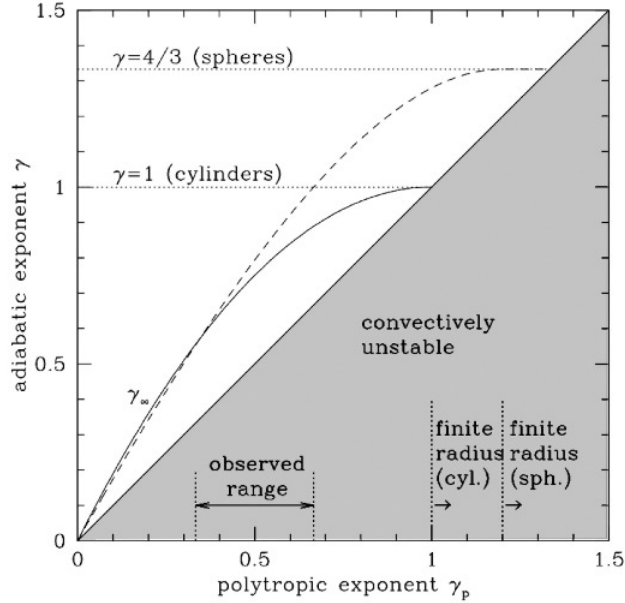


Figure 3.4: Stability properties of cylindrical and spherical polytropes in the γ_p - γ plane. Polytropes in the $\gamma < \gamma_p$ region (*shaded*) are convectively unstable. On the line $\gamma = \gamma_p$, polytropic cylinders (spheres) are isentropic, and become unstable at some finite $(\rho_c/\rho_s)_{cr}$ if $\gamma < 1$ ($\gamma < 4/3$). Above the curve labelled γ_∞ (*dashed* for spheres) cylindrical polytropes are unconditionally stable even for $\rho_c/\rho_s = \infty$. Cylindrical (spherical) polytropes have finite radii for $\gamma_p > 1$ ($\gamma_p > 6/5$) as indicated by the vertical *dotted* lines. The stability properties of spherical polytropes are from McKee & Holliman (1999). From Toci & Galli (2015a).

in cylindrical symmetry, underlying the request for non-isentropic models to reproduce observational results that suggest large density contrasts. The stability properties of polytropic cylinders can be characterised, like in the case of spherical polytropes, using the polytropic exponent γ_p , related to the spatial properties of the filament, and using the adiabatic exponent γ , that characterises the temporal response of the cloud to adiabatic perturbations.

The typical core-envelope structure and the uniformity of the observed properties of filamentary molecular clouds, like the flat-density inner part of size and the power-law envelope and the uniform width (André et al. 2014), indicate polytropic cylinders as a good model to study their main physical characteristics. The observed power-law behaviour of the density at radii larger than the core radius can not be reproduced by isothermal models, nor they can explain the existence of filaments with mass per unit length larger than the

limiting value for an isothermal cylinder. Conversely, the observed radial density profiles of filamentary clouds (Arzoumanian et al. 2011) are well reproduced by negative-index cylindrical polytropes with $1/3 \lesssim \gamma_p \lesssim 2/3$ ($-3 \lesssim n \lesssim -3/2$). This result indicates either outward-increasing temperature gradients, or the presence of a dominant non-thermal contribution to the pressure. The first case predicts a gas temperature at the filament's surface unrealistically high (~ 100 K). Non-thermal support, perhaps in the form of a superposition of small-amplitude Alfvén waves (for which $\gamma_p = 1/2$) can provide a possible mechanism of support. Also, the mass per unit length of negative-index polytropes is not limited, but shows a dependence on the pressure and density at the surface, if the filaments are pressure confined by the ambient medium.

Cylindrical polytropes that have negative-index present a uniform width, as observed (André et al. 2014), if the central velocity dispersion σ_c is proportional to the square root of the central density ρ_c (or the central column density N_c). This relation seems to be satisfied at least by the most dense filaments observed i.e in Arzoumanian et al. (2013) and has been found in numerical simulations of self-gravitating collapse flows Vázquez-Semadeni et al. (1998). The density profile of polytropic filaments, once outside the core radius, has often a power-law behaviour. This implies considerations on the cloud's thermodynamics and equation of state: independently on geometry, both spherical and cylindrical polytropes approach at large radii the same power-law behaviour in radius with a slope equal to $-2/(2 - \gamma_p)$, that reaches -2 for a quasi isothermal gas. However, for cylinders, this power-law behaviour is recovered at increasingly larger radii for $\gamma_p \rightarrow 1$ (at infinite radius for $\gamma_p = 1$).

Pressure-bounded polytropic cylinders with $1/3 \lesssim \gamma_p \lesssim 2/3$ can support a mass per unit length as large as observed depending on the conditions at the surface. However, if we suppose also that they are isentropic, their density contrast cannot be larger than about a factor of 10–20. At the same time, as the spherical case (McKee & Holliman 1999), non-isentropic cylinders are stable also at larger density contrasts (in principle even infinite) with respect to adiabatic pressure perturbations. Since magnetic fields and turbulence (that in this Chapter we parametrised as a superposition of Alfvén waves) behave as non-isentropic pressure components, this stresses that isentropic (and, in particular, isothermal) models are inadequate to represent and characterise the structure and the stability properties of filamentary clouds.

4

Equilibrium of magnetohydrostatic filamentary structures

In the previous Chapter we studied the structure and stability of hydrostatic cylindrical polytropes, which is a rough approximation for a model of interstellar filaments. This approximation allowed us to interpret the observational results obtained by the *Herschel Space Observatory*. In analogy with previous studies of spherical clouds and cores, we derived for the observed radial density profiles of filaments a narrow range of γ_p ($1/3 \lesssim \gamma_p \lesssim 2/3$) that fit the observed data. These values correspond to negative values of the polytropic index n . In particular, a good fit is obtained with $\gamma_p \approx 1/2$ ($n \approx -2$), the polytropic exponent that characterises the pressure of a superposition of low-amplitude undamped Alfvén waves. Magnetic fields are present in molecular clouds, and as showed in the Introduction, their contributions to the stability of filaments cannot be neglected. Therefore, it is necessary to study also the properties of magnetised filaments.

Much of what is known of magnetostatic (MS) equilibria in plasma physics and astrophysics comes from studying systems with one ignorable coordinate, i.e axisymmetric systems. In the three-dimensional case, no one has ever been able to find non-axisymmetric solutions of the MS equations for a self-gravitating fluid, and their actual existence has remained dubious (Galli 2005).

The first work in this field was done by Chandrasekhar & Fermi (1953), in order to study the stability of galactic spiral arms. After that, models of filamentary clouds made with magnetic configurations possessing helical symmetry have also been explored. (i.e Nakamura et al. 1995 or Fiege & Pudritz 2000)

As already reported in the Introduction, observations of the polarisation of background stars in the optical and near infrared found that the field is generally uniform and perpendicular to the filament (For example in the B211/B213/L1495 region in Taurus Palmeirim et al. 2013). Studies of molecular clouds found that the plane of the sky ori-

entation of their elongation and the same projection of magnetic field is bimodal: clouds either tend to be parallel or perpendicular to the magnetic field. This trend has been confirmed by the Planck collaboration. Soler et al. (2016) analysed the relative orientation between density structures and polarization, finding that most of the filaments are mostly aligned with their magnetic field. Planck Collaboration (2016) found that filaments at high column density tends to be perpendicular to the magnetic field, whereas at low column density they tend to be aligned.

For all these reasons, the magnetic field should play an important role in determining the observable properties of filamentary clouds. In this Chapter we will study the properties of magnetised polytropes in cylindrical geometry. In particular, we will underline the conditions for force balance in the radial direction. Our hypothesis is that the evolution of real filaments can be approximated as a series of magnetostatic solutions as filaments accrete more material from the surrounding environment. The models developed are then magnetostatic by design. As in the previous Chapter, this does not necessarily imply zero a velocity field everywhere, as long as the accretion speed becomes either subsonic or directed mostly parallel to the filament's axis in the central parts of the filament.

4.1 Magnetized envelopes

In a cylindrical system of coordinates, any solenoidal vector field \mathbf{B} can be expressed as a linear combination of a certain basic *toroidal* B_φ and *poloidal* (\mathbf{B}_p) fields (Chandrasekhar 1961), given by

$$\mathbf{B}_p = \nabla \times \left(\frac{\Phi}{2\pi\varpi} \hat{\mathbf{e}}_\varphi \right), \quad B_\varphi = \frac{\Psi}{2\pi\varpi}. \quad (4.1)$$

defined in terms of the scalar functions $\Phi(\varpi, z)$ and $\Psi(\varpi, z)$. In addition, to have zero divergence, the toroidal and poloidal fields are characterized by vanishing radial component and vanishing radial component of the curl, respectively¹.

Following the previous Chapter, we assume again the polytropic EOS,

$$p = K\rho^{\gamma_p}. \quad (4.2)$$

We consider a self-gravitating magnetized fluid body, satisfying the ideal magnetostatic

¹Notice that this terminology, *Stratton-Chandrasekhar's*, is different from the one commonly adopted in astrophysics, where is customary to call poloidal a field with components only along r and θ , and toroidal a field with only a component along φ .

equilibrium equations and the Poisson's equation for the gravity potential. The MHD equations from Section 2.1 become

$$-\nabla\mathcal{V} + \frac{1}{\rho}\nabla p + \mathbf{F}_L = 0, \quad (4.3)$$

$$\nabla^2\mathcal{V} = 4\pi G\rho, \quad (4.4)$$

where

$$\mathbf{F}_L \equiv \frac{1}{4\pi\rho}(\nabla \times \mathbf{B}) \times \mathbf{B} \quad (4.5)$$

is the Lorentz force per unit mass. Using the definitions (4.1), the Lorentz force becomes

$$\mathbf{F}_L = -\frac{1}{16\pi^3\rho\varpi^2}[\mathcal{S}(\Phi)\nabla\Phi + \Psi\nabla\Psi + \nabla\Phi \times \nabla\Psi] \quad (4.6)$$

where \mathcal{S} is the Stokesian operator

$$\mathcal{S}(\Phi) = \frac{\partial^2\Phi}{\partial\varpi^2} + \frac{\partial^2\Phi}{\partial z^2} - \frac{1}{\varpi}\frac{\partial\Phi}{\partial\varpi}. \quad (4.7)$$

If the condition of no Lorentz force in the azimuthal direction is required $\nabla\Phi \times \nabla\Psi = 0$, which implies $\Psi = \Psi(\Phi)$. The Lorentz force then reduces to

$$\mathbf{F}_L = -\frac{1}{16\pi^3\rho\varpi^2}\left[\mathcal{S}(\Phi) + \Psi\frac{d\Psi}{d\Phi}\right]\nabla\Phi, \quad (4.8)$$

This is a generalisation of the expression derived by Lizano & Shu (1989) in the case of a poloidal field (see also Li & Shu 1996 and Galli et al. 1999). In a magnetostatic configuration of equilibrium all the contributions from the Lorentz force have to be counterbalanced by the pressure or the gravity. The behaviour of the Lorentz force strictly depends from the intrinsic shape of the magnetic field. The hypothesis of a toroidal magnetic field added to the the poloidal one, previously been examined by Galli et al. (1999), changes the physics of the problem. Taking the dot product of the force equation (3.5) with \mathbf{B} it can be obtained the condition of force balance along field lines

$$\mathcal{V} + (1+n)K\rho^{1/n} = H(\Phi), \quad (4.9)$$

where $H(\Phi)$ is the Bernoulli constant. The condition of force balance across field lines

(along $\nabla\Phi$) is

$$-\frac{1}{16\pi^3\rho\varpi^2}\left[\mathcal{S}(\Phi) + \Psi\frac{d\Psi}{d\Phi}\right] = \frac{dH}{d\Phi}, \quad (4.10)$$

and Poisson's equation (3.6) then becomes

$$\begin{aligned} \frac{1}{\varpi}\frac{\partial}{\partial\varpi}\left[\varpi\left(\frac{dH}{d\Phi}\frac{\partial\Phi}{\partial\varpi} - \frac{1+n}{n}K\rho^{-1+1/n}\frac{\partial\rho}{\partial\varpi}\right)\right] + \\ \frac{\partial}{\partial z}\left(\frac{dH}{d\Phi}\frac{\partial\Phi}{\partial z} - \frac{1+n}{n}K\rho^{-1+1/n}\frac{\partial\rho}{\partial z}\right) = 4\pi G\rho. \end{aligned} \quad (4.11)$$

Eq. (4.8) and (4.10) show that $H(\Phi)$ is a potential for the Lorentz force, $\mathbf{F}_L = \nabla H(\Phi)$.

The two coupled PDEs (4.10) and (4.11) are the two equations governing the problem. In order to find a solution, one must specify the two functions $H(\Phi)$ and $\Psi(\Phi)$, and appropriate boundary conditions have to be applied. The hypothesis of neglecting the dynamical evolution of the cloud implies that the functional dependence of H and Ψ on the flux function Φ is an arbitrary choice. Even if in principle H and Ψ are arbitrary functions (due to the loss of information on the previous history of the filaments, Shu (1992)), not all the solutions would be physically meaningful for modelling molecular clouds. As discussed in the Introduction, the paths that lead to the formations of filamentary molecular clouds are not completely understood, then any requirements to reduce the arbitrariness in eq. (4.10) and (4.11) must be necessarily *ad hoc*.

4.1.1 Non-dimensional equations

Both the Eqs. (4.10) and (4.11) are valid under general azimuthal symmetry. In order to simplify the problem, we also assume cylindrical symmetry ($\partial/\partial z = 0$), reducing the problem to solve a system of two coupled ordinary differential equations. We define a non-dimensional radius ξ and density θ as in the previous Chapter.

$$\varpi = \varpi_0\xi, \quad \rho = \rho_c\theta^n, \quad (4.12)$$

where

$$\varpi_0 = \left[\frac{\mp(1+n)K}{4\pi G\rho_c^{1-1/n}}\right]^{1/2} \quad (4.13)$$

is the radial scale length. Here, as before, the subscripts “c” and “s” indicate quantities evaluated at the center and the surface of the filament, respectively. We also define the

non-dimensional magnetic flux ϕ , enthalpy h and toroidal flux function ψ as

$$\Phi = \left[\frac{\mp \pi (1+n)^3 K^3}{G^2 \rho_c^{1-3/n}} \right]^{1/2} \phi, \quad (4.14)$$

$$\frac{dH}{d\Phi} = \left[\frac{\mp G^2 \rho_c^{1-1/n}}{\pi (1+n) K} \right]^{1/2} \frac{dh}{d\phi}, \quad (4.15)$$

$$\Psi = \left[\frac{\mp 2\pi (1+n) K \rho_c^{1/n}}{G^{1/2}} \right] \psi, \quad (4.16)$$

Again, the upper (lower) sign is for $n \leq -1$ ($n > -1$), where n is the polytropic index.

In a nondimensional form, the components of the magnetic field are

$$B_z = B_0 b_z, \quad B_\varphi = B_0 b_\varphi, \quad (4.17)$$

where the scale factor B_0 is

$$B_0 = [\mp 4\pi (1+n) p_c]^{1/2}. \quad (4.18)$$

The field components are then

$$b_z = \frac{1}{\xi} \frac{d\phi}{d\xi}, \quad b_\varphi = \frac{\psi}{\xi}. \quad (4.19)$$

In the same way, the forces per unit volume acting on the system are: the pressure gradient,

$$-\frac{1}{\rho} \nabla P = \pm F_0 \frac{d\theta}{d\xi} \hat{\boldsymbol{e}}_\varphi, \quad (4.20)$$

the Lorentz force

$$\mathbf{F}_L = F_0 \frac{dh}{d\xi} \hat{\boldsymbol{e}}_\varphi, \quad (4.21)$$

and the gravitational force

$$-\nabla \mathcal{V} = -F_0 \left(\frac{dh}{d\xi} \pm \frac{d\theta}{d\xi} \right) \hat{\boldsymbol{e}}_\varphi, \quad (4.22)$$

where the scale factor F_0 is

$$F_0 \equiv [\mp 4\pi (1+n) G p_c]^{1/2} = G^{1/2} B_0. \quad (4.23)$$

Eq. (4.10) and (4.11) can be re-written in non-dimensional form using the definitions

(4.12)–(4.16),

$$-\frac{1}{\xi^2 \theta^n} \left[\left(\frac{d^2 \phi}{d\xi^2} - \frac{1}{\xi} \frac{d\phi}{d\xi} \right) \frac{d\phi}{d\xi} + \psi \frac{d\psi}{d\xi} \right] = \frac{dh}{d\xi}, \quad (4.24)$$

and

$$\frac{1}{\xi} \frac{d}{d\xi} \left[\xi \left(\frac{dh}{d\xi} \pm \frac{d\theta}{d\xi} \right) \right] = \theta^n. \quad (4.25)$$

In order for the magnetic field to be well-behaved near the axis of the cylinder, we must impose to eq. (4.24)–(4.25) the boundary conditions $\theta(0) = 1$ and $d\theta/d\xi(0) = 0$, as in the previous Chapter, plus the conditions $\xi^{-1} d\phi/d\xi \rightarrow \text{const.}$ and $\xi^{-1} \psi \rightarrow 0$ for $\xi \rightarrow 0$, that lead to $B_z(0) = \text{const.}$ and $B_\varphi(0) = 0$.

The possibility of a magnetic field to support (or to compress) a filamentary cloud depends from the strength of the radial profile and on the relative importance of the poloidal and toroidal components. This sentence can be justified using eq. (4.21) and (4.24), that show that in order to give support to the cloud an axial field must decrease with radius, whereas a toroidal field must decrease with radius more rapidly than ϖ^{-1} .

4.2 Special solutions

4.2.1 Force-free fields

Force free solution are important for their peculiar properties (see 2.1.1). In the literature, magnetic force-free configurations have been used to model solar prominences, where the Lorentz force is the dominant contribution. In the ISM these configurations can be used to model twisted filamentary clouds that cannot survive to disruptive magnetic effects if the configuration is not force-free (Carlqvist et al. 1998).

IF $h = 0$ the magnetic configuration is force-free, the equations for the density and the magnetic field are decoupled. Eq. (4.24) becomes an equation only for the field,

$$\left(\frac{d^2 \phi}{d\xi^2} - \frac{1}{\xi} \frac{d\phi}{d\xi} \right) \frac{d\phi}{d\xi} + \psi \frac{d\psi}{d\xi} = 0, \quad (4.26)$$

and eq. (4.25) becomes the ordinary Lane-Emden equation. There are solutions of eq. (4.26) that are known. For example, if $\psi = 0$ (poloidal field) the only regular solution is $\phi = A\xi^2$, with A arbitrary constant, and that correspond to the trivial case of an uniform axial field. If $\psi = k\phi$, with k constant, eq. (4.26) is linear and reduces to Bessel's equation with solution $\phi = C\xi J_1(k\xi)$, where $J_1(k\xi)$ is the Bessel function of the first kind of order 1 and C is a constant. In this case $b_z = CkJ_0(k\xi)$ and $b_\varphi = CkJ_1(k\xi)$. This is the solution found

by Lundquist in 1950. The field lines are helices that reverse direction and handedness because Bessel's functions are oscillatory. The Lundquist solution is one of a class of solutions that have oscillatory behaviour and that can be generated assuming a power-law dependence of ψ on ϕ .

In the next part, we limit our analysis to the case $\phi > 0$. Even if in general the flux function ϕ can change sign at one or more radii, thus the field reverses, the large-scale magnetic field inside a molecular cloud core should be the result of a smooth distortion of the relatively uniform field characteristic of giant molecular clouds and galactic disks, thus field reversal are not expected.

4.2.2 Constant- β solutions

The hypothesis that the plasma $\beta_z = (8\pi p/B_z^2)^{1/2}$ is spatially constant, implies that the total pressure is a scaled-up version of the total pressure. In this case, eq. (4.24) and eq. (4.25) become

$$\frac{1 + \beta_z^{-1}}{\xi} \frac{d}{d\xi} \left(\xi \frac{d\theta}{d\xi} \right) = \pm \theta^n. \quad (4.27)$$

Using the scaling transformation $\xi \rightarrow (1 + 1/\beta_z)^{-1/2} \xi$, this equation can be recognised as the ordinary Lane-Emden equation for unmagnetized polytropic cylinders. Thus, the analysis of the previous Chapter remains valid, with the spatial length scale ϖ_0 (and the core radius ϖ_{core}) increased by the factor $(1 + 1/\beta_z)^{1/2}$. In particular, for all values of the polytropic index n , the mass per unit length and its critical or maximum value determined for unmagnetised filaments are increased by the factor $1 + 1/\beta_z$. This is not true in general for a purely toroidal field: only for an isothermal equation of state a toroidal field with uniform $\beta_\phi = (8\pi p/B_\phi^2)^{1/2}$ produces a simple rescaling of the Lane-Emden equation (Stodólkiewicz 1963). Then, if $\gamma_p = 1$ the Stodólkiewicz-Ostriker density profile remains a good solution even in the presence of a helical magnetic field with constant β_z and β_ϕ .

4.2.3 Fiege & Pudritz's models

Fiege & Pudritz (2000) solved the equations of magnetostatic equilibrium for cylindrical clouds with an isothermal ($\gamma_p = 1$) or logatropic ($\gamma_p = 0$) equation of state. They chose a specific functional dependence of the magnetic field strength on density and radius, defined as

$$B_z = \Gamma_z \rho, \quad B_\phi = \Gamma_\phi \varpi \rho, \quad (4.28)$$

with Γ_z, Γ_φ being constants with arbitrary values. This choice is equivalent to the assumption that the ratio of magnetic flux to mass per unit length is the same in all cylindrical shells of the filament and that the toroidal component of the field is generated by a uniform twisting of the filament through a fixed angle. In our formalism, eq. (4.28) is rewritten as

$$\frac{d\Phi}{d\varpi} = 2\pi\Gamma_z\varpi\rho, \quad \Psi = 2\pi\Gamma_\varphi\varpi^2\rho. \quad (4.29)$$

Substituting these expressions in eq. (4.10) and (4.11), we find that

$$-\frac{1}{4\pi} \left[\Gamma_z^2 \frac{d\rho}{d\varpi} + \Gamma_\varphi^2 \frac{d}{d\varpi}(\varpi^2\rho) \right] = \frac{dH}{d\varpi}, \quad (4.30)$$

and

$$\frac{1}{\varpi} \frac{d}{d\varpi} \left[\varpi \left(\frac{dH}{d\varpi} - \frac{1+n}{n} K \rho^{-1+1/n} \frac{d\rho}{d\varpi} \right) \right] = 4\pi G \rho. \quad (4.31)$$

Eq. (4.30) can be integrated:

$$H = -\frac{1}{4\pi} \left(\Gamma_z^2 \rho + \Gamma_\varphi^2 \varpi^2 \rho \right) + \text{const.}, \quad (4.32)$$

and eq. (4.31) can be written as

$$\frac{1}{\varpi} \frac{d}{d\varpi} \left\{ \varpi \frac{d}{d\varpi} \left[H - (1+n) K \rho^{1/n} \right] \right\} = 4\pi G \rho. \quad (4.33)$$

Eq. (4.32) and (4.33) are the generalisation of eq. (D5) and (D7) of Fiege & Pudritz (2000). The problem reduces to the solution of the second order ordinary differential equation (4.33) for $\rho(\varpi)$, with H given by eq. (4.32). These generalised Fiege & Pudritz (2000) models have an asymptotic power-law behaviour at large radii depending on the polytropic index n ,

$$B_z \propto \rho \propto \varpi^{\frac{2n}{1-n}}, \quad B_\varphi \propto \varpi \rho \propto \varpi^{\frac{1+n}{1-n}}. \quad (4.34)$$

Then, the magnetic field becomes asymptotically dominated by the toroidal component decreasing as a power-law with exponent between -1 and 0 . The toroidal field has the effect of compressing the cloud.

4.3 Cores and envelopes of magnetised filaments

4.3.1 Series expansion for small radii

For symmetry requirements, on the filament's axis the toroidal component of the electric current needs to vanish and the axial current has to be finite. This leads to the fact that, to the lowest order for $\xi \rightarrow 0$, both ϕ and ψ have to decrease at least like ξ^2 . A series expansion

$$\phi \approx \phi_2 \xi^2 + \phi_4 \xi^4 + \dots, \quad \psi \approx \psi_2 \xi^2 + \dots, \quad (4.35)$$

gives

$$b_z \approx b_{0z} + b_{2z} \xi^2 + \dots, \quad b_\varphi \approx b_{1\varphi} \xi + \dots \quad (4.36)$$

with $b_{0z} = 2\phi_2$, $b_{2z} = 4\phi_4$, $b_{1\varphi} = \psi_2$. Substituting in eq. (4.24) and (4.25) the expansions (4.35) and the expansion for θ

$$\theta \approx 1 \pm \frac{1}{4} \xi^2 + \dots \quad (4.37)$$

we find the Lorentz force per unit mass near the axis,

$$F_L = -4F_0(b_{0z}b_{2z} + b_{1\varphi}^2)\xi + \dots \quad (4.38)$$

where $F_0 > 0$ is given by eq. (4.23). Every realistic model for filamentary clouds where the axial magnetic field decreases with radius following the density has the product $b_{0z}b_{2z}$ negative, and the Lorentz force related to the poloidal field is directed outward, providing support to the cloud. At the same time, the Lorentz force associated to the toroidal field is directed inward, squeezing the cloud. The behaviour of the density near the axis is $\rho/\rho_c \approx 1 - (\varpi/\varpi_{\text{core}})^2 + \dots$, where

$$\varpi_{\text{core}} \approx \frac{2\varpi_0}{[\mp n(1 + 4b_{0z}b_{2z} + 4b_{1\varphi}^2)]^{1/2}}. \quad (4.39)$$

The core radius is then increased by the poloidal field ($b_{0z}b_{2z} < 0$) and decreased by the toroidal field ($b_{1\varphi}^2 > 0$). This result can be a constraint for the strength and the morphology of the magnetic field near the filament's axis. As shown in the previous Chapter, the core radius that is expected for unmagnetised polytropic models is

$$\varpi_{\text{core}} \approx 0.047 \left(\frac{\sigma_c}{0.26 \text{ km s}^{-1}} \right) \left(\frac{n_c}{2 \times 10^4 \text{ cm}^{-3}} \right)^{-1/2} \text{ pc}. \quad (4.40)$$

As an example, a toroidal field in the core region that has $b_{1\varphi}^2 \approx 1$ (corresponding to $B_{\varphi,c} \approx \pi G^{1/2} \varpi \rho_c$ in physical units) would reduce the core radius by a factor of ~ 2 . Field strengths of this order are needed also in the models of Fiege & Pudritz (2000).

4.3.2 Scale-free solutions for large radii

In order to study the characteristics of polytropic magnetised filaments at large radii (to be more precise, at radii much larger than the core radius given by eq. 4.39), we look for asymptotic solutions of eq. (4.10) and (4.11) without making specific requirements on the magnetic field profile, imposing just a power-law behaviour. A power-law behaviour of the density in cylindrical polytropes is only allowed for $n \leq -1$, then we will restrict our analysis to this range of n .

For scale-free solutions, dimensional analysis implies that $|\mathbf{B}| \propto G^{1/2} \rho \varpi$. In addition, the enthalpy H and the toroidal field function Ψ must have a power-law dependence on Φ of the form:

$$\frac{dH}{d\Phi} = H_0 \left[\frac{G^2}{\pi |1+n| K^n} \right]^{\frac{1}{3-n}} \Phi^{-\frac{1-n}{3-n}}, \quad (4.41)$$

$$\Psi \frac{d\Psi}{d\Phi} = 4\alpha^2 \left[\frac{\pi^{2(2-n)} G^{1+n}}{(1+n)^{2n} K^{2n}} \right]^{\frac{1}{3-n}} \Phi^{\frac{1+n}{3-n}}, \quad (4.42)$$

where H_0 is a dimensionless constant that measures the deviation of the poloidal field from force-free, α^2 is a constant measuring the strength of the toroidal field with respect to the poloidal field. In non-dimensional form, using the definitions (4.12)–(4.16), these expressions are

$$\frac{dh}{d\phi} = H_0 \phi^{-\frac{1-n}{3-n}}, \quad (4.43)$$

and

$$\psi \frac{d\psi}{d\phi} = \alpha^2 \phi^{\frac{1+n}{3-n}}, \quad (4.44)$$

Eq. (4.43) and (4.44) can be integrated, obtaining

$$h(\phi) = H_0 \left(\frac{3-n}{2} \right) \phi^{\frac{2}{3-n}}, \quad (4.45)$$

and

$$\psi(\phi) = \pm \alpha \left(\frac{3-n}{2} \right)^{1/2} \phi^{\frac{2}{3-n}}, \quad (4.46)$$

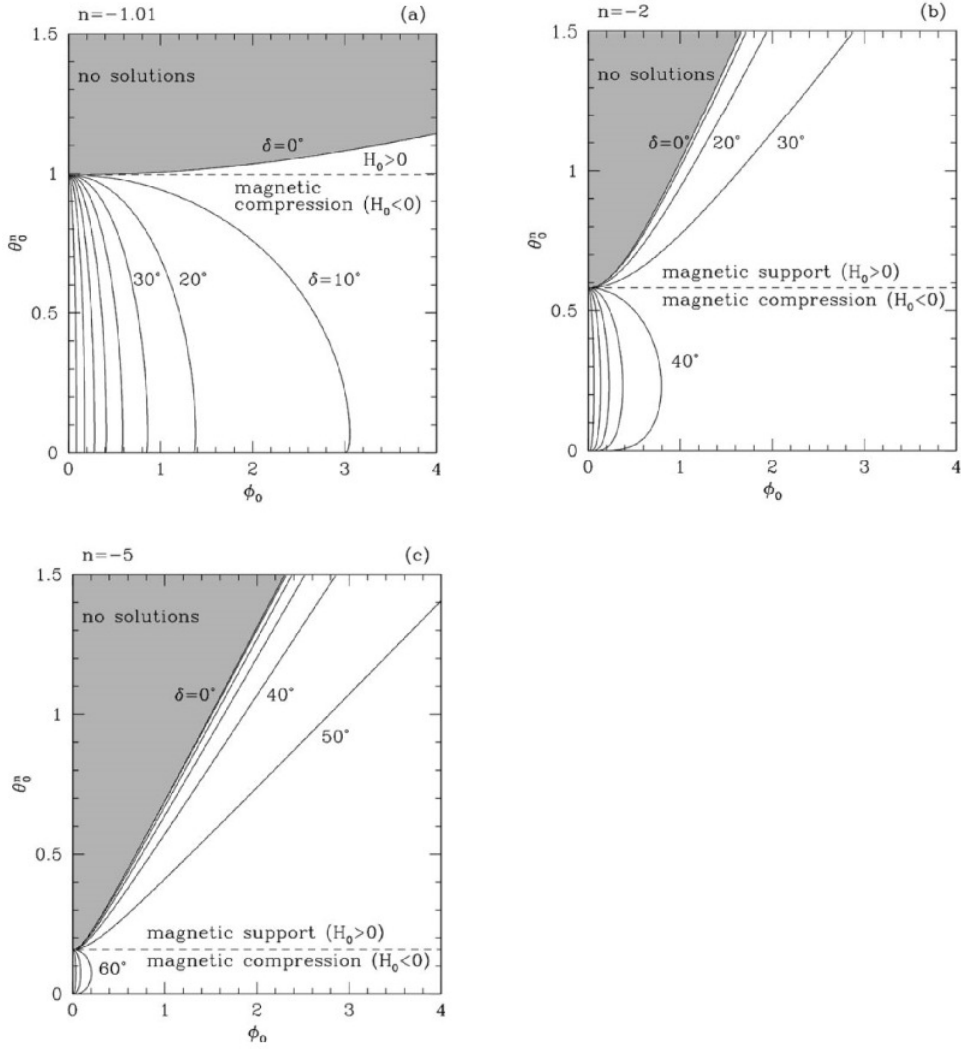


Figure 4.1: Scale-free solutions in the ϕ_0 - θ_0^n plane for $n = 1.01$ (panel *a*), $n = -2$ (panel *b*) and $n = -5$ (panel *c*). The curves are for chosen values of the pitch angle δ from 0° to 90° in steps of 10° . There are no solutions above the $\delta = 0^\circ$ curve, that represent models with a pure poloidal field. No solutions are expected in the *shaded* area above this curve. The *dashed* line is for the pitch angle δ_{ff} , when the field becomes force-free. Above this line, the magnetic field provides support to the cloud ($H_0 > 0$); below the dashed line, the magnetic field compresses the cloud ($H_0 < 0$). From Toci & Galli (2015b).

The system (4.24)–(4.25) allows power-law solutions,

$$\phi = \phi_0 \xi^{\frac{3-n}{1-n}}, \quad \theta^n = \theta_0^n \xi^{\frac{2n}{1-n}}, \quad (4.47)$$

with the scale factors $\phi_0 > 0$ and $\theta_0 > 0$ given by

$$\frac{(3-n)(1+n)}{(1-n)^2} \phi_0^{\frac{2(2-n)}{3-n}} + \alpha^2 \phi_0^{\frac{2}{3-n}} = -H_0 \theta_0^n, \quad (4.48)$$

$$H_0 \frac{2(3-n)}{(1-n)^2} \phi_0^{\frac{2}{3-n}} + \frac{4}{(1-n)^2} \theta_0 = \theta_0^n. \quad (4.49)$$

In these scale-free models, all forces (gravity, pressure gradient, and Lorentz force) decrease with radius with the same power-law slope. The Lorentz force is

$$\mathbf{F}_L = H_0 \left(\frac{3-n}{1-n} \right) \phi_0^{\frac{2}{3-n}} \xi^{\frac{1+n}{1-n}} \hat{\mathbf{e}}_{\varpi}. \quad (4.50)$$

and is directed inward for $H_0 < 0$ and outward for $H_0 > 0$. For $H_0 = 0$, the magnetic field is force-free. In this case, the density is given by the unmagnetised scale-free solution

$$\theta^n = \left[\frac{(1-n)^2}{4} \right]^{n/(1-n)} \xi^{2n/(1-n)}, \quad (4.51)$$

(see the previous Chapter), and the components of the field are

$$b_z = \phi_0 \left(\frac{3-n}{1-n} \right) \xi^{\frac{1+n}{1-n}}, \quad (4.52)$$

$$b_{\varphi} = \pm \alpha \phi_0^{\frac{2}{3-n}} \left(\frac{3-n}{2} \right)^{1/2} \xi^{\frac{1+n}{1-n}}. \quad (4.53)$$

Then, the magnetic field lines are helices twisted over cylindrical flux tubes. The magnetic field decreases with radius with a behaviour that is in between ξ^{-1} for an isothermal equation of state, and ξ^0 for a logatropic equation of state. For the values of the polytropic index derived in the previous Chapter from the fit of the radial density profiles, $-3 \lesssim n \lesssim -3/2$, the slope of the magnetic field is expected to be in the range -0.2 to -0.5 . Thus, as the discussion of Sect. 4.1 implies, for all values of $n \leq -1$ the axial field always supports the cloud and the toroidal field always compresses it. The net effect then depends on the relative strength of the two components, determined by the value of the

pitch angle δ (the angle between B_z and B_φ)

$$\tan \delta = \frac{|B_\varphi|}{|B_z|} = \frac{\alpha(1-n)}{[2(3-n)]^{1/2}} \phi_0^{-\frac{1-n}{3-n}}. \quad (4.54)$$

For small values of δ , the field is almost axial, and supports the envelope with a Lorentz force directed outward. Increasing δ the toroidal component increases, squeezing the cloud with a Lorentz force directed inward. At some particular δ_{ff} the two effects cancel out, and the field is force-free ($H_0 = 0$). This happens when

$$\alpha = \alpha_{\text{ff}} = \frac{[-(3-n)(1+n)]^{1/2}}{1-n} \phi_0^{\frac{1-n}{1+n}}, \quad (4.55)$$

as can be found from eq. (4.48) setting $H_0 = 0$. Thus, for each n , the field becomes force-free when the pitch angle is

$$\tan \delta_{\text{ff}} = \left(-\frac{1+n}{2} \right)^{1/2}, \quad (4.56)$$

a value that is related only to the polytropic index. For $n = -1$ (logatropic case) the force-free field is a poloidal field with uniform strength, while for $n \rightarrow -\infty$ (isothermal case) the force-free field is toroidal and decreases as ϖ^{-1} . For the values of n derived in the hydrostatic case, for filamentary cloud δ_{ff} varies between 26° and 45° .

Fig. 4.1 shows the loci of solutions in the ϕ_0 - θ_0^n plane (field strength vs. density in non-dimensional units), for three values of the polytropic index: $n = -1.01$ (quasi-logatropic equation of state), $n = -2$ (best-fit value for the observed filaments, see in the previous Chapter) and $n = -5$ (quasi-isothermal equation of state). Every line is a locus of solutions that has a fixed value of the pitch angle δ . The parameter space is split in two regions by the $H_0 = 0$ line of force-free configurations: for $H_0 > 0$ the Lorentz force is directed outward and supports the cloud; for $H_0 < 0$ the Lorentz force is directed inward and has the opposite effect. If $H_0 = 0$ the field is force-free, the pitch angle has the value δ_{ff} given by eq. (4.56) and the density the value obtained by eq. (4.51) independently on the field strength ϕ_0 (dashed lines in Fig. 4.1). The line $\delta = 0$ shows the locus of solutions with a purely poloidal field. This line comes from the unmagnetised solution $\theta_0^n = [(1-n)^2/4]^{n/(1-n)}$, $\phi_0 = 0$, and can be found always in the $H_0 > 0$ region of the diagram, indicating that a pure poloidal magnetic field can only support, not compress, a cloud. The solutions with $\delta = 0$ are defined by a density scale θ_0^n larger than the density scale of the unmagnetised model, due to the extra support provided by the field. No solutions are allowed above the $\delta = 0$ line.

The curves in Fig. 4.1 show that for a field strength that increases ϕ_0 , configurations with a chosen pitch angle lower than the critical value δ_{ff} support increasingly larger densities; while if the pitch angle is larger than δ_{ff} , any increase in the field strength reduces the density that can be supported. However, in the second case, equilibrium configuration only exists below a maximum value of ϕ_0 . Thus, for a fixed field strength, there is always at least one solution with density larger than the unmagnetised one, a pitch angle $\delta < \delta_{\text{ff}}$ and magnetic effects that are dominated by the poloidal component (“magnetic support”), and one (or two, or zero) solutions with density lower than the unmagnetised solution, pitch angle $\delta > \delta_{\text{ff}}$, and magnetic effects dominated by the toroidal component (“magnetic compression”). As plotted in Fig. 4.1, if the equation of state is soft (upper panel) in the parameter space “magnetic compression” solutions are more likely, whereas for a quasi-isothermal equation of state (lower panel) “magnetic support” solutions become dominant. This implies that the role of the magnetic field depends sensitively not only on the pitch angle but also on its dependence on radius via the polytropic exponent γ_p .

The two cases $n = 1.01$ and $n = -5$ in Fig. 4.1 show the behaviour of the solutions when they approach the logatropic and the isothermal limit, respectively. In the former case, solutions in which the magnetic field provides support progressively disappear. As an example, for a pitch angle δ larger than about 4° , the hoop stresses of the toroidal field dominate over the support of the dominant poloidal field, squeezing the cloud. Accordingly, the density is lower than in the case of the unmagnetised solution. Increasing $-n$, the region with $H_0 < 0$ shrinks, and the transition from support to compression occurs at larger pitch angle (about 35° for $n = -2$). For $n = -5$ the permitted parameter space is largely populated by solutions where the field gives support to the filament ($H_0 > 0$), but in the limit $n \rightarrow -\infty$ the region of no solutions covers all the ϕ_0 - θ_0^n plane. The unmagnetised solution tends to $\theta_0^n = 0$ in this limit. To be precise, even in the unmagnetised case, no scale-free solution exists for an isothermal equation of state.

4.3.3 Force between magnetised filaments

The magnetic field we used in the previous sections is generated by electric currents flowing in the filaments. A toroidal field $B_\varphi(\varpi)$, for instance, is generated by an electric current $I(\varpi)\hat{\mathbf{e}}_z$ flowing along the filament given by

$$I(\varpi) = \frac{c}{2} \int_0^{\varpi} [\nabla \times (B_\varphi \hat{\mathbf{e}}_\varphi)] \varpi \, d\varpi = \frac{c}{2} \varpi B_\varphi(\varpi). \quad (4.57)$$

For this reason, two parallel filaments, at a distance d larger than their radii ϖ_s , behave as two electric wires and exert on each other an electromagnetic force (per unit length) \mathbf{F}_{em} , repulsive if the currents are aligned, attractive if they are anti-aligned, given by

$$\mathbf{F}_{em} = \frac{2I_1 I_2}{c^2 d} \hat{\mathbf{e}}_{\varpi}. \quad (4.58)$$

This electromagnetic force scales as the gravitational force (per unit length) \mathbf{F}_g between the two filaments,

$$\mathbf{F}_g = \frac{2G\mu_1\mu_2}{d} \hat{\mathbf{e}}_{\varpi}, \quad (4.59)$$

where μ is the mass per unit length. Therefore their ratio is independent on the filaments separation

$$\mathcal{R} \equiv \frac{|\mathbf{F}_{em}|}{|\mathbf{F}_g|} = \frac{I_1 I_2}{c^2 G \mu_1 \mu_2} \sim \left(\frac{I}{c G^{1/2} \mu} \right)^2. \quad (4.60)$$

In this last approximation we assume that the two filaments have similar properties. Following eq. (4.57), the electric current is zero on the axis and equal to $c\varpi_s B_{\varphi,s}/2$ on the surface (in the scale-free models we developed for the filaments' envelopes, in which ϖB_{φ} increases outwards, the electric current is maximum at the surface). Taking the average, we can set $I \approx c\varpi_s B_{\varphi,s}/4$, to have

$$\mathcal{R} \approx \frac{1}{16} \left(\frac{\varpi_s B_{\varphi,s}}{G^{1/2} \mu} \right)^2. \quad (4.61)$$

substituting numerical values,

$$\mathcal{R} \approx 22 \left(\frac{\varpi_s}{1 pc} \right)^2 \left(\frac{B_{\varphi,s}}{10 \mu G} \right)^2 \left(\frac{\mu}{10 M_{\odot} pc^{-1}} \right)^{-2}. \quad (4.62)$$

This picture is extremely idealised, and also have a large uncertainty on the results because is difficult to estimate the filament's outer radius ϖ_s and the related value of the (toroidal) magnetic field. However, the non-negligible numerical value of \mathcal{R} implies that the electromagnetic forces may play a role as important as gravity in the interaction between magnetised filaments.

4.4 Summary

Magnetic field seems to play an important role in determining the observable properties of filamentary clouds. In this Chapter we analysed the properties of magnetised polytropes in cylindrical geometry, extending the study we made in Chapter 3.

The main hypothesis is that the evolution of real filaments can be approximated as a series of magnetostatic solutions as filaments accrete more material from the surrounding environment, thus the models we developed are magnetostatic by design. However, this does not necessarily imply zero a velocity field everywhere, if the accretion speed becomes either subsonic or directed mostly parallel to the filament's axis in the central parts of the filament. We solved general equations for magnetised filamentary clouds imposing a polytropic equation of state, and assuming cylindrical symmetry together with magnetostatic equilibrium. We formulated the problem in terms of two partial differential equations for four unknowns: the density ρ , the flux function Φ for the poloidal field, and two functions of Φ , namely the enthalpy $H(\Phi)$ and the toroidal field function $\Psi(\Phi)$. Generally, to obtain solutions additional assumptions are needed, because the previous evolution of the system is not known. In the literature, these additional assumptions imply specific choices of the dependence of the two component of the field on density and/or radius (e.g. Fiege & Pudritz 2000). In this work, we did not adopt these assumptions. In fact, we analysed the properties of the models in the region near the axis (the filament's core) where the boundary conditions given by symmetry requirements determine the behaviour of the solutions, and at large radii, where the solutions are expected to reach a scale-free form for $n \leq 1$.

The of equation of state explored in this work range from a “logatropic” ($n = -1$, or $\gamma_p = 0$) to an “isothermal” ($n \rightarrow -\infty$, or $\gamma_p = 1$). In all these cases, variables have a power-law behaviour with profiles that become flatter as the equation of state becomes softer. As the polytropic exponent γ_p decreases from 1 to 0, the power-law exponents range from -2 to -1 for the density and from -1 to 0 for the magnetic field.

According to the power-law slope, the magnetic field affects the radial density profile of the cloud in opposite ways. In the range $n \leq -1$, the magnetic field can either support or compress the cloud (or be force-free) depending on the relative strength of the toroidal and poloidal components. Pure poloidal fields, or with small toroidal components (small pitch angle δ) give support to the cloud ($H_0 > 0$). This allows higher values of the envelope density θ_0^n than those resulting from thermal support alone. While the strength of the toroidal component increases ($\alpha^2 > 0$), the effect of the field becomes very sensitive to the field strength ϕ_0 : a small change in ϕ_0 changes the sign of the Lorentz force, from

supporting to squeezing the cloud. In the latter case, the density of the envelope is lower than the expected value in a non magnetised filament. For softer equation of state, the confining effect of the field is enhanced because the poloidal component becomes more uniform. In particular, for a logatropic equation of states, all scale-free solutions have a Lorentz force directed inward, and their density is lower than in the non magnetic case. Conversely, all scale-free solutions converge to zero density in the limit of an isothermal equation of state, because, as shown in Chapter 3, the typical asymptotic power-law behaviour of an isothermal cylinder is reached only at infinite radius, where the density is zero.

Within the limits of the idealised scale-free models for magnetised filaments presented in Chapter 4, our results seems to point out that a measure of the pitch angle of the magnetic field associated to filaments can give a way to discriminate filaments that are compressed by the field from those that are supported by the magnetic field itself. High-resolution observations of polarised dust emission inside the filaments (e.g. with ALMA) will be very useful to understand the role of large- and small-scale magnetic fields in their formation and evolution.

The magnetisation of interstellar filaments implies also the presence of electric currents flowing along and/or around them, producing attractive (or repulsive) electromagnetic forces that enhance (or dilute) their gravitational field and may affect their interactions.

5

Theoretical and numerical modelling of MHD collapse

As shown in the previous Chapters, the magnetic field influences the stability and the evolution of molecular clouds. However, turbulence is also an important ingredient due to the fact that it can provide a non-thermal pressure contribution. In the literature, as already reported in the Introduction, turbulence has been studied in great details with numerical simulations. Almost all these numerical studies are concerned with gas in static volumes. During the process of star formation, however, a cloud undergoes expansions and contractions (induced by gravitational or pressure effects), and therefore its volume changes in time.

Little work has been done to characterise the evolution of turbulent motions physics in expanding or contracting gases in this field. In a recent study, Robertson & Goldreich (2012) simulated the behaviour of isotropic hydrodynamic turbulence during an isotropic contraction, finding an *adiabatic heating* mechanism capable to amplify turbulence by compression in cases where the contraction is more efficient than the dissipation of the random bulk energies. It should be noted, however, that Davidovits & Fisch (2017) found a lower bound for this enhancement of fluctuations, suggesting that some numerical models could be too much dissipative.

Related problems are the evolution of the observed oscillations in cores that are undergoing a contraction (Keto & Caselli 2010), and the *inverse Hubble flow* model developed by Toalá et al. (2015), studying the problem of the growth of density perturbations during the gravitational collapse of a spherical pressureless cloud in analogy with the cosmological model of the expanding Universe. For all these reasons, it is interesting to study the temporal evolution of a magnetised and turbulent element of fluid in a contracting cloud.

In order to study homogeneous turbulence taking into account the effect of contraction, it is more convenient, from a numerical point of view, to use a local simulation

box in Cartesian-like coordinates and periodic boundary conditions. Within such settings the physical processes under investigation can be more easily modelled employing high-accuracy numerical methods. The expanding box model (EBM) (Grappin et al. 1993) allows to study the evolution of compressible MHD turbulence in expanding/contracting volumes in Cartesian coordinates (see also Grappin et al. (1991) and Grappin & Velli (1996)), due to the fact that the effect of expansion/contraction is taken into account by a stretching local frame comoving with the mean velocity. This scheme was originally devised to study turbulence in the expanding solar wind. The model is based on a separation of scales, a large scale characteristic of the mean flow and a small scale describing turbulent fluctuations. The feedback of turbulent fluctuations on the mean flow is neglected.

If the mean flow is radially symmetric it cannot be eliminated by a Galilean transformation. In fact, when following a plasma volume transported by the wind, the effect of the radial flow is equivalent to external forces stretching the volume in directions perpendicular to the radial direction. It is then convenient to use a domain that is expanding at a constant rate in these directions so that the volume stretching reduces to a time-dependent rescaling of transverse gradients and the external forces become, to first order, additional time-dependent linear terms in the original MHD equations. EBM equations do not conserve quadratic invariants, like the energy, due to the external forces that cause the stretching, but linear invariants as angular momentum and magnetic flux are conserved. In a more general context, expansion or contraction can be prescribed by assigning a metric tensor. It is thus convenient to write the equations of the EBM in a covariant formalism more appropriate for multi-purpose conservative schemes working in any system of coordinates. The ECHO code equations are written in this form. In the following Section we will briefly describe how to obtain the EBM equations and the equivalent metric in the covariant formalism.

5.1 The expanding box model for the solar wind

Consider a parcel of plasma at initial position \mathbf{R}_0 , travelling a constant speed \mathbf{u} , so that its position at any time is $\mathbf{R}(t) = \mathbf{R}_0 + \mathbf{u}t$. It is convenient to introduce the *expansion scale factor*,

$$a(t) = \frac{R(t)}{R_0}, \quad \dot{a} = \frac{u(R)}{R} \quad (5.1)$$

where $R_0 = R(t = 0)$ is the initial parcel position and the dot indicates time derivation. The quantity \dot{a}/a in (5.1) is the inverse of the expansion characteristic time, the analogous of the Hubble time in cosmology. MHD equations may be integrated within $|\phi| \leq \alpha$, $|\theta| \leq$

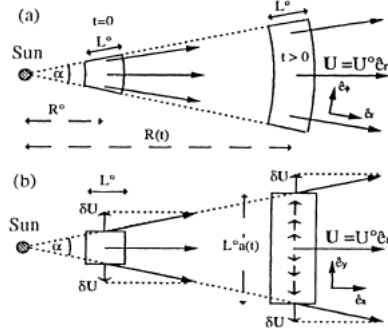


Figure 5.1: Original figure of the evolution of a plasma volume that flows in a spherical wind with constant speed (Grappin et al. 1993). In fig. (a) is showed the exact evolution, in fig. (b) the approximate evolution in the limit of small angular size α

$\pi/2 - \alpha$, where α is the angular size of the box. If the box is small enough, $\alpha \ll 1$ and $L^0 \ll R(t)$, where L^0 is the dimension of the box. We now choose a locally Cartesian-like coordinate system with $x = r - R(t)$ and *stretched* transverse coordinates y and z , expanding at the rate $a(t)$ due to the radial diverging flow. Provided the box is taken sufficiently small such that the expansion/contraction speed inside the box can be considered uniform, after a Galilean transformation in the new *comoving* frame $x^1 = x, x^2 = y/a, x^3 = z/a$ the residual velocity is, to the first order,

$$\mathbf{u}_0 = \dot{a}(0, x^2, x^3) = \frac{\dot{a}}{a}(0, y, z) \quad (5.2)$$

which is not vanishing in the transverse direction. In the evolution equations, time derivatives and transverse spatial gradients are different. They become:

$$\partial_t \rightarrow \partial_t - (\mathbf{u}_0 \cdot \nabla), \quad \nabla = \left(\partial_1, \frac{1}{a} \partial_2, \frac{1}{a} \partial_3 \right) = (\partial_x, \partial_y, \partial_z) \quad (5.3)$$

and new source terms as eq. (5.2) appear in MHD equations (see Grappin et al. 1993 or Grappin & Velli 1996, Grappin et al. 1991, Tenerani & Velli 2013). The EBM transformation (comoving plus expanding domain) is equivalent to introducing a change of coordinates $\mathbf{x}'(\mathbf{x}, t)$:

$$\mathbf{x}'(\mathbf{x}, t) = \mathbb{M}(t) \cdot \mathbf{x}, \quad (5.4)$$

where $\mathbb{M}(t) = \text{diag}(1, 1/a, 1/a)$. The metric formalism allows us to generalise the EBM equations to non-constant speed of expansion/contraction that is required to describe free-fall motion of gas toward the center of molecular clouds or the homologous collapse of

an interstellar cloud¹. It also allows to choose different cases of expansion/contraction, like the contraction along one axis or a more general anisotropic contraction, that can be useful to represent the collapse of a molecular cloud filament or core. The isotropic case $\mathbb{M}(t) = \text{diag}(1/a, 1/a, 1/a)$ corresponds to the expanding Universe or the *inverse Hubble flow*.

5.2 Contracting box model

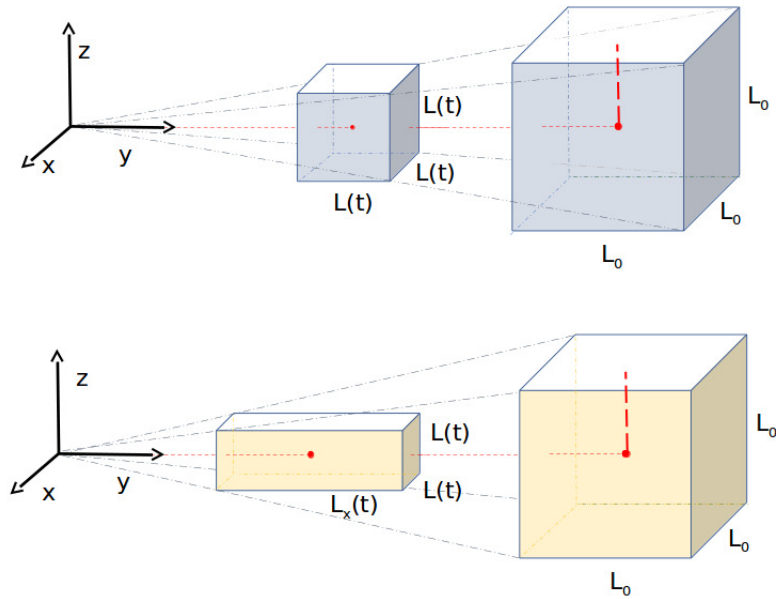


Figure 5.2: Homogeneous (blue box) and free-fall (orange box) contraction.

We generalised the formalism of EBM for a generic anisotropic metric stretched in all the directions. The ECHO code simulates the effect of the background gravity with the comoving coordinates. The metric of the contraction is induced by the self-gravity of external background, that forces the cloud contract, and is superimposed and fixed as an external parameter of the problem.

¹In the case of the solar wind, the accelerated case has been studied by Tenerani & Velli (2013).

Different is the case in which the focus is on the growth of small perturbation in a fluid. In that case the self-gravity of each fluid element can become important (if the Jeans length related to the element becomes comparable or larger than its size). The ECHO code does not take into account self-gravity, but in Chapter 6 we will give an analytical estimate of its effect in the hydrodynamical case.

Let us now choose again a locally Cartesian-like coordinate system, and assume that the velocity field is given by the overall contraction/expansion with velocity $\mathbf{u}_0(\mathbf{x}, t)$ plus a residual component $\mathbf{u}(\mathbf{x}, t)$. Provided the box is taken sufficiently small such that the speed can be considered as uniform, the former can be removed with a Galilean transformation. In analogy with the EBM model, the contraction/expansion velocity is given by

$$\mathbf{u}_0(\mathbf{x}, t) = \left(\frac{\dot{a}}{a}x, \frac{\dot{b}}{b}y, \frac{\dot{c}}{c}z \right) \equiv \mathbb{H}(t) \cdot \mathbf{x}, \quad (5.5)$$

where $\mathbb{H}(t) = \text{diag}(\dot{a}/a, \dot{b}/b, \dot{c}/c)$. The terms containing $\mathbf{u}_0 \cdot \nabla$ can be eliminated by introducing comoving coordinates $\mathbf{x}'(\mathbf{x}, t)$:

$$\mathbf{x}'(\mathbf{x}, t) = \mathbb{M}(t) \cdot \mathbf{x}, \quad (5.6)$$

where $\mathbb{M}(t) = \text{diag}(1/a, 1/b, 1/c)$. Notice that

$$\frac{\partial \mathbb{M}}{\partial t} = -\mathbb{M} \cdot \mathbb{H}. \quad (5.7)$$

The transformation of time and space derivatives is

$$\frac{\partial}{\partial t} = \frac{\partial}{\partial t} + \frac{\partial \mathbf{x}'}{\partial t} \cdot \nabla' = \frac{\partial}{\partial t} - \mathbf{u}_0 \cdot \nabla, \quad (5.8)$$

and

$$\nabla = \mathbb{M} \cdot \nabla', \quad (5.9)$$

where we have used

$$\frac{\partial \mathbf{x}'}{\partial t} = \frac{\partial \mathbb{M}}{\partial t} \cdot \mathbf{x} = -\mathbb{M} \cdot \mathbb{H} \cdot \mathbf{x} = -\mathbb{M} \cdot \mathbf{u}_0. \quad (5.10)$$

In this coordinate system the standard ideal MHD equations (see Section 2.1) become

$$\frac{\partial \rho}{\partial t} + \mathbb{M} \cdot \nabla' \cdot (\rho \mathbf{u}) = -\rho \text{tr} \mathbb{H}, \quad (5.11)$$

$$\frac{\partial \mathbf{u}}{\partial t} + (\mathbf{u} \cdot \mathbb{M} \cdot \nabla') \mathbf{u} + \frac{1}{\rho} \mathbb{M} \cdot \nabla' \left(P + \frac{B^2}{2} \right) + \frac{\mathbf{B}}{4\pi\rho} \times (\mathbb{M} \cdot \nabla' \times \mathbf{B}) = -\mathbb{H} \cdot \mathbf{u}, \quad (5.12)$$

$$\frac{\partial P}{\partial t} + (\mathbf{u} \cdot \mathbb{M} \cdot \nabla')P + \gamma P \mathbb{M} \cdot \nabla' \cdot \mathbf{u}' = -\gamma P \text{tr}\mathbb{H}, \quad (5.13)$$

and

$$\frac{\partial \mathbf{B}}{\partial t} + \mathbb{M} \cdot \nabla' \times (\mathbf{B} \times \mathbf{u}) = \mathbf{B} \cdot (\mathbb{H} - \mathbb{I} \text{tr}\mathbb{H}), \quad (5.14)$$

Note that we added in the momentum equation $-\rho \mathbb{W} \cdot \mathbf{x}$, the force per unit volume responsible for the acceleration of the contraction.

Assume now that the physical quantities are given by the overall mean value plus a fluctuating component,

$$\rho(\mathbf{x}, t) = \rho_0(t) + \rho_1(\mathbf{x}, t), \quad P = P_0(t) + P_1(\mathbf{x}, t), \quad \mathbf{B} = \mathbf{b}_0(\mathbf{x}, t) + \mathbf{B}_1(\mathbf{x}, t), \quad (5.15)$$

where $\rho_0(t)$, $P_0(t)$ and $\mathbf{B}_0(t) = B_0 \hat{\mathbf{e}}_z$ are uniform.

Substituting these expansions in the MHD equations we obtain the MHD equations for the background quantities

$$\frac{\partial \rho_0}{\partial t} = -\rho_0 \nabla \cdot \mathbf{u}_0 = -\rho_0 \text{tr}\mathbb{H}, \quad (5.16)$$

$$\frac{\partial \mathbf{u}_0}{\partial t} + (\mathbf{u}_0 \cdot \nabla) \mathbf{u}_0 - \mathbb{W} \cdot \mathbf{x} = 0, \quad (5.17)$$

$$\frac{\partial P_0}{\partial t} = -\gamma P_0 \nabla \cdot \mathbf{u}_0 = -\gamma P_0 \text{tr}\mathbb{H}, \quad (5.18)$$

$$\frac{\partial B_0}{\partial t} = -\nabla \times (\mathbf{B}_0 \times \mathbf{u}_0) = -B_0 \left(\frac{\dot{a}}{a} + \frac{\dot{b}}{b} \right). \quad (5.19)$$

The solutions of the equation of continuity, pressure and induction are

$$\rho_0(t) = \frac{C_1}{abc}, \quad (5.20)$$

$$P_0(t) = \frac{C_2}{(abc)^\gamma} \quad (5.21)$$

and

$$B_0(t) = \frac{C_3}{ab}, \quad (5.22)$$

where C_1 , C_2 and C_3 are constants, while the momentum equation is correct if the box is sufficiently small compared to the scale in which the mean velocity \mathbf{u}_0 varies.

In this coordinate system the linearized MHD equations for the fluctuations become

$$\frac{\partial \rho_1}{\partial t} + \rho_0 \mathbb{M} \cdot \nabla' \cdot \mathbf{u}_1 = -\rho_1 \text{tr} \mathbb{H}, \quad (5.23)$$

$$\frac{\partial \mathbf{u}_1}{\partial t} + \frac{c_s^2}{\rho_0} \mathbb{M} \cdot \nabla' \rho_1 + \frac{\mathbf{B}_0}{4\pi\rho_0} \times (\mathbb{M} \cdot \nabla' \times \mathbf{B}_1) = -\mathbb{H} \cdot \mathbf{u}_1, \quad (5.24)$$

$$\frac{\partial P_1}{\partial t} + \gamma P_0 \mathbb{M} \cdot \nabla' \cdot \mathbf{u}'_1 = -\gamma P_1 \text{tr} \mathbb{H}, \quad (5.25)$$

and

$$\frac{\partial \mathbf{B}_1}{\partial t} + \mathbb{M} \cdot \nabla' \times (\mathbf{B}_0 \times \mathbf{u}_1) = \mathbf{B}_1 \cdot (\mathbb{H} - \mathbb{I} \text{tr} \mathbb{H}), \quad (5.26)$$

where the terms on the right side of the equations arise from the compression of the fluid element due to the mean flow. Classic EBM model can be obtained setting $a \rightarrow 1$ and $b = c$, the free-fall with $b = c$, and Hubble-like case with $a = b = c$.

5.3 The ECHO Code

Our goal is to study the evolution of turbulence in a molecular cloud that is contracting following a generic metric both in analytical and numerical way. In order to perform numerical simulations we used the ECHO code, that solves numerically the 3D MHD system of equations, based on an *Eulerian conservative high-order* scheme (see i.e Londrillo & Del Zanna 2000, Londrillo & del Zanna 2004, Del Zanna et al. 2007, Landi et al. 2008). For a short description of the code see Appendix A.2.

When the aim of a simulation is to study not only shocks or discontinuities, but also small-scale structures, like turbulent flows and waves, high numerical accuracy in conservative schemes is required. In fact, if the numerical diffusion of the scheme is too high, these structures tend to be smeared out. However, higher than second order accuracy is needed also because, for 3D simulations, numerical grids are limited in size.

High-order numerical methods have been implemented in ECHO to solve MHD equations by Londrillo & Del Zanna (2000), where the request for the magnetic field to be solenoidal was used as a built-in condition (*upwind constrained transport* method, UCT, see Appendix A.4). In general ECHO allows to solve different sets of equations (from classic to general relativistic MHD) and includes different algorithm in a single framework. ECHO is written in Fortran90, composed by modules and parallelised with MPI directives. In particular the code implies a finite difference discretisation, high order component-wise reconstruction methods, a two-wave approximate Riemann solver, and

multi-stage Runge-Kutta for time integration (See A.2 in the Appendix). Different boundary conditions are implemented in the code (See A.2 in the Appendix). In this thesis we used periodic boundary conditions.

5.3.1 Conservative form of MHD equations and code implementations

The standard ECHO code solves *ideal* classical and relativistic MHD equations in the general, conservative form (Del Zanna et al. 2015)

$$\partial_t \mathcal{U} + \partial_i \mathcal{F}^i = \mathcal{S}, \quad (5.27)$$

where \mathcal{U} is a generic vector of conservative variables, \mathcal{F}^i are the corresponding fluxes (i is the index of the 3 spatial coordinates x^i and is assumed the Einstein convention of sum over repeated indexes) and \mathcal{S} is the vector that contains the source terms. Using a generic metric tensor g_{ij} , with determinant g , the MHD system in a conservative form is

$$\mathcal{U} = \sqrt{g} \begin{pmatrix} \rho \\ \rho v_j \\ E_t \\ B^j \end{pmatrix}, \quad \mathcal{F}^i = \sqrt{g} \begin{pmatrix} \rho v^i \\ \rho v^i v_j - B^i B_j + p_t \delta_j^i \\ (E_t + p_t) v^i - (v_k B^k) B^i \\ v^i B^j - v^j B^i \end{pmatrix} \quad (5.28)$$

where the *total* kinetic plus magnetic pressure and energy are:

$$p_t = p + \frac{1}{2} B^2, \quad E_t = \frac{1}{2} \rho v^2 + \frac{1}{\gamma - 1} p + \frac{1}{2} B^2. \quad (5.29)$$

The source terms needed are

$$\mathcal{S} = \sqrt{g} \begin{pmatrix} 0 \\ \frac{1}{2} (\rho v^i v^k - B^i B^k + p_t g^{ik}) \partial_j g_{ik} \\ -\frac{1}{2} (\rho v^i v^j - B^i B^j + p_t g^{ij}) \partial_t g_{ij} \\ 0 \end{pmatrix}. \quad (5.30)$$

We must remember that covariant and contravariant components are related by $v_i = g_{ij} v^j$. In fact, starting from MHD equation in a conservative form in contravariant formalism, covariant form of MHD equation can be obtained using the latter equation. As an example, let's introduce the EBM model within such framework. Given the scale factor

$a = a(t)$ of (5.1), the metric tensor must be defined as

$$g_{ij} = \text{diag}[1, a^2(t), a^2(t)], \quad \sqrt{g} = a^2(t) \quad (5.31)$$

which is almost Cartesian (diagonal and spatially uniform), but time-dependent. If we want to use usual Cartesian orthonormal coordinates we find that $v^1 = v_1 = v_x, v_2 = a^2 v^2 = a v_y, v_3 = a^2 v^3 = a v_z$. Thus, starting from the contravariant formalism we obtain the covariant form of continuity equation:

$$\partial_t(a^2 \rho) + \partial_i(a^2 \rho v^i) = 0, \quad (5.32)$$

thus if $i = 1$ then $v^1 = v_1 = v_x$, either if $i = 2$ or $i = 3$ then $v_2 = a^2 v^2 = a v_y$ and $v_3 = a^2 v^3 = a v_z$.

$$\partial_t \rho + 2 \frac{\dot{a}}{a} \rho + \partial_x(\rho v^x) + a \partial_y(\rho \frac{v^y}{a}) + a \partial_z(\rho \frac{v^z}{a}) = \partial_t \rho + 2 \frac{\dot{a}}{a} \rho + \partial_x(\rho v_x) + \partial_y(\rho v_y) + \partial_z(\rho v_z) = 0 \quad (5.33)$$

Then we obtain again

$$\frac{\partial \rho}{\partial t} + \nabla \cdot (\rho \mathbf{v}) = -2 \frac{\dot{a}}{a} \rho. \quad (5.34)$$

With the same considerations we can obtain also the other equations.

Note that if we assume that our metric is only time dependent the source term proportional to $\partial_j g_{ik}$ vanishes while $\partial_t g_{ik}$ is different from zero, and in particular the term into the energy equation is

$$-\frac{1}{2}(\rho v^i v^j - B^i B^j + p_t g^{ij}) d_t g_{ij} = -\frac{\dot{a}}{a}(\rho v_\perp^2 - B_\perp^2 + 2p_t) \quad (5.35)$$

where $v_\perp = v_y^2 + v_z^2$ and similarly for the magnetic field.

Implementation to the standard ECHO code

We have generalised the ECHO code, allowing the use of a generic diagonal metric. The related contraction/expansion can be also accelerated (in the regime in which the model can be applied). The source contribution in the energy equation eq. (5.35) becomes

$$-\frac{1}{2}(\rho v^i v^j - B^i B^j + p_t g^{ij}) d_t g_{ij} = -\sum_j \frac{g_{jj}}{g_{jj}}(\rho v_j^2 - B_j^2 + p_t), \quad (5.36)$$

that for an inverse Hubble flow is

$$-\frac{1}{2}(\rho v^i v^j - B^i B^j + p_t g^{ij})d_t g_{ij} = -\frac{\dot{a}}{a}(\rho v^2 - B^2 + 3p_t). \quad (5.37)$$

Since the ECHO code solves the EBM equations with a conservative numerical scheme, viscosity and resistivity are ignored and we need to introduce them explicitly so as to be able to control the conversion of turbulent motions into internal energy. We thus introduced explicitly the viscosity and resistivity and tested the code by checking the known time-scale associated to the steepening of a sound wave into a shock in the static case. We then studied the contracting and expanding EBM and Hubble-like cases, to understand how the characteristic time of shock formation changes when the rate of contraction/expansion is varied.

In the Navier-Stokes and in the Ohm equations and eq. (2.9) eq. (2.13) explicit contributes related to the divergence of the Laplacian terms arises. In particular, the flux of the viscosity stress tensor gives

$$F_i = \Sigma_j \zeta v_i \left(\frac{\partial v_i}{\partial x_j} + \frac{\partial v_j}{\partial x_i} - \frac{\partial v_l}{\partial x_l} \delta_{i,j} \right) = \zeta \Sigma_j v_j \frac{\partial v_j}{\partial x_i}, \quad (5.38)$$

and similarly for the resistive term into the Ohm equation (Landi et al. 2008).

Tests

We would like to test the ECHO code with a simple, known case: the sinusoidal 1D sound wave. The governing equations are the continuity equation and the Navier-Stokes equation (see Section 2.1), and, in the absence of dissipation, the exact solution for a monochromatic wave with k_0 wave vector is

$$u_1 = \hat{u}_1 \exp(ik_0 x - i\omega t) \quad (5.39)$$

with dispersion relation $\omega^2 = c_s^2 k_0^2$. Including the effect of the viscosity ($\zeta \neq 0$), the last equation becomes $\omega^2 = c_s^2 k_0^2 - i\zeta \omega k_0^2$. The frequency is in general complex, we can then write $\omega_c = -\frac{1}{2}\zeta k_0^2$ and $\omega_r^2 = c_s^2 k_0^2 - \frac{1}{4}\zeta^2 k_0^4$. Thus the monochromatic wave is

$$u_1 = \hat{u}_1 \exp(ikx - i\omega_r t) \exp(-1/2\zeta k^2 t) \quad (5.40)$$

and as $\omega_i < 0$, this wave is decaying in time $\sim \exp(\omega_c t)$. In presence of viscosity a sound wave is then damped, in particular waves with large wave numbers k , i.e. small wavelengths are dissipated faster ($\omega_c k^2$ is larger). We then expect in the linear regime a

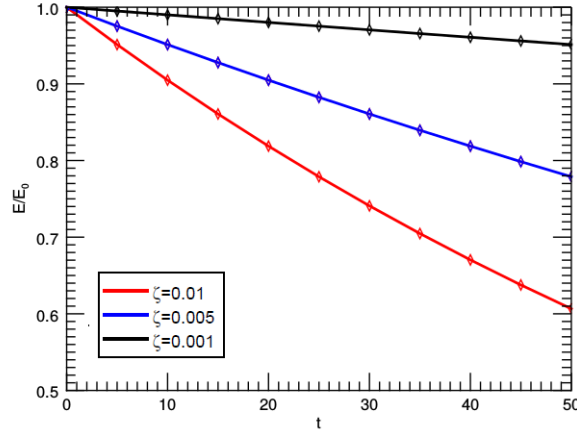


Figure 5.3: Effects of explicit viscosity during the propagation of sound waves in the linear regime: the wave is damped and the kinetic energy exponentially decrease. The initial condition is a monochromatic sound wave propagating along the x axis with $k_0 = 1$, $\gamma = 5/3$ and a value for the velocity fluctuation of 0.1 in the code units. The domain is periodic and the initial crossing time is 1 in code units. The numerical simulations and the theoretical expectations from eq. (5.41) are in good agreement.

behaviour of the kinetic energy

$$E_k \sim |u_{1,k_0}^2| \exp(-\zeta k_0^2 t). \quad (5.41)$$

In Fig. (5.3) is shown the good agreement between the simulations and the theoretical results.

The effects of viscosity are also shown in Fig. (5.4). This figure shows the evolution of a plane sound wave with an initial mode k_0 in an ideal HD case and in a viscous HD case. Due to nonlinear effects the profile of the wave steepens as it propagates, forming a shock. An intuitive way to explain the steepening is that the peak of the wave (with higher velocity) catches the trough of the wave (with lower velocity) as an effect of the advection term in momentum equation. The steepening time is then given by the distance between the two parts ($l \sim 1/k_0$) divided by the velocity u , that is the *nonlinear time*, $t^* \sim 1/k_0 u$. As Fig. (5.4) shows, if the main interest of the physical case under consideration are shocks, there is no need for implementing the viscosity and resistivity effects. In fact, the position of the shocks is well captured in both cases, and does not depend on dissipative effects. The introduction of explicit viscous and resistive terms is crucial in order to stabilise the

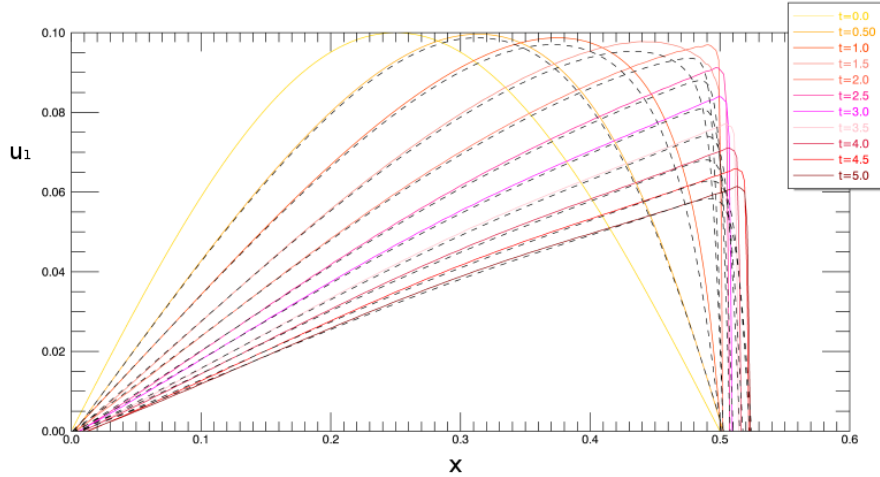


Figure 5.4: A comparison between velocity fluctuations in ideal MHD (coloured) and viscous MHD (dashed lines) at the same times. The initial condition is a monochromatic sound wave propagating along the x axis with $k_0 = 1$, $\gamma = 5/3$ and a value for the velocity fluctuation of 0.1 in the code units. The resolution implied is $n = 512$ grid points and the value of the viscosity $\zeta = 5 \times 10^{-4}$. The domain is periodic and the initial crossing time is 1 in code units. The wave propagates and forms a shock at the time $t^* \sim 1/k_0 u_1$, in this case ~ 1.6 in normalised time t . Introducing viscosity in the code the amplitude of the wave is damped due to dissipation. The ECHO code is shock-capturing, thus the shock forms at the same time and in the same position in both the ideal and the viscous case. As a consequence, the front waves velocity increases.

code in simulations where the focus is on turbulence and vortexes circulation, allowing energy to be dissipated at the small scales. This prevent the accumulation of energy at small scales.

After the generalisation of the metric in the code we tested the consistency of the simulations. The prototype case we studied is a Hubble-like MHD contraction ($a = b = c = 1 - t/t_c$) with constant value for the thermodynamical quantities and $t_c = 1$ in the code units (see Section 6.5 for the code normalisation in the HD case). Values for unperturbed quantities are: $\rho_0 = 1$, $v_{x,0} = 1$, $B_{y,0} = 1$ in the normalised code units, $\gamma = 1$. Using equations (5.16), (5.18) and (5.19) in the linear phase we expected that $\rho_0 \sim a^{-3}$, $v_{x,0} \sim a^{-1}$, $P_0 \sim a^{-3\gamma}$, $B_{y,0} \sim a^{-2}$.

6

Hydrodynamics in contracting volumes

As a first analysis, due to the complexity of the MHD problem, we simplify the MHD equations in contracting volumes of Sect. 5.2, studying first a non-magnetic contraction (thus, in all this Chapter, $\mathbf{B} = 0$).

To address the problem of sub-structure formation in cloud cores, we investigate the evolution of density and velocity perturbations embedded in a contracting medium (the “background”, or “parent cloud”) undergoing isotropic or anisotropic collapse. We use the theoretical framework we developed to study contracting flows, that allows us to follow analytically the linear and nonlinear evolution of perturbations in the two simple cases of contracting backgrounds we introduced: a spherical cloud undergoing homologous pressureless collapse, and the spherical accretion flow on a point mass¹.

We formulate the equations of hydrodynamics in comoving coordinates. Our goal is to apply the study of the dynamics of hydrodynamical waves to contracting interstellar clouds, analytically analysing the evolution of linear perturbations in anisotropic and isotropic contractions. Thus, we investigate the homologous collapse of a cloud with uniform density and the spherical accretion flow on a point mass, comparing our analytical results to hydrodynamical simulations in contracting box performed on the CINECA supercluster MARCONI. We also evaluated analytically the *non-linear time* t_{NL} , when the linear approximation breaks up and the perturbations enter into the non-linear stage. To estimate this time we adopt the Burger’s equation already introduced in Sec. 2.29, using comoving coordinates. We verify numerically that our estimate corresponds to the beginning of the non-linear dissipation of kinetic energy’s phase. Finally, we apply our results to an astrophysical case: the growth of small-scale density perturbations during the col-

¹See Appendix for details of the calculations.

lapse of molecular cores. This process is important because it is related to the theory of molecular cloud's fragmentation.

6.1 Sub-structure formation in starless cores

The growth of small-scale density perturbations during the collapse of an interstellar cloud has been studied by many authors trying to understand the formation of stellar clusters and multiple stellar system by the process of fragmentation.

The concept of fragmentation is the breakup of large, self-gravitating clouds into smaller sub-unities (clumps, cores and stellar clusters). The earliest study in this field has been made by [Hoyle \(1953\)](#), and at that time the works were focused on the growth of initially Jeans-unstable perturbations. [Tohline \(1980\)](#) introduced the concept of “delayed fragmentation”, because the beginning of gravitational instability can occur only after the mean density of the cloud (that is assumed to be in free-fall collapse) has grown significantly, and the instantaneous value of the Jeans length has become smaller than the scale of the perturbed region. He proposed that in this case the time that a perturbation needs for a significant amplification of its amplitude would be larger than the time the parent cloud has left in its evolution, and then proposed a converging motion of the gas in alternative to self-gravity, as a way to amplify small-scale density perturbations which are initially Jeans-stable.

The fate of these initially Jeans-stable perturbations was investigated numerically in collapse simulations made by [Rozyczka \(1983\)](#), who found that the latter are efficiently damped well before reaching the threshold for gravitational instability. Thus, they are unable to form well-defined fragments. Furthermore, in those simulations has been found the formation of local concentrations of angular momentum (possibly as the result of tidal interactions) even in the collapse of clouds with no initial rotation.

The model described in this Chapter can be applied to molecular cloud cores containing only a few Jeans masses. We focus then on the evolution of Jeans-stable density perturbations, that initially oscillate as a collection of sound waves of small amplitude. This is justified by the observational result that non-thermal motions in dense cores are generally subsonic ([Myers & Benson 1983](#)). In the case of starless cores, it has been suggested that subsonic motions (“turbulence”) may be forming the seeds of multiple sites of star formation ([Goodwin et al. 2004](#)), but scarce evidence has been found yet for sub-structure formation in these objects (see i.e [Dunham et al. 2016](#)). Only recently some evidence of compact substructure has been found in one starless core in Ophiuchus ([Kirk et al. 2017](#)) and in the Orion Molecular Cloud 1 South ([Palau et al. 2017](#)). However, the

processes determining the formation of multiple protostellar seeds at these scales remain unclear.

The analysis we made in this Chapter can be considered a generalisation of the original approach to this problem made by Toalá et al. (2015), who formulated the problem in the framework of an *inverse Hubble flow*, i.e. the gravitational collapse of a spherical pressureless clouds². They found that the gravitational instability occurs faster in inverse Hubble flows than in a static cloud, and postulated that growing, unstable perturbations on scales larger than the Jeans length λ_J collapse when they reach the non-linear stage, i.e. at a time t_{nl} identified by the condition $\delta\rho/\rho \approx 1$. In inverse Hubble flows, t_{nl} is always smaller than the free-fall time t_{ff} of the cloud, and approaches the latter in the limit of initially small amplitude of the perturbations. Their analysis has been made for of Jeans-unstable perturbations in a cloud containing a large number of Jeans masses, while the model we made is more suitable for low mass star formation, as already reported.

6.2 Hydrodynamics in comoving coordinates

To study the dynamics of a gas in collapsing cloud cores we apply the theoretical framework derived in Sec. 5.2, neglecting the magnetic field. This is necessary, for example, to follow the evolution of a fluid accreting onto a central mass point. We want to investigate the evolution of density and velocity perturbations embedded in a background medium that is undergoing a collapse. The background medium evolves with some metric-related laws (see Sec. 5.2) and the growth of perturbations is described in a local system of Cartesian coordinates comoving with the background flow.

Consider a small Cartesian line element $\delta\mathbf{x} = (\delta x, \delta y, \delta z)$ advected by the flow, evolving as

$$\delta\mathbf{x}(t) = \mathbb{S}(t) \cdot \delta\mathbf{x}_0, \quad (6.1)$$

where $\mathbb{S}(t) = \text{diag}[a(t), b(t), c(t)]$ is the scale factor, normalized such that $\mathbb{S}(t_0) = \mathbb{I}$ and $\delta\mathbf{x}(t_0) = \delta\mathbf{x}_0$. As in Section 5.2, all hydrodynamical quantities can be split into the sum of background and local components (hereafter called *fluctuations*), as

$$\mathbf{u} = \mathbf{u}_b + \mathbf{u}_1, \quad \rho = \rho_b + \rho_1, \quad (6.2)$$

where $\mathbf{u}(\mathbf{x}, t)$ is the velocity field, $\rho(\mathbf{x}, t)$ is the gas density, and $\mathbf{x} = (x, y, z)$. In the following we will assume an isothermal equation of state, $p = c_s^2 \rho$. We then assume for the

²In cosmology, this solution corresponds to the Lemaitre-Tolman elliptic ($k = +1$) solution of Einstein's equations for a "dust" Universe

background density a spatial uniformity and for the background velocity a general metric law as 5.2,

$$\mathbf{u}_b(\mathbf{x}, t) = \mathbb{H}(t) \cdot \mathbf{x}, \quad (6.3)$$

where $\mathbb{H}(t) = \text{diag}(\dot{a}/a, \dot{b}/b, \dot{c}/c)$. Note that the dot means time derivative. Then, in the comoving coordinates defined by the transformation

$$\mathbf{x}' = \mathbb{S}^{-1}(t) \cdot \mathbf{x}, \quad (6.4)$$

the hydrodynamical equations become

$$\frac{\partial \rho_1}{\partial t} + \tilde{\nabla} \cdot (\rho \mathbf{u}_1) = -\rho_1 \text{tr} \mathbb{H}, \quad (6.5)$$

and

$$\frac{\partial \mathbf{u}_1}{\partial t} + (\mathbf{u}_1 \cdot \tilde{\nabla}) \mathbf{u}_1 + \frac{c_s^2}{\rho} \tilde{\nabla} \rho_1 + \mathbf{g}_1 = -\mathbb{H} \cdot \mathbf{u}_1, \quad (6.6)$$

where the spatial gradient $\tilde{\nabla}'$ is defined as

$$\tilde{\nabla} = \frac{1}{a} \frac{\partial}{\partial x'} \hat{\mathbf{e}}_x + \frac{1}{b} \frac{\partial}{\partial y'} \hat{\mathbf{e}}_y + \frac{1}{c} \frac{\partial}{\partial z'} \hat{\mathbf{e}}_z = \mathbb{S}^{-1} \cdot \nabla', \quad (6.7)$$

and the gravitational field \mathbf{g}_1 satisfies Poisson's equation

$$\tilde{\nabla} \cdot \mathbf{g}_1 = 4\pi G \rho_1. \quad (6.8)$$

As already introduced in Chapter 2, in this case the self-gravity of fluctuations cannot be neglected, and it has to be included into the HD equations.

6.3 Linear evolution of fluctuations

Linearizing the equations we obtain

$$\frac{\partial \delta}{\partial t} + \tilde{\nabla} \cdot \mathbf{u}_1 = 0, \quad (6.9)$$

$$\frac{\partial \mathbf{u}_1}{\partial t} + c_s^2 \tilde{\nabla} \delta + \mathbf{g}_1 = -\mathbb{H} \cdot \mathbf{u}_1. \quad (6.10)$$

where $\delta(\mathbf{x}', t) = \rho_1(\mathbf{x}', t)/\rho_b(t)$ is the density contrast.

An important quantity to consider is the vorticity of the fluid, $\boldsymbol{\omega}_1 = \nabla \times \mathbf{u}_1$, linked to

the tendency of a fluid particle to rotate or circulate at a particular point. Taking the curl of eq. (6.10) we can analyse its evolution in time,

$$\frac{\partial \boldsymbol{\omega}_1}{\partial t} = -\text{tr} \mathbb{H} \boldsymbol{\omega}_1 + \mathbb{H} \cdot \boldsymbol{\omega}_1. \quad (6.11)$$

showing that any initial vorticity is enhanced by the contraction of the cloud and becomes progressively aligned to the direction of fastest contraction. If the contraction is isotropic, eq. (6.11) reduces to

$$\frac{\partial \boldsymbol{\omega}_1}{\partial t} = -2 \frac{\dot{a}}{a} \boldsymbol{\omega}_1, \quad (6.12)$$

implying that the vorticity increases as $a(t)^{-2}$, the reverse of the so-called *natural decay* of vorticity in the expanding Universe. A more general solution of eq. (6.11) for the mean vorticity $\langle \boldsymbol{\omega}^2 \rangle^{1/2}$ has been found by Olson & Sachs (1973). They added a nonlinear term representing the breakup of larger eddies into smaller ones in the case of incompressible turbulence (a process that usually increase the mean vorticity). While in the expanding Universe this last process competes with the *natural decay* made by the global expansion, in a contracting cloud both effects tend to an unbounded increase of the mean vorticity (Olson & Sachs 1973).

Consider now compressible modes with $\mathbf{k}(t) \times \mathbf{u}_1(\mathbf{x}, t) = 0$, that couple to gravity. Taking the divergence $\tilde{\nabla}$ on both sides of eq. (6.10) and using eq. (6.9), we obtain

$$\frac{\partial^2 \delta}{\partial t^2} - c_s^2 \tilde{\nabla}^2 \delta - \frac{4\pi G \rho_0}{abc} \delta = 2 \tilde{\nabla} \cdot (\mathbb{H} \cdot \mathbf{u}_1). \quad (6.13)$$

We focus our attention on a single Fourier mode with amplitude

$$\delta(\mathbf{x}', t) = F(t) e^{i\mathbf{k}' \cdot \mathbf{x}'}, \quad (6.14)$$

where \mathbf{k}' is the (constant) comoving wavevector, related to the proper (time-dependent) wavevector $\mathbf{k}(t)$ by

$$\mathbf{k}(t) = \mathbb{S}^{-1}(t) \mathbf{k}'. \quad (6.15)$$

so that $\mathbf{k}' \cdot \mathbf{x}' = \mathbf{k}(t) \cdot \mathbf{x}$.

Inserting this expression in eq. (6.13), we obtain

$$\frac{d^2 F}{dt^2} + 2H \frac{dF}{dt} + c_s^2 \left(k^2 - \frac{k_{J,0}^2}{abc} \right) F = 0, \quad (6.16)$$

where $k = |\mathbf{k}|$,

$$H = \frac{(\dot{a}/a)k_x^2 + (\dot{b}/b)k_y^2 + (\dot{c}/c)k_z^2}{k^2} = -\frac{1}{k} \frac{dk}{dt}, \quad (6.17)$$

is the contraction rate. The initial Jeans wavenumber is

$$k_{J,0} = \frac{\sqrt{4\pi G\rho_0}}{c_s}, \quad (6.18)$$

but during the collapse it increases as

$$k_J(t) = \frac{k_{J,0}}{\sqrt{abc}}. \quad (6.19)$$

The contraction has an effect on both the wavelength $\lambda(t) = 2\pi/k(t)$ and on the amplitude of perturbations, decreasing the former and increasing the latter (see the second term on the RHS of eq. (6.16) for $H < 0$).

If the compression rate along one direction is much stronger than in the other two, fluctuations grow faster on that direction and become asymptotically two-dimensional. The wavevector of the fluctuations, that is fixed in the stretching coordinates, once evaluated in physical space becomes progressively aligned with the direction of stronger compression. An example of this is given in Sect. 6.3.2 (See i.e Fig. 6.2 and Fig. 6.1)

Introducing the variable ξ as

$$\frac{d\xi}{dt} = c_s \frac{k^2(t)}{k_{J,0}^2} \quad (6.20)$$

eq. (6.16) can be rewritten in compact form as

$$\frac{d^2 F}{d\xi^2} + \left(\frac{k_{J,0}}{k}\right)^4 (k^2 - k_J^2) F = 0, \quad (6.21)$$

which generalises the “basic equation of fragmentation theory” by Lynden-Bell (1973).

6.3.1 WKB approximation

For fluctuations on scales smaller than the Jeans length (that correspond to $k > k_{J,0}$, the effect of gravity can be neglected and perturbations oscillate. If the oscillation period of the fluctuations is much smaller than the contraction time, a WKB analysis can give an estimate of their amplitude. Let's assume

$$F(\xi) = f(\xi)e^{-i\phi(\xi)} \quad (6.22)$$

with $\phi(\xi)$ oscillating on a timescale that is much smaller than the variation of $f(\xi)$. In order to eliminate the dominant terms in eq. (6.16) we can choose

$$\frac{d\phi}{d\xi} = \left(\frac{k_{J,0}}{k}\right)^2 (k^2 - k_J^2)^{1/2}, \quad (6.23)$$

while the other largest terms give a condition that is

$$f \frac{d^2\phi}{d\xi^2} + 2 \frac{df}{d\xi} \frac{d\phi}{d\xi} = 0, \quad (6.24)$$

and implies $f^2 d\phi/d\xi = \text{constant}$. From eq. (6.23), substituting the last equation, one then obtains

$$f \propto \frac{k}{(k^2 - k_J^2)^{1/4}}. \quad (6.25)$$

If $k \gg k_J$, eq. (6.25) represents oscillations with amplitude that increases as $k(t)^{1/2}$ and an instantaneous frequency

$$\omega(t) = \frac{d\varphi}{dt} \approx c_s k(t). \quad (6.26)$$

For isotropic contraction with scale factor $a(t)$ the period of the oscillations ($k^{-1} \propto a$) becomes progressively shorter than the timescale of variation of the amplitude ($k^{1/2} \propto a^{-1/2}$). This implies that the WKB approximation becomes valid at any time, if it is satisfied initially, while in cosmology the WKB approximation is satisfied only at early times (see, e.g. Peebles 1980). At the same time, a WKB analysis of eq. (6.9) shows that

$$|\mathbf{u}_1| = c_s \delta \propto a^{-1/2}. \quad (6.27)$$

With this approximation, the action density is conserved by the compressible modes. In fact,

$$\frac{\mathcal{E}(t)}{\omega(t)} = \text{const.}, \quad (6.28)$$

where

$$\mathcal{E}(t) = \frac{1}{2} c_s^2 \delta^2 + \frac{1}{2} |\mathbf{u}_1|^2 = c_s^2 \delta^2 \quad (6.29)$$

is the energy density of the perturbations and ω is given by eq. (6.26).

Note that, in a contracting clouds, rotational modes increase faster than the compressible (wave) ones. Turbulent flows in compressible media are statistically composed of compressive (curl-free) and rotational (divergence-free) modes. In fully developed isothermal turbulence in three dimensions, the statistical ratio of compressive to solenoidal

modes is 1:2 (see e.g. Federrath et al. 2008). It could be interesting to see, given the previous results, how this ratio changes in a contracting cloud.

6.3.2 Special case: free-fall on a point mass

As an example, we find the amplification of small scale ($k \gg k_J$) fluctuations during spherical free-fall on a point mass M_\star . In this application, the fluid element is compressed in the transverse directions (say x and y), and stretched in the radial direction (say z),

$$a(t) = b(t) = \cos^2 \mu(t) \quad c(t) = 1 + \frac{\sin^2 \mu + 3\mu \tan \mu}{2}, \quad (6.30)$$

where μ is called “development angle” and it goes from 0 to $\pi/2$. It is linked to time by the parametric solution

$$t = \frac{2}{\pi}(\mu + \sin \mu \cos \mu) t_{\text{ff}}. \quad (6.31)$$

$t_{\text{ff}} = (\pi r_0^3 / 8GM_\star)^{1/2}$ is the free-fall time of a fluid element that at the initial time is at a distance r_0 from the star (see Appendix A.5 for details). While the fluid element is falling onto the central point mass, the transversal contraction and the radial stretching asymptotically become

$$a(t) = b(t) \rightarrow \left(1 - \frac{t}{t_{\text{ff}}}\right)^{2/3}, \quad c(t) \rightarrow \left(1 - \frac{t}{t_{\text{ff}}}\right)^{-1/3}. \quad (6.32)$$

According to eq. (6.15), the proper wavevector \mathbf{k} of a fluctuation becomes asymptotically oriented in the transverse direction, parallel to the direction of compression.

As already stated in Sect. 6.3.1, cases in which an anisotropic contraction can amplify some components while damping some others can exist. In this case we know from the kinematics of sound waves that $\mathbf{k} \times \mathbf{v} = 0$ and, because the wave action is conserved in the linear regime, we have $\mathcal{E}(t) = \text{const}$. Thus, if we identify with “ t ” the transverse components and “ r ” the radial one,

$$k = \sqrt{\left(\frac{k_r^2}{k_t^2} + 1\right)} k_t^2; \quad v^2 = \left(\frac{k_r^2}{k_t^2} + 1\right) v_t^2. \quad (6.33)$$

That allows us to find an analytical expression for both the velocity components of the

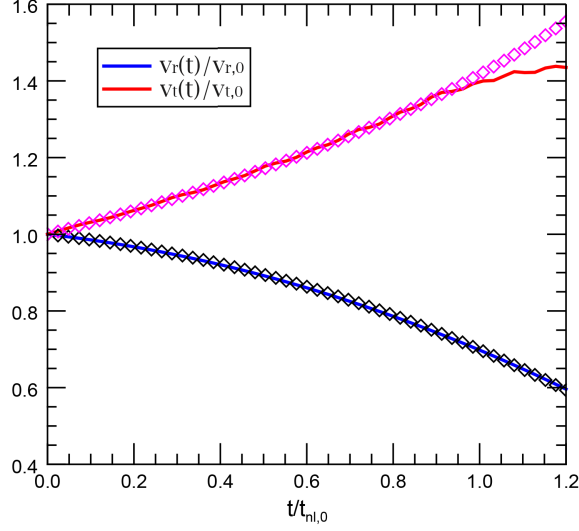


Figure 6.1: Behaviour of transverse and radial components of velocity fluctuations in the case of a free fall collapse with $t_{ff} = 2t_{nl,0}$. The initial condition is a perturbation with $k_{p,0} = k_{t,0} = k_0 = 1$ and a given $t_{nl,0} = 10$ in code units (see Sect. 6.5). The continuous lines are from the simulation and the diamonds are the analytical expectations. As we can see, while the kinematic relation is always valid, the conservation of the wave action breaks up in the non-linear regime. From Toci et al. (2017).

wave (and then, also for the density contrast). For a wave with $k_{r,0} = k_{t,0} = k_0$ we have

$$v_t = Q' \frac{a^{-1/3}}{(a^2 + 1)^{1/4}}, \quad (6.34)$$

where $Q' = \sqrt{\mathcal{E}_0 c_s k_0} = 2^{1/4} v_{t,0}$. Fig. 6.1 shows the behaviour of the velocity fluctuation components for a perturbation, while Fig. 6.2 shows their evolution as function of time.

In fact, considering eq. (6.25), the amplitude of a density perturbation that is propagating at an angle θ (fixed in the comoving frame) with respect to the radial direction increases as

$$\delta = \delta_0 \left(\frac{\sin^2 \theta}{a^2} + \frac{\cos^2 \theta}{c^2} \right)^{1/4}, \quad (6.35)$$

where the scale factors $a(t)$ and $c(t)$ are given by eq. (6.32). Fig. 6.3 shows the evolution of δ for perturbations with wavenumber radial ($\theta = 0$) or transversal ($\theta = 90^\circ$). The

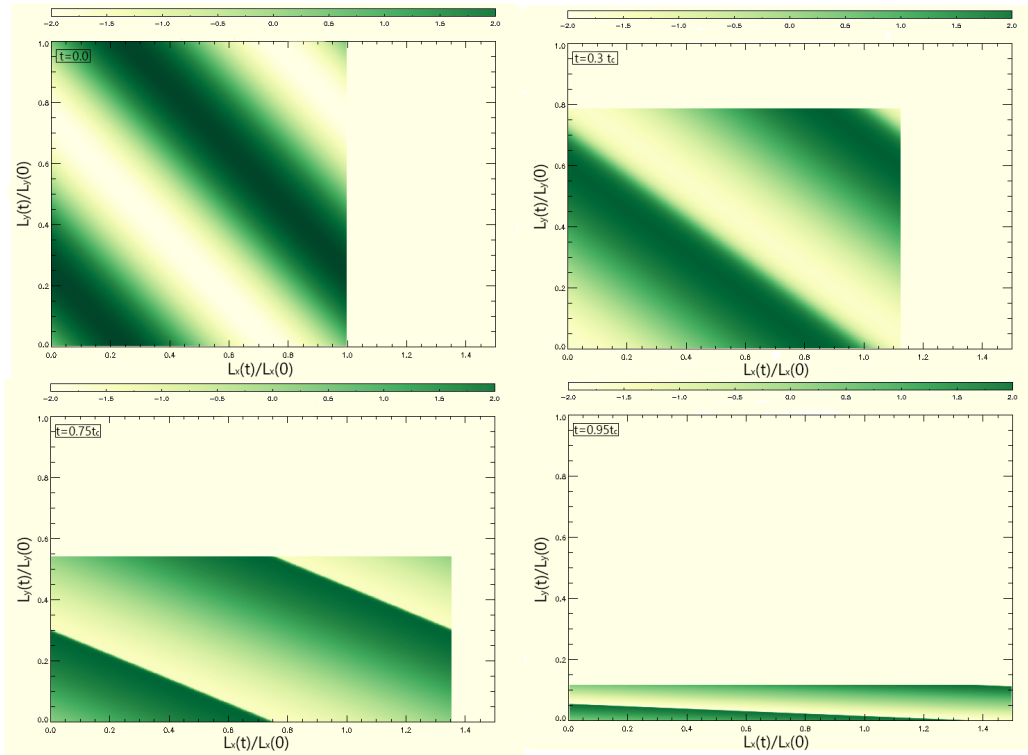


Figure 6.2: Surface plot per the transverse components of the velocity at different time for the same case of Fig. 6.1. At the initial time the oblique wave has $k_t = k_r$. During the evolution, the ratio between the wavevectors components changes, and the wave progressively aligns with the direction of compression (the transverse). During the propagation the wave-front steps until it forms a shock. From Toci et al. (2017).

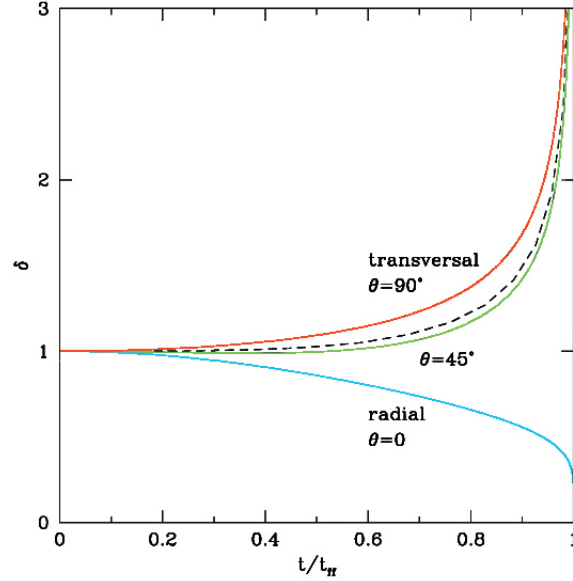


Figure 6.3: Amplitude of density perturbations during spherical free-fall on a point mass, for perturbations with wavenumber radial ($\theta = 0$) and transversal ($\theta = 90^\circ$). The dashed line shows the evolution of the amplitude for a random distribution of wavenumbers. From Toci et al. (2017).

dashed line shows the evolution of the amplitude for a random distribution of wavenumbers obtained averaging eq. (6.35) over θ . Thus, a collection of fluctuations with randomly oriented wavevectors grows preferentially in the direction transverse to the accretion flow. However, a fluid element contracts in two directions and is stretched in the third, then the increase of perturbations is relatively slow: the average amplitude doubles only after 95% of the free-fall collapse of the fluid element has been completed. An even smaller amplification is expected in the case of accretion flows on a filament, if we can approximate the filament as an infinite cylinder, because contraction in this case can only occur in the direction perpendicular to the filament.

Generally, we can state that anisotropic collapse and stretching of fluid elements in this kind of flows driven by the gravitational field of mass concentrations like stars or filaments dilute and retard the growth of any small-scale density/velocity perturbation initially present in the gas. In the next Section we will focus on the homologous collapse of a starless, self-gravitating cloud core in which the amplification of perturbations is expected to occur at the highest possible rate.

6.4 Application to homologous collapse

Starless cores seem to have a dynamics characterised by an overall slow contraction rather than free-fall collapse in their central parts [Keto et al. \(2015\)](#). However, even if the model of the homologous collapse of a uniform density pressureless sphere is an idealisation, it contains all the essential characteristics of flows driven by the self-gravity of the gas ([Whitworth & Ward-Thompson 2001](#)). In addition, it easy allows us to derive analytically the time evolution of the scale factors needed to apply the formalism of inverse Hubble flows.

In this framework, the acceleration of the background comes from the self-gravity of the core,

$$\nabla' \cdot \mathbf{g}_b = 4\pi G\rho_b, \quad (6.36)$$

where $\rho_b = \rho_0/a^3$, and the scale factor is

$$a(t) = \cos^2 \mu(t), \quad (6.37)$$

where μ is taken again from eq. (6.31) and $t_{\text{ff}} = (3\pi/32G\rho_0)^{1/2}$ is the free-fall time (see Appendix A.5 for details). With these definitions eq. (6.16) becomes

$$\frac{d^2 F}{d\mu^2} - 2 \tan \mu \frac{dF}{d\mu} + 6 \left(\frac{k'^2}{k_{J,0}^2} - \frac{1}{\cos^2 \mu} \right) F = 0. \quad (6.38)$$

How a density perturbation evolves depends on its initial spatial scale. Consider the evolution of small-scale, Jeans-stable perturbations with $k' \gg k_{J,0}$. In a static cloud, such kind of fluctuations behave as sound waves, oscillating with frequency $\omega = c_s k$. If the cloud contracts isotropically with scale factor a , the dimension of the perturbation decreases as a (and its oscillation frequency increases as a^{-1}) but the Jeans length decreases faster because $c_s/\sqrt{\rho} \sim a^{3/2}$. Then, any small-scale perturbation that starts linearly stable and propagates as sound waves becomes gravitationally unstable at some time $t_{\text{gr}}(k')$, that tends to t_{ff} as $k' \rightarrow \infty$. Using eq. (6.38), this time corresponds to $\cos^2 \mu_{\text{gr}} = k_{J,0}^2/k'^2$. In this limit, the solution of eq. (6.38) is

$$F(\mu) = \frac{1}{\cos \mu} [c_1 \sin(p\mu) + c_2 \cos(p\mu)], \quad (6.39)$$

where $p = \sqrt{6}k'/k_{J,0} \gg 1$. This represents two oscillating modes (with $F(0) = 0$ and $dF/d\mu(0) = 0$, respectively). As anticipated by the WKB analysis, the amplitude of the

perturbations increase as $1/\cos\mu \propto a^{-1/2}$.

While the cloud undergoes a contraction, a decreases, and eventually perturbations on scales progressively small become gravitationally unstable. When $k' \ll k_{J,0}$, eq. (6.38) becomes

$$\frac{d^2F}{d\mu^2} - 2 \tan\mu \frac{dF}{d\mu} - \frac{6}{\cos^2\mu} F = 0. \quad (6.40)$$

General solutions of this equation are well known from cosmology (see i.e Narlikar 2002).

With the initial conditions appropriate for cloud collapse the solution is (Toalá et al. 2015),

$$F(\mu) = c_1 \frac{\tan\mu}{\cos^2\mu} + c_2 \frac{2 + \sin^2\mu + 3\mu \tan\mu}{\cos^2\mu}. \quad (6.41)$$

This solution represents two growing modes (with $F(0) = 0$ and $dF/d\mu(0) = 0$, respectively). When the time asymptotically goes to $t \rightarrow t_{\text{ff}}$ both modes grow like $a^{-3/2} \propto (1 - t/t_{\text{ff}})^{-1}$. Fluctuations become gravitationally unstable at a time $t_J(\lambda')$, that corresponds to the evolutionary angle

$$\cos\mu_J = \frac{\lambda'}{\lambda_{J,0}}. \quad (6.42)$$

This implies that, in a free-falling background, small-scale, Jeans-stable perturbations are amplified as $a^{-1/2}$ until they become gravitationally unstable and then grow as $a^{-3/2}$, the same rate characterising the evolution of the parent cloud, which is itself gravitationally unstable ($H \propto (1 - t/t_{\text{ff}})^{-1}$).

6.4.1 Onset of nonlinearity

The linear approximation breaks down at some point because the amplitude of the waves increases with time. Linear growth ends when perturbations become Jeans-unstable and collapse, or when they become nonlinear, at a time t_{nl} , and start to dissipate their energy by shocks. After t_{nl} the energy dissipation is extremely efficient, because shocks convert wave energy into heat.

To evaluate t_{nl} , we reduce for simplicity our analysis to a one-dimensional flow. Neglecting pressure and gravity, the momentum equation (5.24) reduces to a modified Burgers' equation (See Section 2.3.1)

$$\frac{\partial u_1}{\partial t} + \frac{u_1}{a} \frac{\partial u_1}{\partial x'} = -H u_1. \quad (6.43)$$

Making a coordinate transformation $v_1 = a u_1$ and $d\tau = a^{-2} dt$, eq. (6.43) can be rewritten

in the new variables $v_1(x', \tau)$ and τ as the standard (inviscid) Burgers' equation for the static case,

$$\frac{\partial v_1}{\partial \tau} + v_1 \frac{\partial v_1}{\partial x'} = 0. \quad (6.44)$$

The general (implicit) solution of eq. (6.44) can be found with the method of characteristics: starting with a velocity perturbation with initial amplitude $v_1(x', 0) = u_1(x', 0)$, it will steepen with time and form a shock at a time

$$\tau = -\left\{ \min \left[\frac{du_1(x', 0)}{dx'} \right] \right\}^{-1} \equiv t_{\text{nl},0}, \quad (6.45)$$

where $t_{\text{nl},0}$ is the time for reaching the nonlinear stage in the static case. In the presence of contraction, nonlinearity therefore occurs at a time t_{nl} such that

$$\int_0^{t_{\text{nl}}} \frac{d\tau}{a^2} = t_{\text{nl},0}. \quad (6.46)$$

Obviously, in the case of contraction $t_{\text{nl}} < t_{\text{nl},0}$, meaning that perturbations enter the nonlinear phase earlier than in the static case, and this time is the one that has to be compared with the other time scales of the problem.

We now will evaluate t_{nl} in the case of the homologous collapse of a pressureless sphere. A sinusoidal velocity perturbation with wavelength $\lambda' = 2\pi/k'$ and initial amplitude u_0 becomes nonlinear and forms a shock at $t = t_{\text{nl}}$, corresponding to the evolutionary angle μ_{nl} obtained integrating eq. (6.46),

$$t_{\text{nl},0} = \frac{4t_{\text{ff}}}{\pi} \int_0^{\mu_{\text{nl}}} \frac{d\mu}{\cos^2 \mu} = \tan \mu_{\text{nl}}. \quad (6.47)$$

For $t_{\text{nl},0} = 1/(k'u_0)$, this implies

$$\tan \mu_{\text{nl}} = \frac{\lambda'}{8t_{\text{ff}}u_0}. \quad (6.48)$$

Our goal is to compare t_{nl} and t_{gr} . It is convenient to parametrize the amplitude of the perturbations as $u_0 = \mathcal{M}_0 c_s$, where \mathcal{M}_0 is the initial value of the rms Mach number, and rewrite eq. (6.48) as

$$\tan \mu_{\text{nl}} = \left(\frac{1}{\sqrt{6}\mathcal{M}_0} \right) \frac{\lambda'}{\lambda_{\text{J},0}}. \quad (6.49)$$

Fig. 6.4 shows the time t_{nl} and t_{G} at which initially Jeans-stable perturbations become nonlinear and gravitationally unstable, respectively, for various values of the rms Mach

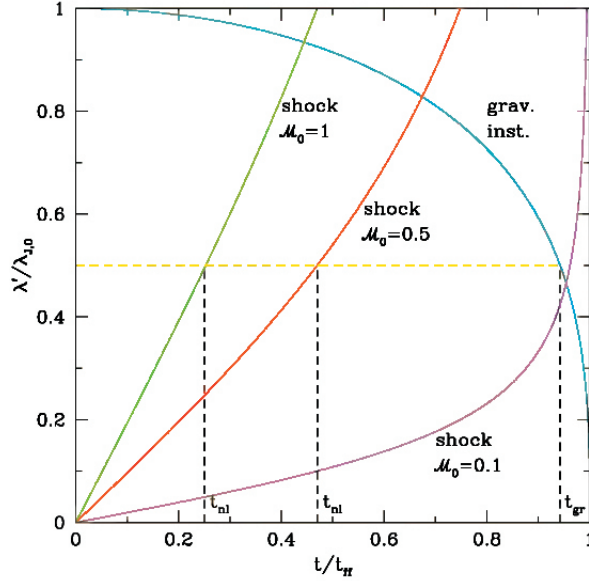


Figure 6.4: During the collapse of a pressureless cloud, a linear perturbation with comoving wavelength λ' becomes nonlinear at a time t_{nl} (curves labelled “shock”) and gravitationally unstable at a time t_{G} (curve labelled “grav. inst.”). Wavelength is in units of the Jeans wavelength $\lambda_{\text{J},0}$ and time is in units of the cloud’s free-fall time t_{ff} . The non-linear time is shown for three values of the initial Mach number of the perturbations, $\mathcal{M}_0 = 1$, $\mathcal{M}_0 = 0.5$ and $\mathcal{M}_0 = 0.1$. The case of $\lambda' = 0.5 \lambda_{\text{J},0}$ is shown as an example: the nonlinear phase is reached before the gravitational instability, unless the perturbations have Mach number below ~ 0.1 . From Toci et al. (2017).

number representative of the level of non-thermal motions observed in dense cores, where typically $\mathcal{M}_0 \approx 0.1\text{--}1$ (see Chapter 1). Both t_{nl} and t_{gr} are bounded from above by t_{ff} , but they are related to the (comoving) scale of the perturbation λ' in opposite ways: while t_{g} increases if λ' decreases, t_{nl} becomes smaller. This allows perturbations on sufficiently small scales to enter the nonlinear phase when they are still gravitationally stable. As an example, if $\lambda' = 0.5 \lambda_{\text{J},0}$, the nonlinear stage and the formation of shocks is reached at $t_{\text{nl}} = 0.26 t_{\text{ff}}$ and $t_{\text{nl}} = 0.47 t_{\text{ff}}$ for $\mathcal{M}_0 = 1$ and 0.5 , respectively, well before the perturbation becomes gravitationally unstable at $t_{\text{G}} = 0.94 t_{\text{ff}}$.

6.5 Numerical simulations

According to the results of Sect. 6.3, initially small-scale low-amplitude density perturbations are amplified adiabatically during the contraction of a cloud, until they become nonlinear and start to dissipate their energy by shocks. After t_{nl} the energy dissipation is extremely rapid, as shocks efficiently convert wave energy into heat.

In order to follow the behaviour of small-scale non-self gravitating perturbations beyond the linear stage in a contracting background we use the ECHO code (already introduced in Chapter 5), performing 3D hydrodynamical numerical simulations. Physical quantities are normalised using the sound speed, a characteristic length and a characteristic density. In this (isothermal) case the adiabatic index $\gamma = 1$. The time is expressed in terms of sound crossing time.

In these simulations we assumed an isotropic contraction from $t = 0$ to $t = t_c$ with scale factor

$$a(t) = \left(1 - \frac{t}{t_c}\right)^\alpha, \quad (6.50)$$

and contraction rate

$$H(t) = \frac{\dot{a}}{a} = -\frac{\alpha}{t_c} \left(1 - \frac{t}{t_c}\right)^{-1}. \quad (6.51)$$

The range of α of physical interest is $0 < \alpha < 2/3$. Special cases are the static background ($\alpha = 0$), a quasi-static collapse ($0 < \alpha < 2/3$), and a dynamical collapse ($\alpha = 2/3$). We also studied the case $\alpha = 1$.

Fig. 6.5 and 6.6 shows the evolution of the density contrast, normalised to the initial value, for the cases $\alpha = 2/3$ and $\alpha = 1$, respectively, obtained with a Cartesian grid $[0, L_x] \times [0, L_y] \times [0, L_z]$ of 512^3 points, $L_x = L_y = L_z = 2\pi$. In the simulations, for a given α we fix the initial amplitude of the perturbations to $\delta_0 = 0.1$ and take as reference time the nonlinear time $t_{\text{nl},0}$ for the static case. We then vary the contraction time, increasing it progressively, $t_c/t_{\text{nl},0} = 20, 10, 2, 1.25$ and we analyse the evolution of perturbations with time. We have run the same simulations with increasing spatial resolutions, checking that for 512^3 grid points convergence was achieved. Using the scale factor given by eq. (6.50), the perturbations are expected to become nonlinear at a time t_{nl} given by eq. (6.46),

$$\frac{t_{\text{nl}}}{t_{\text{nl},0}} = \frac{t_c}{t_{\text{nl},0}} \left\{ 1 - \left[1 - (1 - 2\alpha) \frac{t_{\text{nl},0}}{t_c} \right]^{1/(1-2\alpha)} \right\}. \quad (6.52)$$

Fig. 6.5, shows that the evolution of a perturbation depends on the time scale of the contraction of the box. The growth phase follows strictly the adiabatic (conserving wave

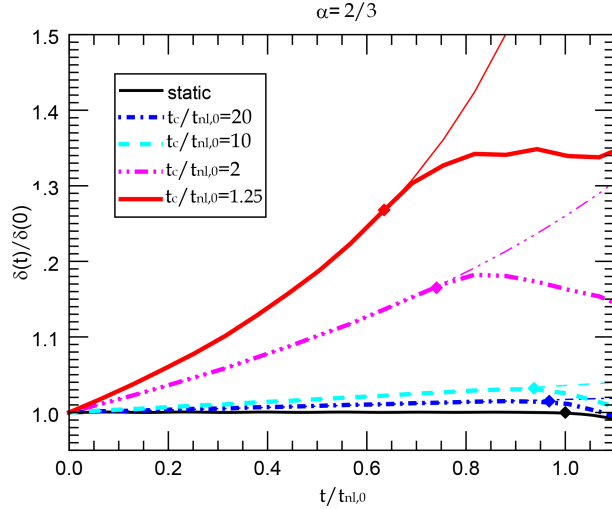


Figure 6.5: Time evolution of the rms amplitude of density perturbations in an isothermal gas contracting isotropically with the scale factor of eq. (6.50) with $\alpha = 2/3$ (case of dynamical contraction) for various values of t_c (*thick lines*). Time is in units of $t_{nl,0}$, the nonlinear time for the static model. A *diamond* marks the position of t_{nl} given by eq. (6.52), and *thin lines* show the evolution of the amplitude in the WKB approximation. For $t > t_{nl}$ shocks are formed and the waves dissipate. From Toci et al. (2017).

energy) approximation $\delta \propto a(t)^{-1/2}$ until nonlinear effects occur. Their effect is to steepen the waves and form shocks. The analytical expression eq. (6.52), that comes from the one-dimensional inviscid Burgers' equation predicts the end of the adiabatic phase and the beginning of the dissipative phase, and it is in good agreement with the numerical results. The figure shows that t_{nl} is considerably reduced compared with the static case if the contraction occurs on a time scale of the order of a few $t_{nl,0}$. If $t_c \approx t_{nl}$ the amplification due to contraction roughly balances the decay due to dissipation, maintaining an almost constant value of the rms of density (and velocity) perturbations.

6.6 Summary

In this Chapter we studied the evolution of small-scale hydrodynamic perturbations during the contraction of a core, generalising the analytical approach already developed for cosmology (expanding Universe) to the case of arbitrary anisotropic inverse Hubble

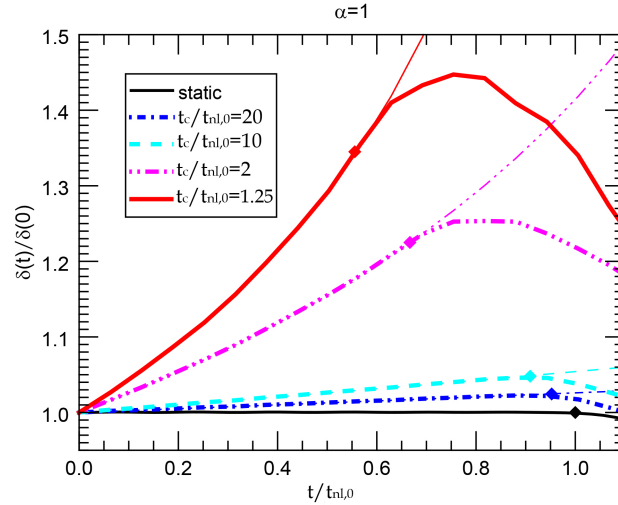


Figure 6.6: Same as Fig. 6.5 for $\alpha = 1$. From Toci et al. (2017).

flows. Generally, gravity-driven anisotropic flows, like those characterising the accretion onto point-like or filament-like mass concentrations, have less effects than isotropic flows generated by the self-gravity of a cloud core in the amplification of density and velocity perturbations, because the effect of the stretching of fluid elements are diluted in the direction of the flow.

There are differences also between the isotropic case and the expanding Universe, where both solenoidal and compressible modes decay due to the expansion of the Universe. Only the gravitational instability can promote the formation of substructures. In a contracting cloud, solenoidal and compressible perturbations grow with time, the former faster than the latter (as a^{-2} or faster, in the isotropic case). Thus vortex structures are promoted to form preferentially aligned to the direction of faster contraction. This process may create local enhancements of angular momentum even in the absence of any bulk rotation of the core, and core fragmentation may be generated from the break-up of rotationally supported substructures, as found e.g. in the simulations by Goodwin et al. (2004). Conversely, the amplitude of compressible modes in the WKB approximation grows as $a^{-1/2}$ in the isotropic case and conserves the wave action density. These modes couple to the gravitational field, and become gravitationally unstable as the Jeans length progressively shrinks (as long as the collapse is isothermal), leading to fragmentation. However, the actual fate of compressible perturbations depends in general on their wavelength and amplitude, and is controlled by the comparison between several timescales:

the time to reach the nonlinear stage t_{nl} , the time at which perturbations become gravitationally unstable t_{gr} , and the global collapse time scale of the background. The nonlinear time in a collapsing cloud, bounded from above by the free-fall time t_{ff} , is shorter than in a static background, and can be estimated analytically using a one-dimensional Burgers' equation in contracting coordinates. For the typical amplitudes of velocity perturbations observed in cloud cores ($\delta u/c_s \approx 0.5-1$), in general $t_{\text{nl}} < t_{\text{gr}}$, according to their wavelength. Only perturbations on scales larger than $\sim 80-90\%$ of the initial Jeans length (of the same order of the size of the core), become Jeans-unstable in the linear phase. The others start to dissipate their energy forming shocks, establishing a competition with the “adiabatic heating” resulting from contraction.

Our analytical expectations are supported by fully three-dimensional numerical calculations performed with the hydrodynamical code ECHO. These simulations confirm that initially linear perturbations in a box that contracts isotropically increase their amplitude as predicted by the WKB analysis up to the time t_{nl} . As shown by the simulations, t_{nl} marks the onset of a phase of decay of the perturbations' amplitude due to strong energy dissipation by shocks. If the rapid amplitude decay following t_{nl} suggested by the numerical calculations is representative of the dissipation in cloud core, it is unlikely that small-scale perturbations can survive to the point of becoming self-gravitating and unstable. In this scenario, multiple fragmentation in cores is likely achieved by the growth and subsequent breakup of solenoidal, rather than compressible, small-scale perturbations, either through the fragmentation of disk-like structures (Goodwin et al. 2004), or by the accumulation of mass at the boundary between nearby anti-parallel vortices. However, vortices are easily disrupted by any large-scale magnetic field due to magnetic stresses associated to current sheets at their edges, an aspect that should be addressed in future works.

7

Magnetohydrodynamics in contracting volumes

As shown in Chapter 1, turbulence is expected to play an important role in star formation, as suggested by the Larson’s laws (Larson 1981), that establishes a power-law relation among velocity dispersion, size, and mass in molecular clouds (see i.e Elmegreen & Scalo 2004). More recent observations of size-dispersion relations found in the literature are in agreement with an interpretation in terms of compressible turbulence (see i.e Heyer et al. 2009, or the review Dobbs et al. 2014).

Molecular clouds appear to be in an approximate virial equilibrium (Larson 1981, Solomon et al. 1987), thus turbulent pressure can either balance the self-gravity of the cloud or the confining pressure given by the interclump medium (Bertoldi & McKee 1992). The concept of a turbulent pressure being still not well understood (Vázquez-Semadeni et al. 1998), is then important to understand the origin and the evolution of turbulence in molecular clouds. We recall that, if not sustained, turbulence dissipates in a crossing time (Goldreich & Kwan 1974), which is shorter than the cloud lifetime (Blitz & Shu 1980). To provide support against gravitational collapse, turbulence needs some “driving”, or it will quickly dissipates (Mac Low & Klessen 2004). However, the cloud lifetime is uncertain and still debated, as pointed out in Chapter 1, due to the fact that molecular clouds are not generally gravitationally bound nor perfectly balanced.

Numerical simulations have studied in detail supersonic turbulence. The power spectrum of isothermal supersonic turbulence seems to have a lognormal density distribution that increases with the Mach number (Federrath et al. 2010), independent of the numerical methods implied. As pointed out by Robertson & Goldreich (2012), numerical simulations of turbulence usually consider a gas cloud in a fixed volume, while astrophysical clouds expand or contract. Robertson & Goldreich (2012) studied the behaviour of hydrodynamical turbulence during an isotropic collapse (inverse Hubble flow as in Toalá et al.

2015), given by an external pressure or self-gravity, finding that turbulence is sustained by contraction and *adiabatically* heats up if the time-scale of the contraction is longer than the eddy turnover time (see below). They also suggested that the relation between velocity dispersion and size may be linked to the competition between the enhancement of fluctuations and dissipation. The main goal of this Chapter is to study numerically the

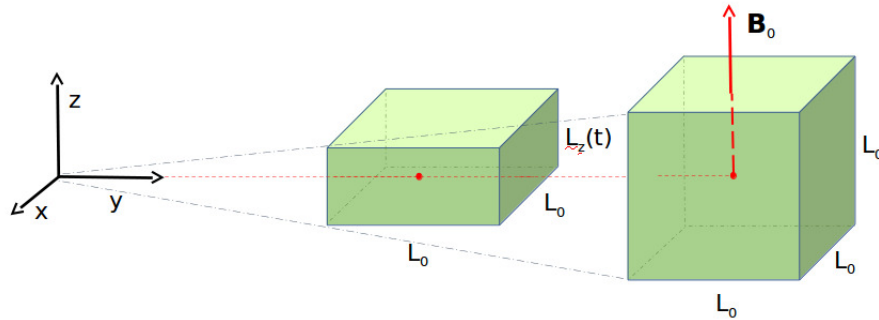


Figure 7.1: Contraction along a mean magnetic field.

temporal evolution of a magnetised and turbulent element of fluid in a contracting cloud (or a contracting core). The fluid element is contracting along the direction of the mean magnetic field (see Fig. 7.1), a scenario that mimics the accretion of mass on a filament. In particular, we will follow the evolution of the properties of turbulence (fluctuations of velocities and densities, spectral shape, dissipation times, etc.) in a gas parcel contracting along the magnetic field lines with different contracting time-scales in order to determine the conditions for amplification or quenching of the turbulent fluctuations. Our interest focus onto fluctuations due to the fact that they are directly linked to the observable quantities in molecular clouds and cores.

To achieve this goal we adopt the magnetohydrodynamical code ECHO (Del Zanna et al. 2007), already described in Chapter 5 (we already used this code in Chapter 6 for HD 3D simulations). If we choose a direction for the ambient magnetic field (say the z direction), we can represent the effects of self-gravity of the cloud with a non-isotropic metric tensor

$$g_{ij} = \text{diag}[1, 1, a^2(t)], \quad \sqrt{g} = a(t). \quad (7.1)$$

In this thesis we choose the contraction to be linear, then

$$a(t) = a_0 \left[1 - \frac{t - t_0}{t_c} \right], \quad (7.2)$$

where t_0 is the time when the contraction starts, t_c is the contraction time at the initial time t_0 , a_0 is the initial scale factor ($a_0 = L/L_0 = 1$, with L_0 the initial size). Our choice implies a decreasing contraction rate,

$$H = \left| \frac{\dot{a}}{a} \right| = [t_c - (t - t_0)]^{-1}, \quad (7.3)$$

defined in analogy with cosmology and the previous work (see Chapter 6). We are interested in studying the behaviour of a turbulent fluid during contractions with different t_c in order to understand whether, also in this anisotropic MHD case, turbulent motions could be amplified or quenched during the collapse. This depends on the ratio of the contraction time scale $1/H$ and the eddy turnover time (we will use this definition to estimate the *non-linear* time associated with the scale of dissipation),

$$t_{eddy} = \frac{1}{k_{inj} u_{rms}}, \quad (7.4)$$

where k_{inj} is the wavenumber corresponding to the larger scale in our domain and u_{rms} is the root-mean square amplitude of velocity fluctuation. While the behaviour of H is imposed in our simulations, the eddy turnover time is determined during simulations as a balance between amplification of u_{rms} due to contraction and damping due to turbulent dissipation.

In Section 7.1 and 7.2 we introduce the numerical setup for the simulations while in Section 7.3 we describe how we prepare the initial condition for runs with contraction switched on. The initial condition for all contracting simulations is a snapshot of fully developed turbulence taken from a simulation of decaying turbulence initialised with a superposition of random-phase Alfvénic fluctuations. In Section 7.4 we turn on the contraction with different values of t_c and we study the behaviour of the simulations. Finally, in Section 7.5 we summarise the characteristics of this physical case.

7.1 Numerical setup

We integrate numerically the resistive MHD equations in contracting volumes, with the hypothesis that the gas is isothermal ($\gamma = 1$). Physical quantities are normalised using a characteristic length-scale, a characteristic density and a characteristic magnetic field strength $B_0/\sqrt{4\pi}$ (where B_0 is the background value measured for the molecular cloud). The reference velocity is the Alfvén velocity and time is expressed in terms of the Alfvén crossing time. As a consequence, the fluid pressure is in unit of $B_0^2/4\pi$.

From Section 5.2, MHD equations in comoving coordinates are

$$\frac{\partial \rho}{\partial t} + \rho \mathbb{M} \cdot \nabla' \cdot \mathbf{u} = -\rho \text{tr} \mathbb{H}, \quad (7.5)$$

$$\frac{\partial \mathbf{u}}{\partial t} + \frac{1}{\rho} \mathbb{M} \cdot \nabla' P + \frac{\mathbf{B}}{4\pi\rho} \times (\mathbb{M} \cdot \nabla' \times \mathbf{B}) - \zeta (\mathbb{M} \cdot \nabla')^2 \mathbf{u} = -\mathbb{H} \cdot \mathbf{u}, \quad (7.6)$$

and

$$\frac{\partial \mathbf{B}}{\partial t} + \mathbb{M} \cdot \nabla' \times (\mathbf{B} \times \mathbf{u}) - \eta (\mathbb{M} \cdot \nabla')^2 \mathbf{B} = \mathbf{B} \cdot (\mathbb{H} - \mathbb{I} \text{tr} \mathbb{H}), \quad (7.7)$$

where $\mathbb{H} = \text{diag}(0, 0, \dot{a}/a)$ and $\mathbb{M} \cdot \nabla'$ is the spatial gradient in the comoving reference system. The equation for the pressure (or the temperature) can be omitted due to the fact that we choose an isothermal equation of state. Note also that we choose a linear rate of contraction H , thus the term $-\mathbb{W} \cdot \mathbf{x}'$ in eq. (7.6) is equal to zero¹. Viscosity ($\zeta=0.001$ in code units) and resistivity ($\eta=0.001$ in code units) different from zero have been fixed for all the simulations, in order to guarantee the stability of the code. We are not trying to model any realistic physical process with this choice: a proper resistivity and viscosity is required to prevent the accumulation of energy in fluctuations at small scales.

We solve this system of equations in a cubic domain $[0, L_x] \times [0, L_y] \times [0, L_z]$ with $L_x = L_y = L_z = 2\pi$ and resolution $N_x = N_y = N_z = 512$ points with periodic boundary conditions.

In order to start contraction with a fully-developed turbulence we first run a static simulation, i.e. with $\mathbb{H} = 0$ and $\mathbb{M} = \mathbb{I}$ in eqs. (7.5)-(7.7). We initialise the static case with a superposition of shear of Alfvén waves with random phases exciting modes $1 < k_{x,y,z} < 4$ with equal energy. This corresponds to an isotropic initial spectrum and fluctuation with only components perpendicular to the ambient magnetic field $\mathbf{B}_0 = B_0 \hat{\mathbf{e}}_z$. We anticipate that the contraction axis coincides with the mean field direction, thus we will use the subscripts (\parallel, \perp) to denote directions along z and lying on the (x, y) plane.

The initial conditions for the velocity fluctuations read:

$$\mathbf{u}_{\perp}(x, y, z) = \frac{1}{2} \sum_{k_x, k_y, k_z} [\mathbf{u}_{\perp}(k_x, k_y, k_z) \exp[i(k_x x + k_y y + k_z z + \phi_u(k_x, k_y, k_z))]], \quad (7.8)$$

and, in the same way, the initial magnetic fluctuations

$$\mathbf{b}_{\perp}(x, y, z) = \frac{1}{2} \sum_{k_x, k_y, k_z} [\mathbf{b}_{\perp}(k_x, k_y, k_z) \exp[i(k_x x + k_y y + k_z z + \phi_b(k_x, k_y, k_z))]], \quad (7.9)$$

¹See eq. (2.9) in Section 5.2.

with different random phases ϕ . These initial conditions have been used in different works as initial conditions for the solar wind turbulence (see, i.e. [Franci et al. 2015](#)).

The value of the initial mean density and magnetic field is 1 in the code unit, while the pressure is dependent from the value of the plasma β ($P = 1/2\beta B_0^2$). The initial condition has no mean velocity. The values of the amplitude of fluctuations and the plasma β are parameters to be chosen to set proper initial conditions for the ISM.

Different physical parameters characterise different phases of the ISM (see Chapter 1). Table 7.1 shows the values for three phases: the diffuse ISM, molecular clouds and dense cores.

	Diffuse ISM	Molecular cloud	Low mass dense core
Size L (pc)	10	5	0.1
Density n cm^{-3}	30	200	10^3
Temperature T (K)	100	10	5
Magnetic field (μG)	5	10	100
Velocity dispersion σ :			
Line of sight component (km/s)	4	1	0.2
Total 3D velocity (km/s)	7	2	0.3
Sound speed c_s	0.6	0.2	0.2
Alfvén speed v_A	1	1	1
Plasma $\beta = 2c_s^2/v_A^2$	0.7	0.08	0.08
Turbulent Mach $\mathcal{M}_s = \sigma/c_s$	12	10	1
Alfvénic Mach $\mathcal{M}_A = \sigma/v_A$	1	2	0.3

Table 7.1: Physical parameters for the ISM

We impose energy equipartition and vanishing correlations between magnetic and velocity fluctuations by choosing $u_\perp = b_\perp = 0.5$ and $\beta = 0.5$. These values are appropriate for a fluid element of a core resulting in $\mathcal{M}_s = u_{rms}/c_s = 1$ and $\mathcal{M}_A = u_{rms}/v_A = 0.5$. We let the static simulation evolve and we describe its properties in Sect. 7.3. The initial condition for runs with contraction is a snapshot of fully-developed turbulence, taken after the peak of turbulent dissipation.

7.2 Basic quantities

We will analyse quantities that can be directly compared with observables in the ISM, such as the density contrast, which is the ratio between the density fluctuation and the mean value of the density $\delta = \rho_{fluct}/\rho_{mean}$, the rms of velocity and magnetic field (related to the large scale motions), the Mach numbers of the fluctuations (\mathcal{M}_A and \mathcal{M}_s) and

parameters that depend on mean quantities like the plasma β . For example, the rms of velocity can be associated with non thermal motions observed in the emission lines (see Chapter 1). We define the 1D *isotropised* velocity spectrum as

$$\mathcal{E}_k(k) = \int |\hat{u}|^2 \sin \theta d\theta d\phi dk, \quad (7.10)$$

where $\hat{u} = \sum_{i=x,y,z} |\hat{u}_i|^2$ is the sum of the 3D Fourier coefficients of the 3 components of velocity fluctuations, k is the wavenumber and the value of the spectra is built by averaging the spectral density within spherical shells of radius k . A further integration in k yields the root mean square amplitude (rms):

$$u_{rms} = \int \mathcal{E}_k dk = \sqrt{\langle u^2 \rangle - \langle u \rangle^2}, \quad (7.11)$$

where $\langle \dots \rangle$ is the space average over the full 3D domain. Replacing \hat{u} with \hat{b} we obtain the same quantities for the magnetic fluctuations. Similar definitions hold for the density fluctuations. Other important quantities are the kinetic and magnetic *enstrophy*, integrals of vorticity and current in the domain,

$$\Omega_k = \int |\nabla \times \mathbf{u}|^2 d^3x, \quad \Omega_m = \int |\nabla \times \mathbf{B}|^2 d^3x. \quad (7.12)$$

These quantities are directly related to the dissipation of the incompressible part of the kinetic energy and of magnetic energy. They can be used to estimate the time at which the turbulence is fully developed. In fact, the maximum of the enstrophy corresponds to the time of maximum turbulent activity for incompressible flows² (Mininni & Pouquet 2009).

From a numerical point of view, the time evolution of enstrophy emphasises the properties of the numerical scheme and the inaccuracy of discretisation. For this reason, it can be used to understand whether the resolution can resolve the small scales, a crucial point for turbulent simulations. The nonlinearity of MHD equations leads to a transfer of energy and enstrophy between scales, in particular for a given simulation energy reach the discretisation at a scale which is an intrinsic limitation. A well resolved simulation of decaying turbulence does not show an accumulation of enstrophy in time: the enstrophy first increases and then decreases due to the effects of viscosity (and resistivity). In a decaying simulation in which not all the scales are resolved, the enstrophy increase monotonically

²This time can be also used as an estimate of the "effective" non-linear time t_{nl} , the estimate $t_{nl} \sim 1/k_0 u_{rms}$ can underestimate the time associated with the conversion between kinetic and internal energy.

and eventually saturates (Orlandi 2000).

7.3 Static case

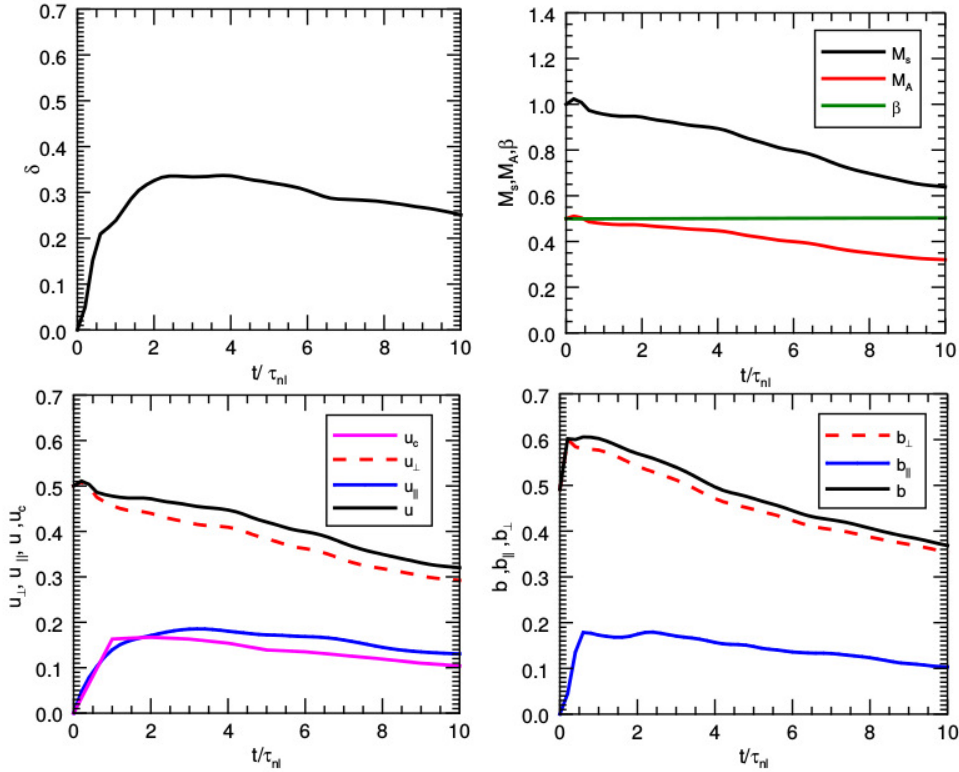


Figure 7.2: a) Evolution of the rms of density contrast δ and b) M_s, M_A and β evolution as a function of normalised time (t/τ_{nl}). c) Values of the velocity rms' components. d) Behaviour of rms of magnetic fluctuations normalised with the initial amplitude of fluctuations. As expected, after a first readjustment and relaxation of the initial configuration, fluctuations are dissipated because vortexes circulate and nonlinear interactions transfer energy to the smaller scales where dissipation dominates.

In this Section, we will focus on the properties of turbulence in our static simulations that will be used to prepare the initial condition at $t = t_0$ for contracting cases and to highlight differences between static and contracting turbulence for $t > t_0$. We recall the initial values of fluctuations, $u_{rms} = b_{rms} = 0.5$ and the for $M_s = 1$, $M_A = 0.5$ and

$\beta = 1/2$ as described in the previous Section. Our initial condition returns a 1D spectra $\mathcal{E} \sim k^2$ for $k \leq k_{max}$, with $k_{max}=4$. This implies that most of the energy is in the last excited mode k_{max} and a better estimation of the non-linear time is

$$t_{eddy}(k_{max}) = \tau_{nl} = \frac{1}{k_{max}u_{rms}} \sim 0.5 \quad (7.13)$$

in the code units. This will be our normalisation for the time in all our simulations (also for the contracting cases). In order to make comparisons between the amplitude of velocity and magnetic fluctuations, hereafter we will renormalise the magnetic field fluctuations in Alfvènic units³,

$$\mathbf{b} \rightarrow \frac{\mathbf{b}}{\sqrt{\rho_{mean}}}. \quad (7.14)$$

Fig. 7.2 shows the behaviour of mean quantities and fluctuations as a function of time (normalised to the non-linear time). After being generated from the initial conditions, density fluctuations start to decay after $\sim 2\tau_{nl}$. The value of the two Mach number decreases because the amplitude of fluctuations decreases. The velocity fluctuations in the perpendicular plane (u_x, u_y) exhibit a small increase and then, after $\sim 2\tau_{nl}$, start to decrease, while \parallel -components are generated with time due to pressure gradients and compressible effects (related to the $\nabla \cdot \mathbf{u}$ term), but remain smaller than the perpendicular components at all times. The compressible velocity is also shown in panel c) and it is of the same order of magnitude of u_{\parallel} . Magnetic fluctuations evolve as the velocity fluctuations, but they have larger amplitude. In fact, 3D MHD turbulent simulations with initially magnetic and kinetic energies at equipartition spontaneously develop a magnetic excess (or residual energy) (Grappin et al. 2016) due to dynamo effects that stretch out magnetic field's lines. The level of residual energy is given by the balance between the stretching and the effects of Alfvènic coupling.

Values for Ω_k and Ω_m are shown in Fig. 7.3. The turbulence is well developed after $\sim 4\tau_{nl}$, corresponding to the time in which the turbulent activity reaches its maximum. Magnetic enstrophy is larger than kinetic one, reflecting the different rms's value. Note that the enstrophies are relatively large at the initial time and comparable to the final time. This is due to our initial condition $\mathcal{E} \propto k^2$ for $k \leq k_{max} = 4$.

Fig. 7.4 shows the isotropised spectra of density, kinetic and magnetic energy at different times, compensated by the Kolmogorov scaling $k^{5/3}$. In both the magnetic and kinetic energy, most of the contribution comes from the perpendicular component (not shown). The density spectrum is initially generated by pressure gradients and compressible fluctu-

³In Alfvènic units velocity and magnetic field have the same units.

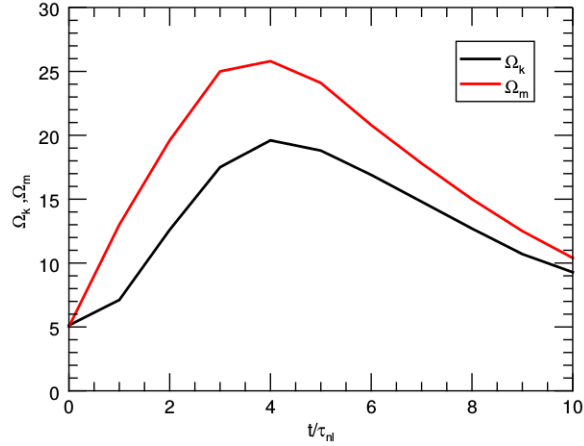


Figure 7.3: Behaviour of Ω_k and Ω_m as a function of the normalised time t/τ_{nl} . The vorticity and the current increase quickly in the fluid, reach their maximum value after $\sim 4\tau_{nl}$ and then start to decrease. The maximum value represents a good indicator for the level of turbulence development.

ations that develop from the relaxation of our out-of-equilibrium initial conditions. At the time of maximum activity ($t = 4\tau_{nl}$), the density spectrum has a small inertial range (1/4 of a decade) with slope $-5/3$, which is maintained at later time. The velocity spectrum has no clear power-law behaviour and is the steepest spectrum, possibly reflecting compressible effects. Finally, the magnetic field spectrum has a larger inertial range, about half a decade at $t = 4\tau_{nl}$, which is maintained at later times. From the magnetic spectra we can infer the value of the injection scale, which is moving to larger scale. At the final time $k_{inj} \sim 2$. We will use this value to evaluate the non-linear time at time $t_0 = 10\tau_{nl}$ when contraction is switched on. Since the fluctuations' energy is decaying due to turbulent dissipation, the cascade rate decreases with time and leads to shorter and shorter spectra. We can estimate the value of the dissipative wavenumber, k_d , which is an estimate of the dissipative scale $1/k_d$ where the transition between turbulent and viscous motion occurs, as the maximum of $k^2\mathcal{E}_k$. This is shown in panel (d).

The time evolution of the above quantities can be divided in 3 phases:

- $t < \tau_{nl}$: a short phase of relaxation of initial conditions. Compressive effects generate parallel components of fluctuations. This process generates a spectrum for the density fluctuations.
- $t \sim 2\tau_{nl}$: initialisation of turbulent cascade, triggered by the perpendicular fluctua-

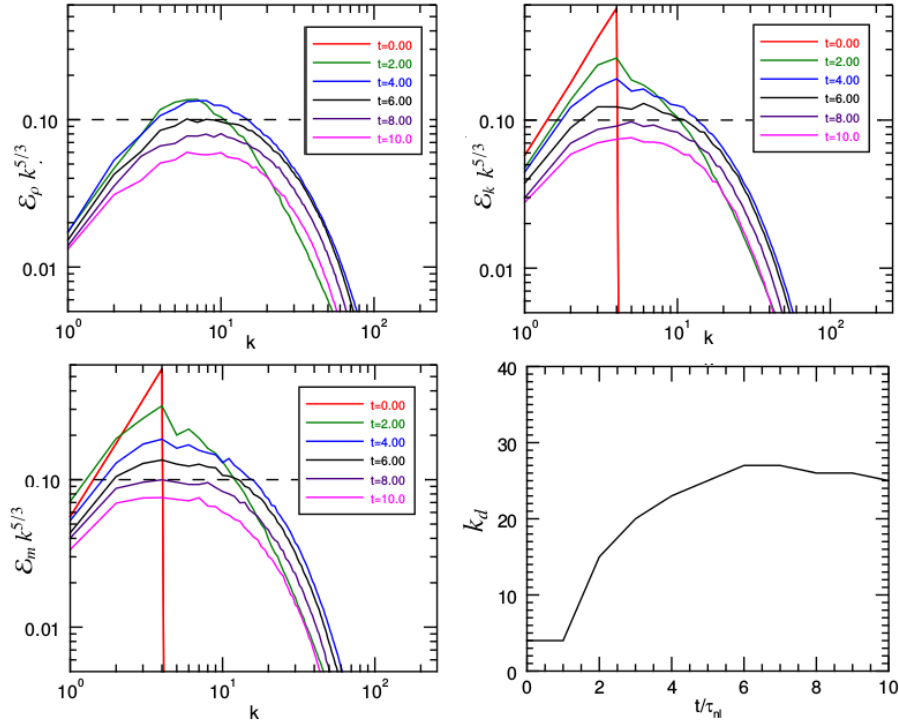


Figure 7.4: Power spectra of density \mathcal{E}_ρ (a), velocity \mathcal{E}_k (b) and magnetic \mathcal{E}_m (c) fluctuations in different t/τ_{nl} , compensated by $k^{5/3}$. The horizontal line is the reference for a $k^{5/3}$ spectrum. Fig. d) shows the values of the dissipative wavenumber k_d as a function of the normalised time. The estimate of k_d is given taking the k correspondent to the maximum value of $k^2 \mathcal{E}_k$ for each time.

tions.

- $t > \tau_{nl}$: phase of decay characterised by a decrease of all the quantities, in which the turbulence is developed and energy is dissipated. The spectra decrease but the Reynolds number is \sim constant (as we can estimate from k_d).

7.4 Contracting clouds simulations

We now consider the behaviour of turbulent fluctuations in a contracting background. As already introduced in this Chapter, the contraction changes the physical size of the cloud $L(t)$. This is modelled with a rescaling of coordinates along the magnetic field

direction with a scale factor $a = L(t)/L_0$, with $a(t)$ shown in eq. (7.2) and with an *Hubble*-like parameter $H = \dot{a}/a$ that depends on time t .

Linearising the equations from Section 7.1, the unperturbed quantities evolve following

$$\rho_0(t) = \frac{\rho_{0,0}}{a} \quad P_0(t) = \frac{P_{0,0}}{a}. \quad (7.15)$$

This behaviour is a consequence of mass conservation and the hypothesis of an isothermal EOS⁴. The equations for the perturbed quantities become

$$\frac{\partial \delta}{\partial t} + \mathbb{M} \cdot \nabla' \cdot \mathbf{u}_1 = 0, \quad (7.16)$$

$$\frac{\partial \mathbf{u}_1}{\partial t} + c_s^2 \mathbb{M} \cdot \nabla' \delta + \frac{\mathbf{B}_0 a}{4\pi \rho_{0,0}} \times (\mathbb{M} \cdot \nabla' \times \mathbf{b}_1) = -\frac{\dot{a}}{a} \mathcal{L} \cdot \mathbf{u}_1 + \zeta (\mathbb{M} \cdot \nabla')^2 \mathbf{u}_1, \quad (7.17)$$

where $\mathcal{L} = \text{diag}(0, 0, 1)$, and

$$\frac{\partial \mathbf{b}_1}{\partial t} + \mathbb{M} \cdot \nabla' \times (\mathbf{B}_0 \times \mathbf{u}_1) = -\frac{\dot{a}}{a} \mathbf{b}_1 \cdot \mathcal{T} + \eta (\mathbb{M} \cdot \nabla')^2 \mathbf{b}_1, \quad (7.18)$$

where $\mathcal{T} = \text{diag}(1, 1, 0)$.

Due to the intrinsic anisotropy of the problem, fluctuations and wavenumbers in the direction parallel or perpendicular to the direction of contraction are expected to follow different evolutions. In particular, while the parallel component of the wavenumber remains constant in time ($k_\perp = k_0$), its parallel component progressively increases as $k_\parallel = k_0/a$, implying that $|\mathbf{k}| = k(t)$. Considering separately the perpendicular and parallel directions, the equations for fluctuations in the case where contraction dominates (thus neglecting effects from sonic and Alfvénic coupling and non linear effects) become

$$\frac{\partial \delta}{\partial t} = 0 \rightarrow \delta \sim \text{const}; \quad (7.19)$$

$$\frac{\partial \mathbf{u}_\perp}{\partial t} = 0 \rightarrow u_\perp \sim \text{const}; \quad \frac{\partial \mathbf{u}_\parallel}{\partial t} = -\frac{\dot{a}}{a} \mathbf{u}_\parallel \rightarrow u_\parallel \sim a^{-1} \quad (7.20)$$

$$\frac{\partial \mathbf{b}_\perp}{\partial t} = -\frac{\dot{a}}{a} \mathbf{b}_\perp \rightarrow b_\perp \sim a^{-1}; \quad \frac{\partial \mathbf{b}_\parallel}{\partial t} = 0 \rightarrow b_\parallel \sim \text{const} \quad (7.21)$$

The behaviour of fluctuations depends also from the presence of dissipation terms (either physical or related to the numerical discretisation). We will use simulations to understand whether this effect is negligible or not compared to the effects of contraction.

⁴For a generic value of the adiabatic index γ the pressure scales as $P_0(t) = P_{0,0}/a^\gamma$.

The initial condition is a snapshot of well-developed turbulence that is decaying in a static volume, with properties that have been described in Section 7.3. In particular, we switch on the contraction of the box at $t = t_0 = 10\tau_{nl}$, allowing eddies to circulate and energy to be transferred to the small scales before the contraction begins.

Two time-scales characterise the evolution: the *non-linear* time t_{nl} related to the physical state of the turbulence (its initial value depends from the value of the turbulent fluctuations of the snapshot at $t = 10\tau_{nl}$) and the *contraction time* t_c . An estimate for the value of t_{nl} at the initial snapshot can be given by using eq. (7.4), considering the value of the rms of velocity fluctuations at $t = 10\tau_{nl}$ and the estimate for $k_{inj} = 2$ given by the spectra of Fig. 7.4, we have that

$$t_{nl} = t_{eddy}(t_0) \sim 2\tau_{nl}. \quad (7.22)$$

In this thesis we explore different values of t_c , either smaller or larger than t_{nl} :

- Simulation I: $t_c/t_{nl} = 0.5$,
- Simulation II: $t_c/t_{nl} = 5$,
- Simulation III: $t_c/t_{nl} = 50$.

During the contraction these time-scales change. In particular, the non-linear time evolves as $t_{nl}(t) = 1/k_{inj}(t)u_{rms}(t)$.

We study these simulations in two different ways. First, we make a comparison between the static case and a contracting case (simulation II), then we compare the results from simulations I, II and III. Our aim is to compare the evolution of the three different cases in a contraction that squeezes the initial box from the initial value L to $1/10L$. As a function of scale factor, this implies $a \rightarrow [1, 0.1]$. During a contraction the scale factor goes to zero, and that leads to a progressively increasing energy accumulation at the small scales given by the circulations of swirling structures created during the evolution of the system. For these reasons, our simulations fail to reach a reduction of a decade in the box size. However, information on the different behaviour in different physical situations can be found and used to elaborate some conclusions.

7.4.1 Comparison with a static case

We compare the evolution in time of our static case already introduced in Sect. 7.3 with a contracting prototype case, having $t_c/t_{nl} = 5$ (Simulation II). This simulation has been chosen because in its time evolution it displays the properties of simulation I and III.

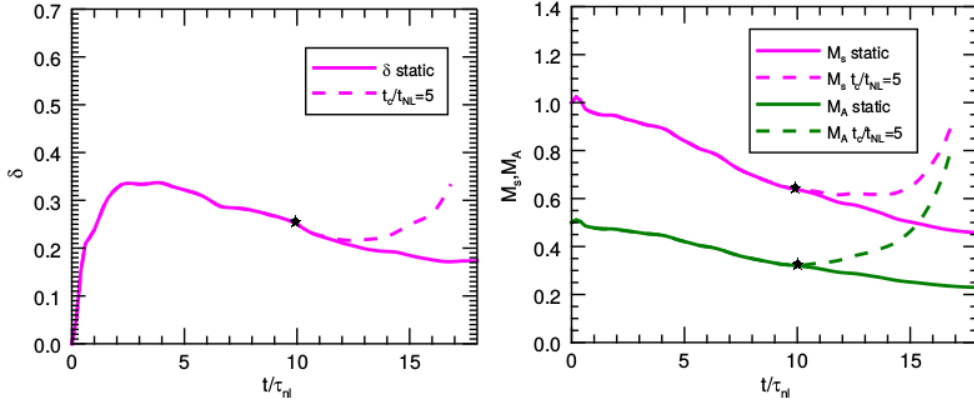


Figure 7.5: Comparison between the static case (line) and the contracting case (dashed line) with $t_c/t_{nl} = 5$ as a function of normalised time t/τ_{nl} . Left) Evolution of the rms of density contrast δ . Once the contraction is turned on ($t_0 = 10\tau_{nl}$), showed as a black star) in a first phase the effect of dissipation is balanced by the effect of contraction. After t_0 plus a few τ_{nl} fluctuations are enhanced. Right) M_s (magenta) and M_A (green) evolution as a function of normalised time.

Fig. 7.5 and show the behaviour of the rms of density contrast, of the sonic Mach M_s and of the Alfvénic Mach M_A as a function of time normalised with the non-linear time τ_{nl} . As soon as the contraction is turned on, the behaviour between the static and the contracting case is different. In particular, while the amplitudes of the density contrast and M_s decrease in the static case, in the contracting case there is a first region where they remain about constant. This region can be compared with observations of molecular clouds. The gas is isothermal, thus the value of c_s is constant and the evolution of M_s is given by the evolution of the velocity's fluctuations, that are amplified during the collapse, while for M_A both the velocity fluctuations and the Alfvén velocity change in time. The value of β , while in the static case is constant, increases proportionally to ρ_0 , thus $\beta(t) = \beta(t_0)a^{-1}$ (not shown).

Values for Ω_k and Ω_m are shown in Fig. 7.6, together with the rms of velocity and magnetic fluctuations. Both the fluctuations have a region in which their rms module is constant in time, shorter for the magnetic fluctuations, then they start to be amplified. Both the quantities present again a first phase in which they are almost constant when the contraction is turned on. They then increase fast after $\sim 14\tau_{nl}$ ($4\tau_{nl}$ after t_0). This implies that eddies' circulation increases due to the vortexes stretching. Note that the kinetic enstrophy grows faster than the magnetic one.

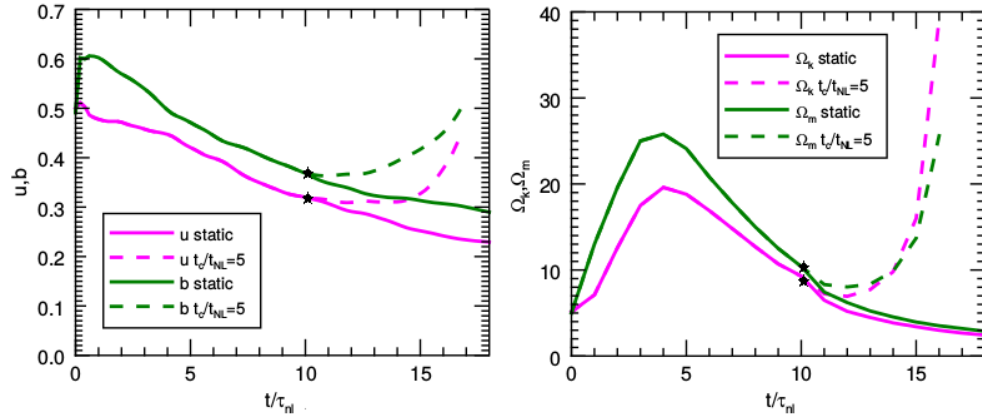


Figure 7.6: Comparison between the static case (line) and the contracting case (dashed line) with $t_c/t_{nl} = 5$ as a function of the normalised time t/τ_{nl} . The time where the contraction starts is shown with a black star. Left) Rms' behaviour of velocity (magenta) and magnetic field (green) amplitude. Both are enhanced during the contraction after a first phase where they are constant in time. Right) Behaviour of Ω_k (magenta) and Ω_m (green). The vorticity and the current increase quickly in the fluid when the contraction is turned on, after a first phase in which they are almost constant. This implies that the vorticity and the current in the system rapidly grow.

In fig. 7.7 we show the rms amplitude decomposed in \parallel and \perp components. The perpendicular component dominates the module of the rms of magnetic fluctuations, while in the velocity fluctuations the parallel component is amplified more than the perpendicular one, the magnetic fluctuations have the opposite behaviour.

Summarising, the time evolution of fluctuations in a contracting volume, when the non-linear time t_{nl} is comparable with the contracting time t_c have two different regimes:

- A phase in which velocity and density contrast fluctuations remains almost constant, indicating that the amplification due to contraction is balanced by the turbulent dissipation. The expected values of this phase can be tested with observational results.
- A phase in which all the fluctuations grow (See Section 7.4.2), indicating that the dissipation contributions can be neglected and the contribution of contraction dominates. As the amplitude of fluctuations increases, the pressure contribution can become comparable with the thermal pressure (we will come back to this in the discussion).

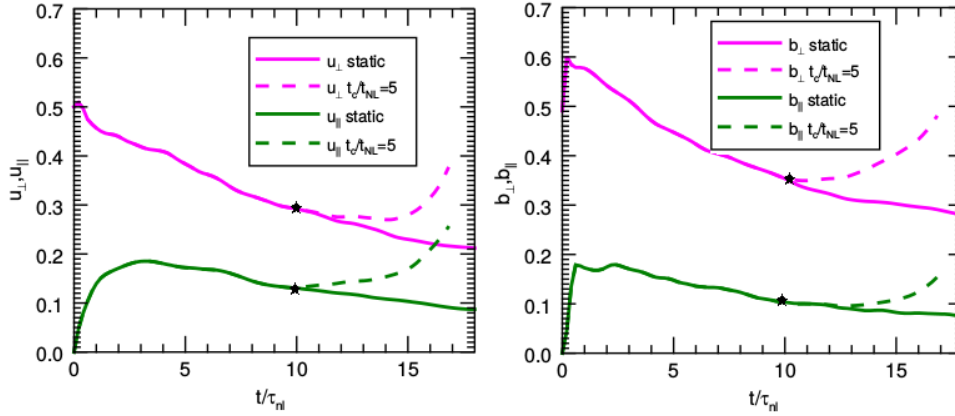


Figure 7.7: Comparison between the static case (line) and the contracting case (dashed line) with $t_c/t_{nl} = 5$ as a function of normalised time t/τ_{nl} . The time where the contraction starts is shown with a black star. Left) Evolution of the rms of the perpendicular (magenta) and parallel (green) component of velocity. Also in this case, once the contraction is turned on in a first phase the effect of dissipation is balanced by the effect of contraction. After t_0 plus a few τ_{nl} fluctuations are enhanced. Right) Evolution of the rms of the perpendicular (magenta) and the parallel (green) component of magnetic field as a function of normalised time. Both the components start to grow when the contraction begins.

7.4.2 Comparison between different t_c/t_{nl}

We now compare results from simulations I, II and III in order to understand how the same physical system behaves under different time-scales of contractions. In fact, in the case of simulation I, where $t_c < t_{nl}$, we expect the contribution due to turbulent and dissipating processes to be negligible compared with the one given by compression (the gas undergoes an *adiabatic heating* as in Robertson & Goldreich 2012), while in the case of simulation III, where $t_c > t_{nl}$, large-scale eddies have time to circulate and then dissipation terms should be dominant in the first phase of the temporal evolution. However, due to the different values of t_c , the three simulations last different times, then it is useful to compare results at the same scale-factor a . Our goal is to analyse the properties of contracting turbulence, its evolution with the scale factor a and its dependence upon the ratio between the contraction time-scale and the dissipation time-scale, thus we compare results from simulations I, II and III as function of the scale factor a in logarithmic plots. During the evolution in time, the value of the scale factor decreases from 1 to 0.1, according to the linear law of eq. (7.2), $a(t) = 1 - (t - t_0)/t_c$. It is convenient, then, to show all plots with

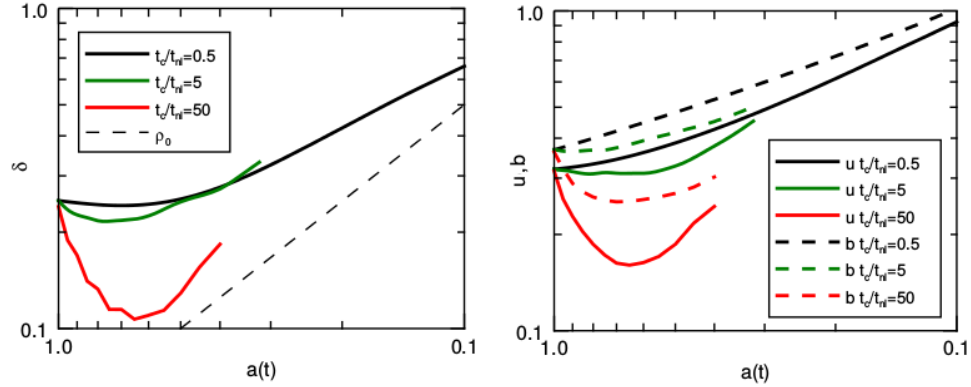


Figure 7.8: Plot of the density contrast's rms δ (left) and of the rms' behaviour of velocity and magnetic field amplitude (right) as a function of the scale factor $a(t)$ for simulations I, II and III. As a comparison for the density contrast, the value of $\rho_0(t)$ is shown as a reference. In simulation I ($t_c < t_{nl}$) dissipative effects seem to be almost negligible, while in simulation II ($t_c \sim t_{nl}$) some viscous effects are not negligible. Simulation III shows a first phase in which dissipation dominates on contraction.

an inverted scale for a , from 1 to 0.1, to follow the temporal evolution of the physical quantities. The evolution of the plasma β value, as in Section 7.4.1, is governed by the mean density ($\beta = \beta(t_0)a^{-1}$), and is then the same for all the simulations (not shown).

Fig. 7.8 shows the plot of the density contrast's rms δ , the rms' behaviour of velocity and magnetic field amplitude as a function of the scale factor $a(t)$ for simulation I, II and III. Considering eq. (7.19), the behaviour of δ in the first phases of the contraction (until $a(t) \sim 0.5$), in the case $t_c/t_{nl} = 0.5$ and $t_c/t_{nl} = 5$ is consistent with a constant time derivative (even if, in the case $t_c/t_{nl} = 5$ some dissipative effects can be noticed), while in the case $t_c/t_{nl} = 50$ dissipative effects dominates. However, in all the simulations there is a second phase where $\delta(t)$ grows with a fitted dependence $\sim a(t)^{-2/3}$. The transition between the two phases occurs at smaller scales for larger t_c/t_{nl} .

The behaviour of u_{rms} is very similar to that of δ , including the asymptotic regime with power law $a^{-2/3}$: in the case $t_c/t_{nl} = 5$ some dissipative effects can be noticed also in the first phase, while the case $t_c/t_{nl} = 50$ dissipative effects dominate until $a(t) \sim 0.5$. The behaviour of rms b is different from the other quantities. In fact, it grows $\sim a^{-1}$ for $t_c/t_{nl} = 0.5$ and $t_c/t_{nl} = 5$, but also in the case of $t_c/t_{nl} = 50$ the dissipation dominates in a shorter regime. This implies, considering also eq. (7.21), that the amplification terms due to contraction dominates.

Fig. 7.9 shows the plot of the rms of parallel and perpendicular components of ve-

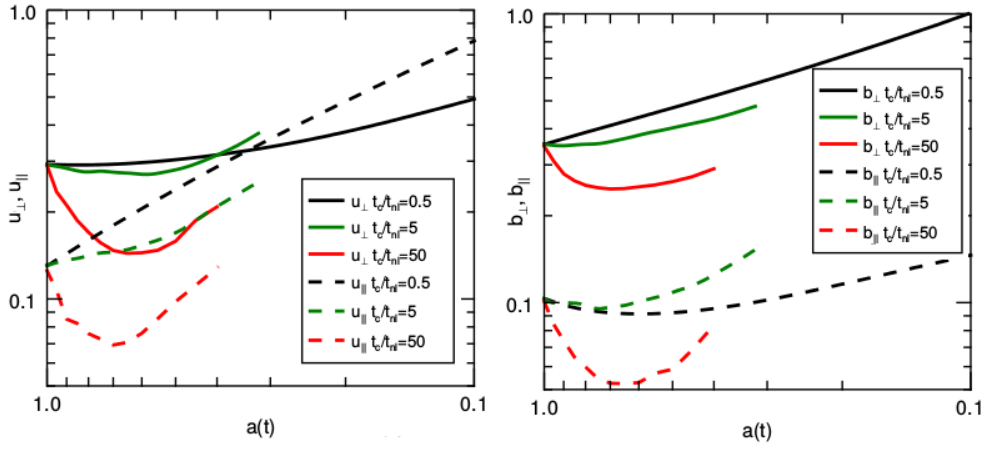


Figure 7.9: Plot of the rms of parallel (left) and perpendicular (right) components of velocity and magnetic field fluctuations as a function of the scale factor $a(t)$ for simulation I, II and III. In general, simulation I ($t_c < t_{nl}$) dissipative effects seem to be almost negligible, while in simulation II ($t_c \sim t_{nl}$) some viscous effects are not negligible. Simulation III ($t_c > t_{nl}$) shows a first phase in which dissipation dominates on contraction.

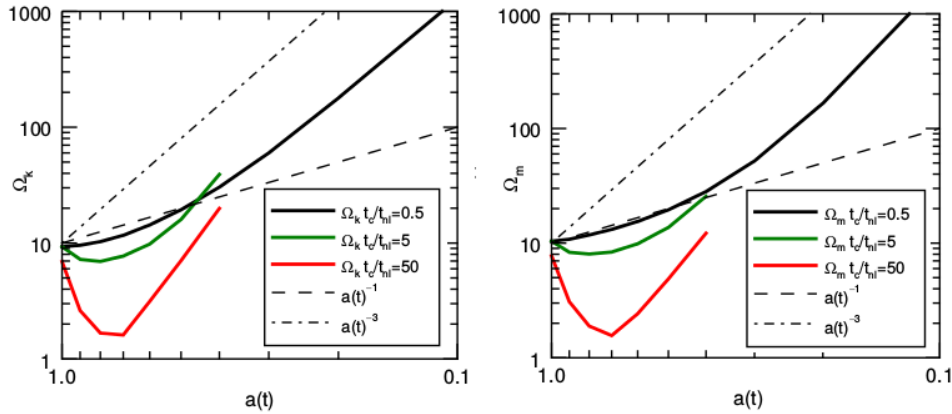


Figure 7.10: Plot of Ω_k (left) and Ω_m (right) as a function of the scale factor $a(t)$ for simulation I, II and III.

locity and magnetic field fluctuations as a function of the scale factor $a(t)$ for simulation I, II and III. Most of the contribution to the total module of the fluctuations comes from the perpendicular terms for all the values t_c/t_{nl} . An exception is the case of fast contraction, where the parallel component of velocity fluctuations grows faster ($\sim a^{-0.9}$) and

become dominant over the perpendicular one (which is constant for a first phase until $a \sim 0.5$ and then grows as $\sim a^{-1/3}$). We recall that contraction occurs along the z axis: the parallel component is made of compressible fluctuations induced by the external compression. Considering eq. (7.20), in simulation I, where $t_c < t_{nl}$ non-linear terms seem to be negligible compared with the \dot{a}/a term, while in simulation II and III dissipation effects can be noticed. In the amplitude of magnetic fluctuations the perpendicular component dominates. From eq. (7.21), in simulation I and II, spatial terms seem to be negligible compared with the \dot{a}/a term, while in simulation III in a first short phase dissipation can not be neglected.

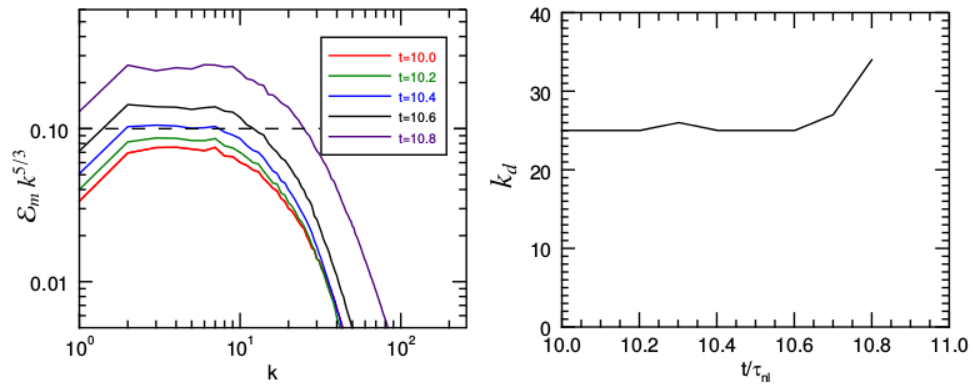


Figure 7.11: Magnetic field spectra (left) and dissipative scale (right) for the case of fast contraction $t_c/t_{nl} = 0.5$. The spectrum maintains a power-law slope of $-5/3$ while its module increases due to the amplification of fluctuations.

Fig. 7.10 shows the plot of Ω_k and Ω_m as a function of the scale factor $a(t)$ for simulation I, II and III. In simulation I ($t_c < t_{nl}$) there are two different regimes, a first one (until $a \sim 0.5$), in which both enstrophies seem grow as a^{-1} , and a second one, where they grow as a^{-3} . In simulation II and III there is a first phase (until $a \sim 0.5$) where dissipative effects are comparable with (or larger than) gravitational ones, then both Ω_k and Ω_m start to grow.

In Fig. 7.11 we show the magnetic field spectra and the dissipative scale (again estimated as the max of $k^2 \mathcal{E}_m$) for the case of fast contraction. The spectrum evolves in a self-similar way, that means that energy increases maintaining a $-5/3$ power-law. The dissipative scale, $1/k_d$, is also about constant. This phase is termed "adiabatic heating" (Robertson & Goldreich 2012) since the turbulent dissipation is driven by the "adiabatic" amplification of fluctuations caused by the fast contraction. Indeed, using the scaling

$b \sim a^{-1}$ (see Fig 7.9) one obtains a cascade rate $\epsilon = k_{inj} b_{rms}^3 \sim a^{-3}$, where we have used $k_{inj} \sim const$ as can be inferred from the spectra shown in Fig. 7.11. Only at the last time the spectrum flattens and k_d diverges, since turbulence is not able to counteract the growth of fluctuation due to the adiabatic compression and energy is accumulated at small scales due to finite numerical resolution.

7.5 Summary and discussion

Summarising, from our results the dependence from the ratio t_c/t_{nl} seems to be a key parameter to understand whether if the contraction is or is not able to amplify turbulent fluctuations. Starting from the comparison between the static and the contracting case (simulation II) shown in Section 7.4.1 (where $t_c \sim t_{nl}$), the evolution of a turbulent fluid undergoing a contraction along the mean magnetic field's axis can be divided into two different regimes: a phase where the dissipation is balanced by the contraction, and the fluctuations are supported but not enhanced, and a phase where the effect of the collapse dominates and fluctuations increase following power-laws of the scale factor. This case, ($t_c/t_{nl} = 5$) has also a region in which the value of the density contrast and the Mach numbers are almost constant. This region can be used to make comparisons between our theoretical expectations and observations.

The comparison between simulations performed in Section 7.4.2 shows that, if the contraction is slow ($t_c > t_{nl}$) turbulent and dissipative effects dominate and the turbulent velocity and magnetic field decay whereas if the contraction is fast ($t_c < t_{nl}$) the turbulent velocity and magnetic field are amplified and dissipation increases as a plain consequence of this amplification (adiabatic heating). This suggests that in a slow contraction vortexes have time to circulate and non-linear interactions can transfer energy to the small scales where it is dissipated until the dimension of the box is sufficiently small. On the other hand, in a fast contraction, the eddies are adiabatically compressed, turbulence "heats up" and turbulent quantities increase.

Fig. 7.12 shows the evolution of the rms of density contrast, magnetic and velocity fluctuations as a function of normalised time for a wide range of t_c/t_{nl} . The behaviour of all the quantities is in agreement with our deductions: for $t_c \ll t_{nl}$ dissipative effects are negligible and fluctuations are adiabatically heated, while, as t_c approaches t_{nl} , fluctuations are sustained and not enhanced for longer times. For $t_c \gg t_{nl}$ fluctuations are hardly sustained. For sufficiently large times also in this case fluctuations start to be amplified, implying that any contraction has an effect on the fluctuations if the size of the box becomes sufficiently small (or the mean density sufficiently high). The prototype

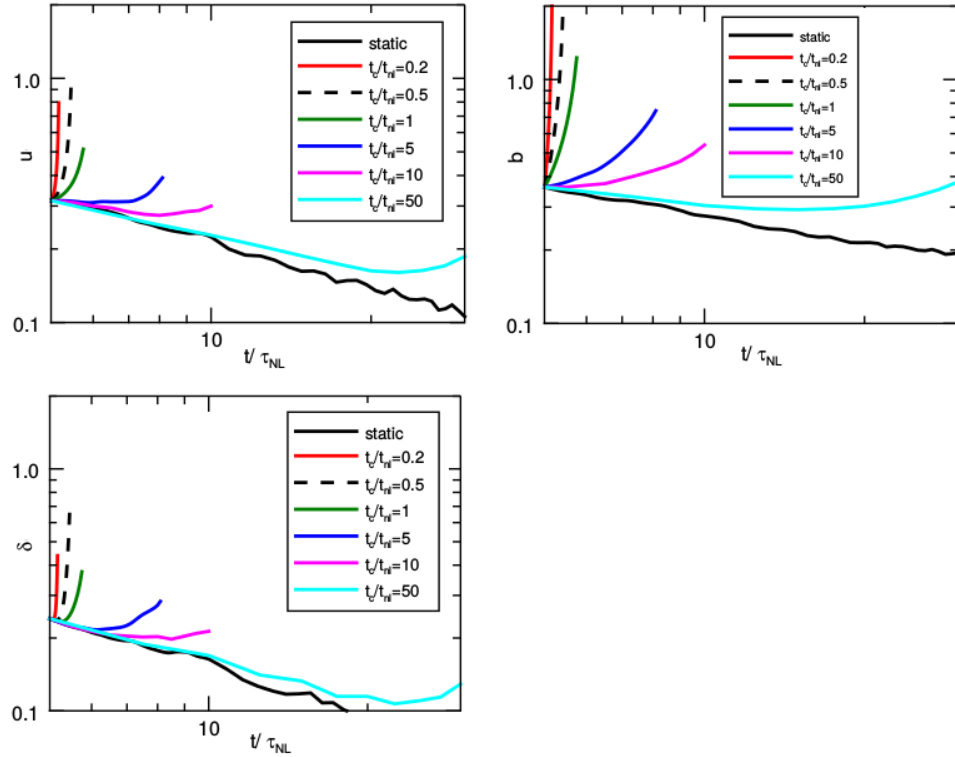


Figure 7.12: Comparison between the rms of density contrast δ (top left), magnetic b (top right) and velocity fluctuations u (bottom left) as a function of the normalised time t/τ_{nl} for different values of t_c/t_{nl} .

case $t_c/t_{nl} = 5$ represents the transition point where the contribution of contraction and dissipative effects are comparable.

A limit of our simulation is that feedback effects on the background system resulting from the enhancement of fluctuations is neglected. This effect could counteract the compression and stop the collapse. A way to estimate the magnitude of the turbulent contributions is to define an empirical relation between the mean density and the velocity fluctuations, that are both measurable quantities in molecular clouds. A *turbulent* pressure can be defined as (Lizano & Shu 1989) by $P_u = u_{rms}^2 \rho_0$.

Fig. 7.13 shows the behaviour of thermal pressure, $P_{th} = c_s^2 \rho_0$ and the turbulent pressure related to kinetic e magnetic fluctuations, $P_u = u_{rms}^2 \rho_0$ and $P_b = b_{rms}^2 \rho_0$ ⁵, for the

⁵ b is in Alfvénic units.

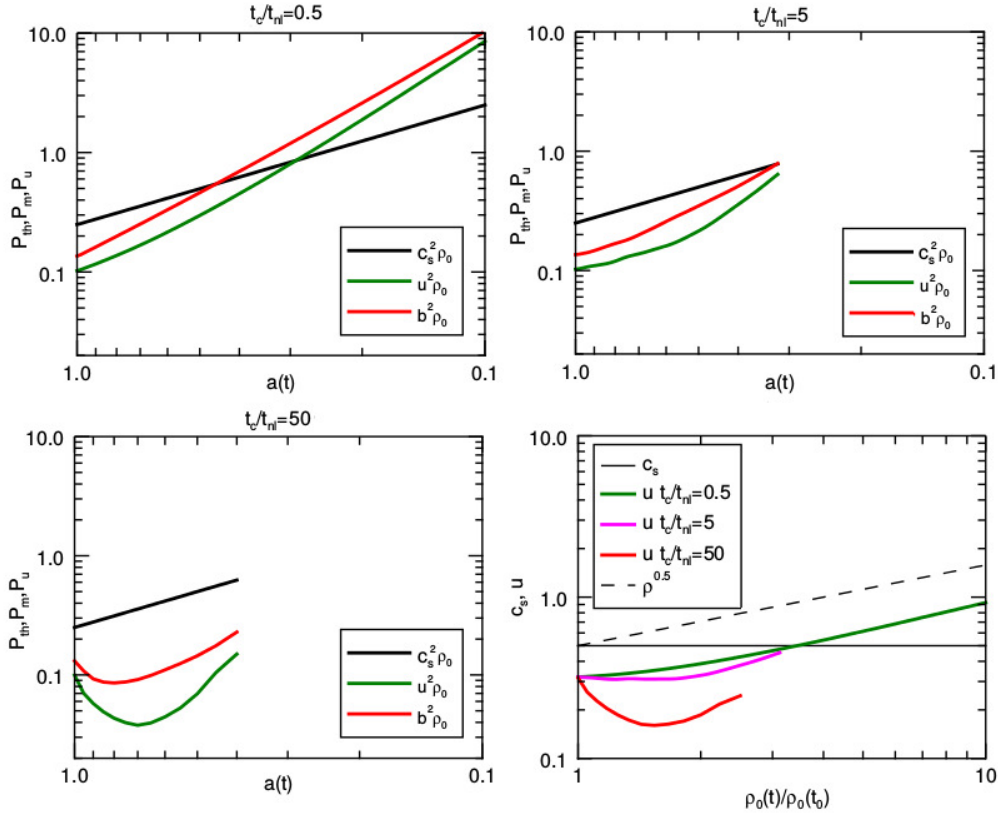


Figure 7.13: Comparison between turbulent pressure P_u (top left), P_m (top right) and thermal pressure P_{th} (bottom left) as a function of the scale factor. The fourth panel (bottom right) shows velocity fluctuations as a function of the mean density $\rho(t)/\rho_0(t_0)$

cases we examined in the previous Sections. As in the static case, there is a magnetic energy excess compared to the kinetic energy, and their ratio is approximately preserved during the contraction. In the case $t_c/t_{nl} = 0.5$, once the three pressures become comparable, turbulence becomes dynamically significant for the evolution of the fluid element. The case $t_c/t_{nl} = 5$ lasts until the value of the three pressures becomes of the same order, thus all the simulation is physically plausible. In the case $t_c/t_{nl} = 50$ our informations are not sufficiently complete to draw firm conclusion.

Fig. 7.13 also shows the behaviour of the velocity fluctuations as a function of the mean density $\rho_0(t)/\rho_0(t_0)$. The velocity fluctuations increase with density as $u_{rms} \sim \rho^{0.5}$, implying a polytropic equation of state for the turbulent pressure as in the case of

Vázquez-Semadeni et al. (1998).

A polytropic equation of state for turbulent fluctuations is also suggested in the analysis of Chapter 3, thus our simulations confirm our theoretical expectations.

8

Conclusions

In this thesis we studied the stability and contraction of molecular clouds both in the hydrodynamical and magnetohydrodynamical case, in the quasi-static and dynamical phase of evolution.

After a general introduction to the problem of star formation, in Chapter 2 we summarised the basic physics of the hydrodynamics and magnetohydrodynamics in order to provide a general background for our models. In Chapter 3 and Chapter 4 we analysed the stability of molecular clouds. Under the hypothesis that the observed filaments and cores can be represented by a sequence of hydrostatic or magnetostatic models, we studied their radial density profiles and stability properties. However, molecular clouds must contract and fragment in order to form stars. We then focused on the phase of dynamical collapse and, in particular, on the evolution of the physical properties of a fluid element that collapses in a hydrodynamic or magnetohydrodynamic regime. To achieve this, we developed a theoretical and numerical tool (see Chapter 5). In Chapter 6 we studied the growth of hydrodynamical density perturbations and the formation of sub-structures and fragments in pre-stellar cores. Finally, in Chapter 7 we analysed a magnetohydrodynamical case of the contraction of a fluid element along the direction of the mean magnetic field of the cloud.

The main conclusion obtained in this thesis are the following:

- In Chapter 3 we characterised the stability properties of filamentary clouds with a polytropic equation of state, using the polytropic exponent γ_p , related to the spatial properties of the filament. The observed radial density profiles of filamentary clouds are well reproduced by negative-index cylindrical polytropes with $1/3 \lesssim \gamma_p \lesssim 2/3$, indicating either external heating or non-thermal pressure components. The first case predicts a gas temperature at the filament's surface unrealisti-

cally high (~ 100 K). Non-thermal support, perhaps in the form of a superposition of small-amplitude Alfvén waves (for which $\gamma_p = 1/2$) provides a plausible mechanism of support. Also, the mass per unit length of negative-index polytropes is not limited, but shows a dependence on the pressure and density at the surface, if the filaments are pressure-confined by the ambient medium.

- In Chapter 4 we extended the study made in Chapter 3 to the MHD case. In fact, magnetic field seems to play an important role in determining the observable properties of filamentary clouds. We solved general equations for magnetised filamentary clouds imposing a polytropic equation of state, and assuming cylindrical symmetry together with magnetostatic equilibrium. We found that magnetic field can either support or compress the cloud (or be force-free) depending on the relative strength of the toroidal and poloidal components. Pure poloidal fields, or with small toroidal components (small pitch angle δ) give support to the cloud. This allows higher values of the envelope density than those resulting from thermal support alone. If the strength of the toroidal component increases, the effect of the field becomes very sensitive to the field strength: a small change inverts the Lorentz force, from supporting to squeezing the cloud. In the latter case, the density of the envelope is lower than the expected value in a non magnetised filament.
- In Chapter 6 we focused on the evolution of small-scale hydrodynamic perturbations in a contracting core, using the model described in Chapter 5, in order to constraint the process of fragmentation. We showed that in a contracting cloud, solenoidal and compressible perturbations grow with time, but the former faster than the latter. However, the evolution of compressible perturbations depends on their wavelength and amplitude and is controlled by the competition between several timescales: the time to reach the nonlinear stage t_{nl} , the time at which perturbations become gravitationally unstable t_{gr} , and the global collapse time scale of the background. We estimated analytically the non-linear time during a collapse, finding that, for amplitudes of velocity perturbations observed in cloud cores $t_{nl} < t_{gr}$, depending on their wavelength. Only perturbations that have initial scales comparable with the size of the core can become gravitationally unstable. The others form shock and start to dissipate their energy, establishing a competition with the “adiabatic heating” resulting from contraction. We verified our analytical results with fully three-dimensional numerical calculations performed with the hydrodynamical code ECHO. If the amplitude decay following t_{nl} suggested by the numerical calculations is representative of the dissipation in cloud core, it is unlikely that small-scale

perturbations can survive to the point of becoming self-gravitating and unstable. We suggested that fragmentation in cores is likely achieved by the growth and subsequent breakup of solenoidal, rather than compressible, small-scale perturbations. However, vortices are easily disrupted by any large-scale magnetic field.

- In Chapter 7 we performed 3D MHD simulations with 512^3 grid points, with the aim of studying numerically the temporal evolution of a magnetised and turbulent element of fluid in a contracting cloud (or a contracting core). The fluid element is contracting along the direction of the mean magnetic field, a scenario that mimics the accretion of mass on a filament. From our results the dependence from the ratio between the contraction time and the non-linear time of the system, t_c/t_{nl} , seems to be a key parameter to understand whether if the contraction is or is not able to amplify turbulent fluctuations. In fact, if the contraction is slow ($t_c > t_{nl}$) turbulent and dissipative effects dominate and the turbulent velocity and magnetic field decay whereas if the contraction is fast ($t_c < t_{nl}$) the turbulent velocity and magnetic field are amplified and dissipation increases as a plain consequence of this amplification (adiabatic heating). Defining in a phenomenological way the turbulent "pressure", we showed that, during a contraction, it quickly becomes comparable with the gas thermal pressure.

We can discuss also some general conclusion of this work. In particular, an interesting result from the MHD simulations is that the "pressure" contributions arising from the turbulent velocity can be parametrised with a polytropic equation of state, i.e. $p \sim \rho^{0.5}$. This contribution is also in agreement with the one needed to support the stability of filaments according to our quasi-static analytical models (Toci & Galli 2015a,b). Focusing on the physical properties of a fluid element in a cloud that is contracting due to its self-gravity, we can make a comparison between the hydrodynamical and magnetohydrodynamical case. Considering the behaviour of the density contrast, the velocity fluctuations and the kinetic enstrophy in contracting MHD simulations in the most representative case, there is a first phase where both these quantities remains constant in time, suggesting the lack of a preferential mechanism of structure formation. Kinetic enstrophy starts to grow earlier and faster than density and velocity fluctuations, suggesting that, as in the hydrodynamical case (Toci et al. 2017), solenoidal modes grow at a faster rate than compressible modes, and may eventually promote fragmentation through the formation of vortical structures.

8.1 Future perspectives

Part of the research showed in this thesis has not been published. With a view to a future paper, there are several improvement that we can make in order to extend our analysis.

As regard the analytical models, in the hydrodynamical case we can extend our analysis also to values of the polytropic index that we first excluded. They represent particular solutions (i.e. magnetic dominated configurations) that can represent observational cases. We would also like to compare our theoretical expectations with the new ALMA observations of density profiles. An analytical analysis of the temperature profile would allow us to make comparison also with observed temperature profiles. The new ALMA polarimetric observations will give new constrain to the direction and strength of magnetic fields in molecular clouds and cores, and will allow us to improve our magnetohydrodynamical models.

The study on the growth of hydrodynamical gravitational collapse showed that the growth and subsequent breakup of solenoidal, rather than compressible perturbations could lead to multiple fragmentations. This aspect should be explored in future works, considering the different mechanism of structure's fragmentation but also that vortices are easily disrupted by large-scale magnetic field. It would be also desirable to improve the capabilities of submillimetre interferometers like ALMA to constrain the level of fragmentation in starless cores.

Finally, considering the MHD simulations we performed, our model is highly idealised both in the geometry of the system both in the superimposed contraction. Despite this, we are not able to cover contractions of $1/10 L_0$ and a first improvement should be in this direction. Two important physical limits of our simulations are the absence of a *feedback* effect due to fluctuations on the contraction, and the absence of a *Poisson solver* in order to follow the evolution of fluctuations once they become gravitationally unstable. An analytical analysis, as in the HD case, will help us to understand the different regions where these contribution are important. An extension of this work could be the study of different metrics, related to different scale-law, and different magnetic configurations. Another important parameter that characterize turbulence in MC is the fluctuations' Mach number, thus new simulations with supersonic Mach numbers will improve our analysis.

A

Appendix

A.1 Appendix A: physical characteristics of a plasma

A characteristic of a plasma is the *quasi neutrality*. Charged particles have long-range electromagnetic interactions that are dominant versus the Coulomb interactions between neighbours, the kinetic energy being greater than the potential energy between two neighbouring particles. The electrostatic interaction between two charged particles is shielded due to the presence of other particles with opposite charge. A negative charge will attract positive charges and that will lead to a screening at great distances, making the electrostatic potential in a plasma with the same number of protons and electrons $n_i = n_e = n$ and the same temperatures $T_i = T_e = T$ equal to:

$$\Phi(r) = \frac{e}{r} \exp\left(-\frac{r}{\lambda_D}\right), \quad (\text{A.1})$$

where e is the electric charge of the particle. The effective potential reduces to the Coulomb form $\Phi \rightarrow e/r$ for $r \rightarrow 0$ and it becomes negligible when $r \rightarrow \infty$. The characteristic length where a particle is fully shielded is given by the Debye length λ_D ,

$$\lambda_D = \left(\frac{k_b T}{4\pi n e^2}\right)^{\frac{1}{2}} \sim 6.9 T^{1/2} n^{-1/2}, \quad (\text{A.2})$$

where k_b is the Boltzmann constant. The Debye length also defines an effective range for collisions, due to the fact that interactions between particles occur with a shielded Coulomb potential. The hypothesis of charge screening can be applied only if the density is sufficiently large so that there are many particles in a volume defined by the Debye

length (or, equivalent, if the mean distance between particles, $\langle d \rangle \sim n^{-1/3}$ is much smaller than the Debye length). Mathematically, if the number of particles is $\sim n\lambda_D^3$, for a charged fluid being a plasma (thus quasi-neutral)

$$n\lambda_D^3 \gg 1 \quad (\text{A.3})$$

and

$$\lambda_D \ll L, \quad (\text{A.4})$$

where L is the characteristic scale of the plasma over with macroscopic quantities such as ρ or T vary. These two conditions are usually incorporated into the plasma definition.

An important characteristic frequency in a plasma is the collision frequency. In fluids collisions are strong and binary. A binary collision between particles is an interaction occurring when the distance between particles decreases below a certain characteristic scale b , given for example by the distance at which the kinetic energy of relative motion equals the electrostatic Coulomb potential energy. The collisional cross-section is $\sigma_c = \pi b^2$ and the collision frequency is $\nu_c = n\sigma_c v_T$. This is an important difference between plasmas and fluids: in plasma collisions are weak, many-body interactions. The cumulative effect of all the weak interactions is to reduce the collision time by a factor $\sim 8\ln(\lambda_D/b_0)$ (also known as the Coulomb logarithm), where b_0 is the interaction distance corresponding to a $\pi/2$ deflection, with respect to the one of neutral gas.

Collisions are the way through which a plasma thermalizes (particle populations with different temperatures reach thermal equilibrium). In a collision, energy may be transferred from the particle of higher energy to the lower energy one. Consider a plasma of electrons and ions both out of thermodynamic equilibrium but with similar energies. Collisions that lead to equilibrium among particles of the same species are on a different time-scale compared to that required for thermal equilibrium across species. For an electron-proton plasma electron-proton thermalization requires longer times than both electron-electron and proton-proton thermalization, thus this plasma may have electrons and protons at different temperatures. Collision frequencies are associated with *disordered* motions in a plasma.

Another fundamental plasma frequency is associated with the plasma shielding. The root mean square (rms) or thermal speed of particles with mass m is $v_T = \sqrt{3k_b T/m}$. Using also the Debye length this sets a characteristic timescale $\tau_p = \lambda_D/v_T$. The plasma frequency is proportional to $1/\tau_p$, and defined as

$$\omega_p = \sqrt{\frac{4\pi n e^2}{m}}. \quad (\text{A.5})$$

In a plasma composed of ions and electrons, there will be a plasma frequency associated with electrons, ω_{pe} , and one with the protons ω_{pi} . For electrons, in cgs-Gaussian units $\omega_{pe} \sim 5.6 \times 10^4 n_e^{1/2}$. In this plasma, if the electrons are displaced by a general amount x the resulting electric field is $E = 4\pi n_e e_0 x$ and the equation of motion for a displaced electron corresponds to the dynamics of an harmonic oscillator with frequency ω_{pe} . Charge separation in a plasma then leads to restoring forces that tend to produce oscillations in electrons. This is an *ordered* motion (as opposed to random thermal motions). The plasma frequency therefore poses an upper limit to the frequencies of dynamic motions in the plasma satisfying quasi-neutrality because only disturbance with frequency comparable or larger than such value will produce an appreciable charge separation in plasma, otherwise fast electric oscillations will cancel the effect.

The neutrality condition does not imply that local material sources for electromagnetic fields could be ignored. A plasma may be electrically neutral on average, yet still have electric currents due to electrons drift relative to ions. Such currents can generate magnetic fields \mathbf{B} . Particles of charge q and mass m in a magnetic field do not follow straight line trajectories but gyrate around the field lines with a non-relativistic gyro-frequency called *cyclotron* or *Larmor frequency*,

$$\omega_L = \frac{qB}{mc}. \quad (\text{A.6})$$

For a proton the gyro-frequency is $\sim 0.1s^{-1}$ in a magnetic field with strength $B = 10^{-5}$ Gauss, a typical value for interstellar clouds. The gyro-radius $r_L = v_{\perp}/\omega_L$ is small compared to macroscopic scales for almost all the values of the velocity. In presence of a magnetic field charged particles cling to the field lines until they are knocked off by collisions. This makes the motion of charged particles more coherent. This leads to the fact that even in a dilute plasma, the macroscopic behaviour of the particle is more similar to a fluid than to a collection of independent moving particles if the plasma is sufficiently magnetised. The ISM is a classical plasma. Relativistic effects become important if the thermal energy is $k_b T \gg mc^2$, then for an electron $T > 6 \times 10^9 K$.

A.2 Appendix B: ECHO code numerical scheme

As already anticipated in Chapter 5.3, the numerical solution of the MHD equations system requires a particular numerical scheme. The one used in the code is based on the Godunov scheme (Godunov 1959), projected for fluid dynamics and extended for MHD

using the UCT method¹. The code ECHO can solve any MHD-like set of equations that can be represented as a duple of coupled sub-systems, the former containing the fluid part in which the spatial operator are in the form of divergence (an application of Gauss theorem) plus source terms and the latter, specific for the magnetic field, that contains the induction equation in curl form, with the condition of divergence-free (an application of Stokes theorem),

$$\frac{\partial \mathbf{u}(\mathbf{w})}{\partial t} + \nabla \cdot \mathbf{f}(\mathbf{w}) = 0, \quad (\text{A.7})$$

where \mathbf{f} is the fluid flux, $\mathbf{w} = [\mathbf{u}, \mathbf{B}]^T$ is the set of conserved variables and

$$\frac{\partial \mathbf{B}(\mathbf{w})}{\partial t} + \nabla \times \mathbf{E}(\mathbf{w}) = 0, \quad (\text{A.8})$$

where \mathbf{E} is the magnetic flux. In Appendix A.3 is described the Gudonov explicit scheme and in Appendix A.4 its extension, the UCT (Upwind Constrained Transport) method (Londrillo & del Zanna 2004).

The ECHO scheme

The steps needed to evolve the system are described in Del Zanna et al. (2007) and Landi et al. (2008). Here we will give a brief summary of the procedures.

- In order to evaluate the spatial derivatives of the fluxes along all the directions, we refer as u_i to indicate any scalar component of the discretised variables (\mathbf{u}, \mathbf{B}) along a general direction x_i , with Δx the grid dimension and by $f_i = f(u_i)$ a corresponding flux component.
- Every primitive (or conservative) variable u_i in eq. (A.28) is reconstructed (applying the 1D reconstruction procedure, REC in the code) in the correspondent cell interface $x_{i+1/2}$ using a left-biased (L) or right-biased (R) interpolation, i.e

$$u_i \rightarrow [u^L, u^R]_{i+1/2}. \quad (\text{A.9})$$

As a consequence, any flux component $f(u)$ is a two-sided interpolated function,

$$f_i = f(u_{i+1/2}) \rightarrow [f^L, f^R]_{i+1/2}. \quad (\text{A.10})$$

¹Upwind schemes are a class of methods that solve partial hyperbolic equations using finite differences. For any grid point i in the numeric domain there are only two directions associated with it, left and right. An asymmetry of points on the left part compared to the right part is an *upwind* method, the opposite is *downwind*.

The shock-capturing feature requires in one-sided interpolation schemes non oscillatory properties for allowing the monotonicity of functions. In the ECHO code a compact upwind REC has been implemented that avoids Gibbs oscillations and guarantees monotonicity (see [Del Zanna et al. 2007](#) for details). Different orders of explicit WENO (Weighted Essentially Non-Oscillatory) schemes are implemented, too. Simulations in this work are performed by employing WENO5 (Weighted-ENO) fifth order scheme for the spatial derivatives coupled with a third order Runge-Kutta time integration. The solenoidal constraint for the magnetic field is enforced through the Upwind Constrained Transport (UCT) method (See [Appendix A.4](#)).

- After the reconstruction phase, the two values function $[f^L, f^R]$ are combined in an unique continue value of the upwind flux with an approximate Riemann solver:

$$f(u^L, u^R) = \frac{1}{\alpha_+ + \alpha_-} [\alpha_+ f^L + \alpha_- f^R - \alpha_+ \alpha_- (\alpha_+ u^R - \alpha_- u^L)], \quad (\text{A.11})$$

where $\alpha_+ = \max[\alpha_+^R, \alpha_+^L]$, $\alpha_- = \max[\alpha_-^R, \alpha_-^L]$, $\alpha = |v_p| + \lambda$, v_p is the plasma velocity and λ is the local mean of the maximum eigenvalue (wave characteristic velocity) of the Jacobian flux and \pm is the sign of α . In MHD cases $\lambda = V_f$, where V_f is the fast magnetosonic speed.

- The formal order of approximation r requires that the term $(u^R - u^L)$ in the calculation of the flux is a diffusive or dispersive term order $O(\Delta x)^r$ in the smooth region. In almost all the current simulations the REC order is $r=5$. The order r for the interpolation of u is related to the approximation order for the flux function on the cell interfaces,

$$f_{i+1/2} = f(x_{i+1/2}) + O(\Delta x)^r, \quad (\text{A.12})$$

but the difference between the two fluxes is only a second-order approximation of the flux derivative, independently on the chosen r ,

$$\frac{f_{i+1/2} - f_{i-1/2}}{\Delta x} = f'_i + O(\Delta x)^2. \quad (\text{A.13})$$

To obtain high-order precision for the fluxes derivative an additional high order reconstruction procedure, named DER, is required. It allows to reach a high order approximation from the point value quantities calculated at the same intercell locations, recovering a numerical derivative function $f_{i+1/2} \rightarrow \hat{f}_{i+1/2}$ having the

requested properties,

$$\frac{\hat{f}_{i+1/2} - \hat{f}_{i-1/2}}{\Delta x} = f'_i + O(\Delta x)^{r+1}. \quad (\text{A.14})$$

Simulations in this work are performed by employing a sixth order DER procedure.

- The same procedure can be applied to the induction eq. (A.8), where a staggered discretisation will be used, with a specific 2D Riemann solver is needed in order to take into account the specific curl form of the differential operator and the conservation laws (see Appendix A.4). Values at the interface of $b_{i+1/2} \rightarrow [b^L, b^R]_{i+1/2, k+1/2}$ and its relative flux $\hat{f}(b_{i+1/2}) = \hat{E}_{i+1/2, k} \rightarrow [\hat{E}^L, \hat{E}^R]_{i+1/2, k+1/2}$ are reconstructed at the interface. The two-value flux function is then combined, using a Riemann solver as in eq. (A.11), to have a unique value. A sixth-order interpolation procedure (INT) is required to approximate magnetic field components, defined at the interfaces of cells S (again, see Del Zanna et al. 2007).
- Runge-Kutta time-stepping can be finally applied, and the whole procedure for updating the set of conservative variables \mathbf{w} has to be repeated for each sub-cycle. As in all explicit schemes, the timestep Δt is limited by the CFL (Courant-Friedrichs-Lewy) condition, $0 < CFL < 1$ (see eq A.27),

$$\Delta t = \frac{CFL}{\min\left[\frac{\Delta}{\alpha}\right]}, \quad (\text{A.15})$$

where $\Delta = \min[\Delta x, \Delta y, \Delta z]$ and α is the maximum of the eigenvalues in the j direction α_j ($j = x, y, z$).

Temporal integration: The Runge-Kutta method

Third order Runge-Kutta (R-K) method for integrating in time allows to find for a generic time function $u(t)$, known at t , the temporal evolution $u(t + \Delta t)$ with a precision equal to a third order Taylor-expansion using only the first order derivative of $u(t)$. Three steps are in use, with slightly different coefficients compared with the standard R-K method,²

$$u_1 = u_0 + \frac{8}{15}\Delta t f(u_0); \quad u_0 = u(t), \quad (\text{A.16})$$

$$u_2 = u_1 - \frac{17}{60}\Delta t f(u_0) + \frac{5}{12}\Delta t f(u_1); \quad (\text{A.17})$$

²Those value are chosen to simplify the code algorithm.

$$u_3 = u_2 - \frac{5}{12}\Delta t f(u_1) + \frac{3}{4}\Delta t f(u_2); \quad u_3 = u(t + \Delta t). \quad (\text{A.18})$$

As in all the explicit integration methods, R-K method uses a variable Δt , in order to have a more stable code. The choice of the integration step depends on the field propagation velocity in the numerical grid, in particular it has to be shorter than the time required for the field propagation. If α is the maximum velocity propagation and Δs is the smaller grid step, then the latter condition is

$$|\alpha| \frac{\Delta t}{\Delta s} < 1, \quad (\text{A.19})$$

corresponding to the Courant-Friedrichs-Lewy criterion. In the case of this thesis, the plasma is viscous and resistive, thus both the related diffusion coefficients have to be considered. Condition for Δt is then

$$\Delta t < \Delta t_{min} = \min \left[\frac{\Delta s}{|\alpha|}, \frac{\Delta s^2}{\eta}, \frac{\Delta s^2}{\zeta} \right], \quad (\text{A.20})$$

where ζ and η are the kinematic and magnetic viscosity. For increasing the stability of the code, again $\Delta t = CFL * \Delta t_{min}$.

Boundary Conditions

ECHO code allows the following boundary conditions:

- Open boundary conditions
- Periodic boundary conditions $g(x \pm L) = g(x)$; if n_{GC} are the points requested, out of the numerical domain, for the evaluation of REC, DER and INT at the required order (called Ghost Cells), the periodic boundary condition is

$$g_{i_0-1} = g_{n_0-1}; \quad g_{n_0-1} = g_{i_0+1}; \quad i = 1, \dots, n_{GC}. \quad (\text{A.21})$$

$i_0 = 1/2$, or $i_0 = 1$ and $n_0 = n + 1/2$ or $n_0 = n$ (n is the total number of points in a direction) according to the procedure. This condition is the one used in this work.

- boundary conditions with reflection
- Third order extrapolation: fields are reconstructed out of the numerical domain with a one-side third order scheme.

MPI parallelisation and optimisations

For any temporal step ECHO code have to evaluate first, second, mixed derivatives for all the physical fields ($\mathbf{u}, \mathbf{B}, \rho, T$). Most of the computational time is employed for the spatial derivatives, that require many operations. To decrease the duration of simulations processes can be parallelised: the process that works on all the numerical grid is splitted in n_p processes working on a grid slice (or cube). The processes have to share common informations like the integration time step. A physical CPU (with its own RAM memory) corresponds to any process. The number of processes n_p can be chosen by the user.

The ECHO code has been parallelised using the MPI protocol (Message Passing Interface) and has been used on local clusters in Arcetri and on the CINECA supercomputer MARCONI. We will shortly describe the parallelisation algorithm. Only the spatial derivatives have to take into account also informations from neighbour points, while other parts of the code are local (only the variables values in the points are required). In addition, the evaluation of a derivative along a general i direction requires only the i -neighbours informations³, thus the spatial derivative in a direction is local in the other two.

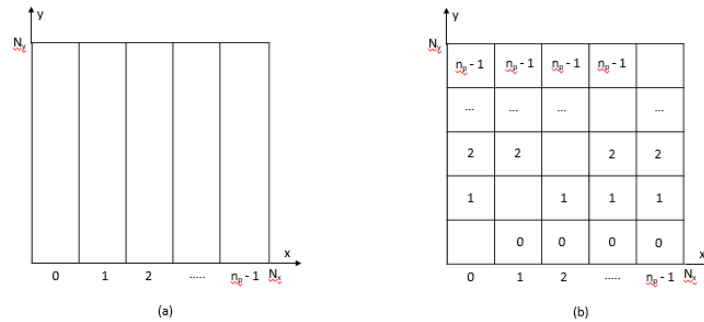


Figure A.1: Parallelisation strategy: (a) grid division along the x axis, (b) swap procedure.

The numerical grid has been divided into n_p slices along a direction (hereafter, the x direction, see Fig. (A.1)). The y and the z derivatives can be evaluated locally, while for the parallelisation direction a *swap* procedure is needed (see Fig. (A.1)). For simplicity let us consider the 2-D case as example: the grid is divided also on the y direction, thus there are n_p vectors v_{xy} with dimension $m_x \times n_y$, where $m_x = n_x/n_p$. A new storage vector v_{yx} is generated, with dimension $n_x \times m_y$, where $m_y = n_y/n_p$ and the derivatives along

³This is a consequence of the finite explicit method of derivatives implied in the code. For other kinds of schemes it could be required the knowledge of the fields in all the points

the x direction are calculated. During the construction of the storage vector all the CPUs communicate, and this process require time (the more CPUs, the longer the process). A limitation on the CPUs number comes from the grid point numbers for each process. In general, $n_{points}/n_p = 4$ is a good compromise.

A.3 Appendix C: Gudonov explicit scheme

The starting point is to discretise the equations. An explicit Godunov scheme is a conservative numerical scheme that solves partial differential equations. It is a conservative finite-volume method that solves exact (or approximate) Riemann problems at any inter-cell boundary. The original form is first order accurate in both space and time. Defining a fixed volume \bar{V} and beeing \bar{S} its surface, eq. (A.7) for the fluid part can be written as

$$\frac{d}{dt} \int_{\bar{V}} \mathbf{u} dV + \oint_{\bar{S}} \mathbf{f}_i n_i dS = 0, \quad (\text{A.22})$$

where n_i is the normal versor to the generic surface S . The value of the conserved variables \mathbf{u} is supposed to be known in the cell center i in the discretisation grid. Considering a 1-D domain of integration divided in n equal cells, spaced with Δx , as reported in Fig A.2, the volume \hat{V} corresponds to the interval x which goes between $x_{i-1/2}$ and $x_{i+1/2}$. Eq. (A.22) becomes

$$\frac{d}{dt} \int_{x_{i-1/2}}^{x_{i+1/2}} \mathbf{u} d\xi + \hat{\mathbf{f}}_{x_{i+1/2}} - \hat{\mathbf{f}}_{x_{i-1/2}} = 0. \quad (\text{A.23})$$

If we define the mean value of \mathbf{u} in the interval x as \mathbf{u}_i^4 , the temporal integration in an interval $\Delta t = t^{n+1} - t^n$ of the last equation is

$$\mathbf{u}_i^{n+1} = \mathbf{u}_i^n \frac{1}{\Delta x} \int_{t^n}^{t^{n+1}} (\hat{\mathbf{f}}_{x_{i+1/2}} - \hat{\mathbf{f}}_{x_{i-1/2}}) d\tau. \quad (\text{A.24})$$

If the time integral is approximated as $\sim \Delta t (\hat{\mathbf{f}}_{x_{i+1/2}}^n - \hat{\mathbf{f}}_{x_{i-1/2}}^n)$, then we have

$$\frac{\mathbf{u}_i^{n+1} - \mathbf{u}_i^n}{\Delta t} + \frac{\hat{\mathbf{f}}_{x_{i+1/2}}^n - \hat{\mathbf{f}}_{x_{i-1/2}}^n}{\Delta x} = 0, \quad (\text{A.25})$$

where i is the index for the spatial level and n is the temporal level. $\hat{\mathbf{f}}_{x_{i\pm 1/2}}^n$ represent the flux numerical vector of the conserved variables, evaluated in the interfaces between i and

⁴The mean value is defined as $\hat{\mathbf{u}} = \frac{1}{\Delta x} \int_{x_{i-1/2}}^{x_{i+1/2}} \mathbf{u} d\xi$

$i \pm 1$ or $i - 1$ and i at the temporal level n (see Fig. (A.3)). How to evaluate the numerical

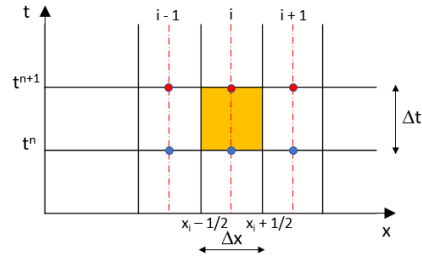


Figure A.2: Numerical grid.

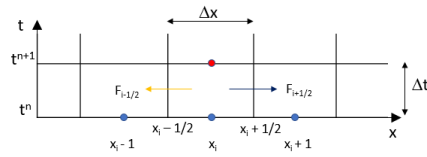


Figure A.3: Flux representation on the discretisation grid.

flux vector depends from the numerical scheme in use. Godunov proposed a method that uses the Riemann's problem solution⁵. If the mean values of the primitive variables are known in every spatial cells (\mathbf{u}_i^n , with $n = 1, \dots, n_{cells}$) at a certain time n , it is possible to construct a function that is constant in steps $\mathbf{u}_k(x, t^n)$ that contains the former values. This solution is discontinue in the interfaces between two close cells.

Let us consider this solution as an initial condition for the problem. After some time, there will be n_{cells} Riemann problems. In any interface a set of waves will be generated (as many as the equations). The solution of the Riemann problem is to find an unique set for the conserved values at any interface. This values will be conserved until the waves generated in an interface reach the next one. In order to avoid this phenomenon the integration time interval has to be, if $\alpha_{max}(i)$ is the largest among all the propagation

⁵ The Riemann problem studies the temporal evolution of a discontinuity that is in between two different fluids. Those fluids have, in general, different thermodynamic and kinematic values. The initial discontinuity generates, in the Eulerian case, two families of waves that propagates in opposite directions and a contact discontinuity.

velocities for every i -Riemann problem,

$$\Delta t(i) \leq \frac{\Delta x}{\alpha_{max}(i)}. \quad (\text{A.26})$$

This condition gives a constrain on the temporal interval,

$$\Delta t \leq \frac{\min[\Delta x]}{\max[\alpha_{max}(i)]}. \quad (\text{A.27})$$

Thus, defining $CFL = \alpha_{max}\Delta t/\Delta x$, it has to be ≤ 1 . The primitive variables will have the values evaluated in the interfaces $i \pm 1/2$, and they will be used to estimate the values of the vectors $\hat{\mathbf{f}}_{x_{i\pm 1/2}}^n$. Using eq. (A.25) the value of the conserved variables in the new time \mathbf{u}_i^{n+1} for all the integration cells can be obtained. The numerical scheme has to take into account that the step-defined solution $\mathbf{u}_k(x, t^n)$ cannot be unique. In that case, the chosen solution is the one that solves simultaneously all the Riemann problems of the Euler system for entropy.

We can then define the solving algorithm, that is applied until the last integration time:

- Reconstruction: in each cell, starting from the \mathbf{u}_i^n , the step defined function $\mathbf{u}_k(x, t^n)$ is built.
- Evolution: Riemann problems are solved in the interfaces, imposing the condition from eq (A.27). The function $\mathbf{u}_k(x, t^{n+1})$ is obtained; from that the values in the interfaces.
- Mean values: Using eq. (A.25) the values in the centres of the cells are obtained, \mathbf{u}_i^{n+1} in the new temporal instant.

A method that allows to evaluate the value of solutions in the new time starting from the known solution at the previous time is called *explicit method*.

A.4 Appendix D: Upwind Constrained Transport method

An extension of conservative schemes like Godunov for applying to MHD equations requires a modification in order to represent and solve Riemann's problems for the magnetic field's solenoidal structure. The Constrained Transport (CT) method allows to staggered discretize vectorial magnetic and electric fields in the induction equation, with the constrain $[\nabla \cdot \mathbf{B}]_{num} = 0$ for the initial condition that is conserved in time. A method Godunov-like with the CT extension is called UCT method (Londrillo & del Zanna 2004).

This is known to be more efficient than finite volume methods for high order treatments of multi-dimensional problems because only 1D reconstruction algorithms are used.

Let r be the order of spatial accuracy requested for the scheme. In this method the finite 3-D computing domain Ω is divided in Cartesian cells C , that have volume V , size h_i , $i = x, y, z$ and faces made by oriented surface elements S_i^\pm , where \pm indicates the direction of the surface's versors (normal to direction i). For each face S_i , its oriented side L_j^\pm, L_k^\pm with $j, k \neq i$. The code implies semi-finite volumes only for the spatial integration, the temporal dependence will be evaluated using Runge-Kutta integration schemes.

A conservative discretisation of eq. (A.7) can be realised integrating any scalar equation on the volume element V of any cell C and using Gauss theorem,

$$\frac{d}{dt} \hat{\mathbf{u}}(t) + \sum_i \frac{1}{h_i} (\hat{\mathbf{f}}_i^+ - \hat{\mathbf{f}}_i^-) = 0, \quad (\text{A.28})$$

where

$$\hat{\mathbf{u}}(t) = \frac{1}{|V|} \int_V \mathbf{u}(\mathbf{x}, t) dV \quad \text{and} \quad \hat{\mathbf{f}}_i^\pm = \frac{1}{|S_i^\pm|} \int_{S_i^\pm} \mathbf{f}_i dS \quad (\text{A.29})$$

are the mean on the volume of each scalar component u^l on the cell C and the mean of the flux on the faces of the cell S_i^\pm . Note that the fluxes are exact values of the parallel coordinate i , and their differences are the mean flux derivatives.

For the system (A.8), the CT method that preserves the original property, that is the asymmetry of the vector, is realised with a surface integration on a cell face followed by the use of Stokes theorem. It gives

$$\frac{d}{dt} \hat{b}_i(t) + \sum_{j,k} \epsilon_{i,j,k} \frac{1}{h_j} (\hat{E}_k^+ - \hat{E}_k^-) = 0, \quad (\text{A.30})$$

where $\epsilon_{i,j,k}$ is the Levi-Civita tensor and \pm is the versor of the j -direction faces and

$$\hat{b}_i(t) = \frac{1}{|S_i|} \int_{S_i} B_i(\mathbf{x}, t) dS \quad \text{and} \quad \hat{E}_k^\pm = \frac{1}{|L_k^\pm|} \int_{L_k^\pm} \mathbf{E}_k dL \quad (\text{A.31})$$

are the magnetic field staggered discretised variables, defined as integrals on the face of cell S_i , while \hat{E}_k^\pm are the magnetic flux components averaged on the oriented boundaries L_k^\pm (the orientation depends from the versor of the face, see Fig. (A.4)). Here the magnetic field components are exactly evaluated in the parallel coordinate i (like in the case of $\hat{\mathbf{f}}_i$), while \hat{E}_k are point values in the orthogonal coordinate $(i, j) \neq k$. This form is known as *semi-analytical* because the time derivatives are left analytical. This staggered discretisation produces a couple of normalised fluxes b_i^\pm , defined on the faces S_i^\pm for all direction

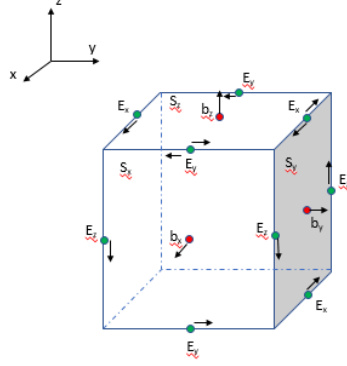


Figure A.4: Staggered vectorial fields in the CT scheme. Only S_x^+ , S_y^+ , S_z^+ faces are shown. The black arrows in the centers of the interfaces, where the b_i components of the magnetic field are defined, indicate the faces versors and their relative oriented boundaries. The electric field vectors are defined in the centers of the boundaries.

i. Using those components it is possible to represent the mean volume of the (parallel) prime derivative $\partial_i B_i(\mathbf{x})$, and then the non-evolutionary solenoidal constraint becomes

$$\Sigma_i \frac{1}{h_i} (\hat{b}_i^+ - \hat{b}_i^-) = 0. \quad (\text{A.32})$$

The numerical form of induction equation eq. (A.22) will preserve this condition during the integration. At this level, everything is an exact solution. Spatial approximations are necessary when all the MHD variables have to be reconstructed at the cell faces, where the fluxes are defined as local values.

Let us define the center point of a cell as (i, j, k) and all the magnetic and electric fields on a cube surface (and then, recursively, on all the others):

- the 5-components vector $\mathbf{u}_{i,j,k}$ is defined in the center of the cell,
- the associated fluxes are defined on the interface of the cell, $\hat{\mathbf{f}}_{x,i+1/2,j,k}$,
- the magnetic field is defined on the interface of the cell too, $\hat{b}_{x,i+1/2,j,k}$,
- the magnetic field's fluxes are defined as 4-states functions on the sides of the cells: $\hat{E}_{y,i-1/2,j\pm 1/2,k}$ and $\hat{E}_{z,i+1/2,j\pm 1/2,k}$.

A.5 Appendix E: free-fall on a star

In this Appendix we derive the metric coefficients for a case of astrophysical interest: the free-fall motion. In this case the metric equations have a fully analytical (although parametric) solution. Consider a fluid element that is free-falling on a star of mass M_* . If r_0 is the position of the fluid element at the starting time $t = 0$ and $u = 0$ is the initial velocity, its velocity in a general position r is

$$u(r) = -u_{\text{ff}} \left(\frac{r_0}{r} - 1 \right)^{1/2}, \quad (\text{A.33})$$

where $u_{\text{ff}} = (2GM/r_0)^{1/2}$. The radius of the fluid element in function of time is given by the parametric solution

$$t = \frac{2}{\pi} (\mu + \sin \mu \cos \mu) t_{\text{ff}}, \quad (\text{A.34})$$

$$r = r_0 \cos^2 \mu, \quad (\text{A.35})$$

$$u = -u_{\text{ff}} \tan \mu, \quad (\text{A.36})$$

where $t_{\text{ff}} = \pi r_0 / 2u_{\text{ff}}$ and μ is a parameter (called *developed angle* running from 0 to $\pi/2$). The fluid element reaches the origin at a time t_{ff} that depends on its initial radius r_0 .

We take a shell that at the initial time $t = 0$ ($\mu = 0$) has an outer radius r_0 and an inner radius $r_0 - \delta r_0$, where $\delta r_0 \ll r_0$. Let us suppose that the outer radius of the shell reaches the star in a time t_{ff} , the inner radius reaches the star at a time $t_{\text{ff}} - \delta t$, that is the time when $\delta t / t_{\text{ff}} \approx -3/2(\delta r_0 / r_0)$. At any time $t(\mu)$, the value of the parameter of the inner side is $\mu + \delta \mu$, where

$$r_0 \delta \mu = \frac{3}{2} \left(\frac{\mu + \sin \mu \cos \mu}{1 + \cos 2\mu} \right) \delta r_0. \quad (\text{A.37})$$

Thus, while the outer radius of the shell is $r_0 \cos^2 \mu$, the inner radius is $(r_0 - \delta r_0) \cos^2(\mu + \delta \mu)$, and the thickness of the shell during collapse is

$$\delta r = \cos \mu \left(\cos \mu + 3 \sin \mu \frac{\mu + \sin \mu \cos \mu}{1 + \cos 2\mu} \right) \delta r_0 = \left(1 + \frac{\sin^2 \mu + 3\mu \tan \mu}{2} \right) \delta r_0. \quad (\text{A.38})$$

We can also give an expression for the radial scale factor $c(t) = \delta r(t) / \delta r_0$, that is then given by

$$c(t) = 1 + \frac{\sin^2 \mu + 3\mu \tan \mu}{2}. \quad (\text{A.39})$$

Due to the fact that the collapse is radial, the transverse scale factor is simply $a(t) =$

$r(t)/r_0$, or

$$a(t) = \cos^2 \mu(t). \quad (\text{A.40})$$

In either case, time t is given by eq. (A.34). These scale factors are shown in Fig. A.5. Thus, a fluid element that is free-falling on a star is stretched in the longitudinal direction and squeezed in the transverse direction.

After some calculation, the rate of radial stretching can be obtained, and it is

$$\frac{\dot{c}}{c} = \frac{3\mu + (3 + 2 \cos^2 \mu) \sin \mu \cos \mu}{t_0 \cos^3 \mu [\cos \mu (4 + \sin^2 \mu) + \sin \mu (6\mu + \sin \mu \cos \mu)]}, \quad (\text{A.41})$$

while the transverse compression rate is

$$\frac{\dot{a}}{a} = \left(\frac{u_{\text{ff}}}{r_0} \right) \frac{\sin \mu}{\cos^3 \mu}. \quad (\text{A.42})$$

These rates are shown in Fig. A.6. When $t \rightarrow t_{\text{ff}}$, expanding to the first order the factors

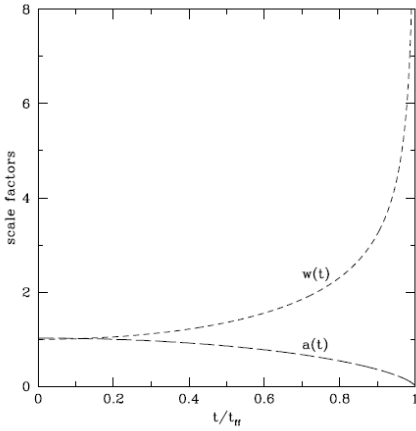


Figure A.5: Longitudinal and transverse scale factors $c(t)$ and $a(t)$ as function of time t .

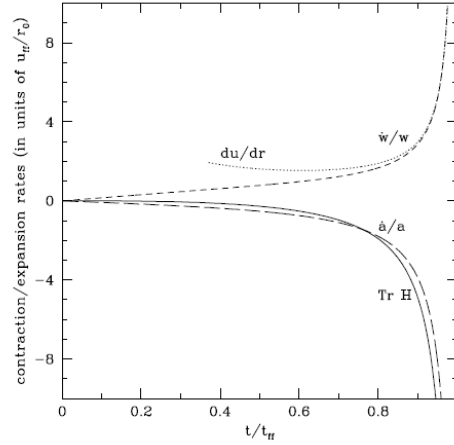


Figure A.6: Longitudinal and transverse contraction/expansion rates \dot{c}/c and \dot{a}/a and $\text{Tr } \mathbb{H} = \dot{c}/c + 2\dot{a}/a$.

and the rates it can be found that

$$r(t) \rightarrow r_0 \left(\frac{3\pi}{4} \right)^{2/3} \left(1 - \frac{t}{t_{\text{ff}}} \right)^{2/3}, \quad (\text{A.43})$$

$$a(t) = b(t) = \left(1 - \frac{t}{t_{\text{ff}}}\right)^{2/3}, \quad c(t) = \left(1 - \frac{t}{t_{\text{ff}}}\right)^{-1/3}, \quad (\text{A.44})$$

and

$$\frac{\dot{a}}{a} \rightarrow -\frac{u_{\text{ff}}}{r_0} \left(1 - \frac{t}{t_{\text{ff}}}\right)^{-1}, \quad \frac{\dot{c}}{c} \rightarrow \frac{u_{\text{ff}}}{2r_0} \left(1 - \frac{t}{t_{\text{ff}}}\right)^{-1}. \quad (\text{A.45})$$

The rate of longitudinal expansion is asymptotically 1/2 of the rate of transversal contraction. Notice that the radial stretching rate \dot{c}/c is asymptotically equal to the radial velocity gradient du/dr .

A.6 Appendix F: Homologous collapse of a pressureless sphere

Let us consider a cloud of mass M and an uniform density ρ_0 that is undergoing a free-fall (pressureless) collapse. The mass $M(r_0)$ contained in a radius r_0 is $M(r_0) = (4\pi/3)\rho_0 r_0^3$, while the free-fall velocity at the same radius r_0 is $u_{\text{ff}} = (8\pi G\rho_0/3)^{1/2}r_0$. The free-fall time is $t_{\text{ff}} = (3\pi/32G\rho_0)^{1/2}$, that is not depending on the initial radius r_0 . For this reason, all the shells arrive at the origin at the same time. The radius of each shell follows the parametric solution eq. (A.34)–(A.35) and the density increases in an uniform way as $\rho = \rho_0/\cos^6 \mu$. We than have that

$$\delta r = \delta r_0 \cos^2 \mu, \quad (\text{A.46})$$

and the contraction is isotropic with scale factors

$$a(t) = b(t) = c(t) = 1 - \sin^2 \mu(t). \quad (\text{A.47})$$

We can find an expression for $H(t) = \dot{a}/a = -\tan \mu/(t_0 \cos^2 \mu)$, where $t_0 = 2t_{\text{ff}}/\pi$.

References

- [Alves et al. 2001] J. F. Alves, C. J. Lada & E. A. Lada, ‘Internal structure of a cold dark molecular cloud inferred from the extinction of background starlight’. *Nature*, January 2001, volume 409, 159–161.
- [André et al. 2014] P. André, J. Di Francesco, D. Ward-Thompson, S.-I. Inutsuka, R. E. Pudritz & J. E. Pineda, ‘From Filamentary Networks to Dense Cores in Molecular Clouds: Toward a New Paradigm for Star Formation’. *Protostars and Planets VI*, 2014, pages 27–51, doi:[10.2458/azu_uapress.9780816531240-ch002](https://doi.org/10.2458/azu_uapress.9780816531240-ch002), arXiv:[1312.6232](https://arxiv.org/abs/1312.6232).
- [Andre et al. 2000] P. Andre, D. Ward-Thompson & M. Barsony, ‘From Prestellar Cores to Protostars: the Initial Conditions of Star Formation’. *Protostars and Planets IV*, May 2000, page 59, arXiv:[astro-ph/9903284](https://arxiv.org/abs/astro-ph/9903284).
- [Arzoumanian et al. 2011] D. Arzoumanian, P. André, P. Didelon, V. Könyves, N. Schneider, A. Men’shchikov, T. Sousbie, A. Zavagno, S. Bontemps, J. di Francesco, M. Griffin, M. Hennemann, T. Hill, J. Kirk, P. Martin, V. Minier, S. Molinari, F. Motte, N. Peretto, S. Pezzuto, L. Spinoglio, D. Ward-Thompson, G. White & C. D. Wilson, ‘Characterizing interstellar filaments with Herschel in IC 5146’. *A&A*, May 2011, volume 529, L6, doi:[10.1051/0004-6361/201116596](https://doi.org/10.1051/0004-6361/201116596), arXiv:[1103.0201](https://arxiv.org/abs/1103.0201).
- [Arzoumanian et al. 2013] D. Arzoumanian, P. André, N. Peretto & V. Könyves, ‘Formation and evolution of interstellar filaments. Hints from velocity dispersion measurements’. *A&A*, May 2013, volume 553, A119, doi:[10.1051/0004-6361/201220822](https://doi.org/10.1051/0004-6361/201220822), arXiv:[1303.3024](https://arxiv.org/abs/1303.3024).
- [Ballesteros-Paredes et al. 2007] J. Ballesteros-Paredes, R. S. Klessen, M.-M. Mac Low & E. Vazquez-Semadeni, ‘Molecular Cloud Turbulence and Star Formation’. *Protostars and Planets V*, 2007, pages 63–80, arXiv:[astro-ph/0603357](https://arxiv.org/abs/astro-ph/0603357).
- [Barnard 1919] E. E. Barnard, ‘On the dark markings of the sky, with a catalogue of 182 such objects.’ *ApJ*, January 1919, volume 49, doi:[10.1086/142439](https://doi.org/10.1086/142439).
- [Bergin & Tafalla 2007] E. A. Bergin & M. Tafalla, ‘Cold Dark Clouds: The Initial Conditions for Star Formation’. *ARA&A*, September 2007, volume 45, 339–396, doi:[10.1146/annurev.astro.45.071206.100404](https://doi.org/10.1146/annurev.astro.45.071206.100404), arXiv:[0705.3765](https://arxiv.org/abs/0705.3765).
- [Bertoldi & McKee 1992] F. Bertoldi & C. F. McKee, ‘Pressure-confined clumps in magnetized molecular clouds’. *ApJ*, August 1992, volume 395, 140–157, doi:[10.1086/171638](https://doi.org/10.1086/171638).

- [Biskamp 2003] D. Biskamp, *Magnetohydrodynamic Turbulence* (2003).
- [Blitz & Shu 1980] L. Blitz & F. H. Shu, ‘The origin and lifetime of giant molecular cloud complexes’. *ApJ*, May 1980, volume 238, 148–157, doi:[10.1086/157968](https://doi.org/10.1086/157968).
- [Bonnor 1956] W. B. Bonnor, ‘Boyle’s Law and gravitational instability’. *MNRAS*, 1956, volume 116, 351, doi:[10.1093/mnras/116.3.351](https://doi.org/10.1093/mnras/116.3.351).
- [Bowyer et al. 1995] S. Bowyer, R. Lieu, S. D. Sidher, M. Lampton & J. Knude, ‘Evidence for a large thermal pressure imbalance in the local interstellar medium’. *Nature*, May 1995, volume 375, 212–214, doi:[10.1038/375212a0](https://doi.org/10.1038/375212a0).
- [Breyse et al. 2014] P. C. Breyse, M. Kamionkowski & A. Benson, ‘Oscillations and stability of polytropic filaments’. *MNRAS*, January 2014, volume 437, 2675–2685, doi:[10.1093/mnras/stt2077](https://doi.org/10.1093/mnras/stt2077), arXiv:[1305.2198](https://arxiv.org/abs/1305.2198).
- [Burgers 1948] J. M. Burgers, ‘A mathematical model illustrating the theory of turbulence’. *Advances in applied mechanics*, 1948, volume 1, 171–199.
- [Carlqvist et al. 1998] P. Carlqvist, H. Kristen & G. F. Gahm, ‘Helical structures in a Rosette elephant trunk’. *A&A*, April 1998, volume 332, L5–L8.
- [Caselli et al. 2002] P. Caselli, P. J. Benson, P. C. Myers & M. Tafalla, ‘Dense Cores in Dark Clouds. XIV. N_2H^+ (1-0) Maps of Dense Cloud Cores’. *ApJ*, June 2002, volume 572, 238–263, doi:[10.1086/340195](https://doi.org/10.1086/340195), arXiv:[astro-ph/0202173](https://arxiv.org/abs/astro-ph/0202173).
- [Caselli & Ceccarelli 2012] P. Caselli & C. Ceccarelli, ‘Our astrochemical heritage’. *A&A Rev.*, October 2012, volume 20, 56, doi:[10.1007/s00159-012-0056-x](https://doi.org/10.1007/s00159-012-0056-x), arXiv:[1210.6368](https://arxiv.org/abs/1210.6368).
- [Caselli et al. 1998] P. Caselli, C. M. Walmsley, R. Terziewa & E. Herbst, ‘The Ionization Fraction in Dense Cloud Cores’. *ApJ*, May 1998, volume 499, 234–249, doi:[10.1086/305624](https://doi.org/10.1086/305624).
- [Chandrasekhar 1951] S. Chandrasekhar, ‘The Gravitational Instability of an Infinite Homogeneous Turbulent Medium’. *Proceedings of the Royal Society of London Series A*, December 1951, volume 210, 26–29, doi:[10.1098/rspa.1951.0228](https://doi.org/10.1098/rspa.1951.0228).
- [Chandrasekhar 1961] S. Chandrasekhar, *Hydrodynamic and hydromagnetic stability* (1961).
- [Chandrasekhar & Fermi 1953] S. Chandrasekhar & E. Fermi, ‘Magnetic Fields in Spiral Arms.’ *ApJ*, July 1953, volume 118, 113, doi:[10.1086/145731](https://doi.org/10.1086/145731).
- [Chiuderi & Velli 2015] C. Chiuderi & M. Velli, *Basics of Plasma Astrophysics* (2015).
- [Crutcher 2012] R. M. Crutcher, ‘Magnetic Fields in Molecular Clouds’. *ARA&A*, September 2012, volume 50, 29–63, doi:[10.1146/annurev-astro-081811-125514](https://doi.org/10.1146/annurev-astro-081811-125514).
- [Crutcher et al. 2010] R. M. Crutcher, B. Wandelt, C. Heiles, E. Falgarone & T. H. Troland, ‘Magnetic Fields in Interstellar Clouds from Zeeman Observations: Inference of Total Field Strengths by Bayesian Analysis’. *ApJ*, December 2010, volume 725, 466–479, doi:[10.1088/0004-637X/725/1/466](https://doi.org/10.1088/0004-637X/725/1/466).
- [Davidovits & Fisch 2017] S. Davidovits & N. J. Fisch, ‘A Lower Bound on Adiabatic Heating of Compressed Turbulence for Simulation and Model Validation’. *ApJ*, April 2017, volume 838, 118, doi:[10.3847/1538-4357/aa619f](https://doi.org/10.3847/1538-4357/aa619f), arXiv:[1612.00063](https://arxiv.org/abs/1612.00063).

- [Del Zanna et al. 2015] L. Del Zanna, L. Matteini, S. Landi, A. Verdini & M. Velli, ‘Parametric decay of parallel and oblique Alfvén waves in the expanding solar wind’. *Journal of Plasma Physics*, January 2015, volume 81(1), 325810102, doi:[10.1017/S0022377814000579](https://doi.org/10.1017/S0022377814000579), arXiv:[1407.5851](https://arxiv.org/abs/1407.5851).
- [Del Zanna et al. 2007] L. Del Zanna, O. Zanotti, N. Bucciantini & P. Londrillo, ‘ECHO: a Eulerian conservative high-order scheme for general relativistic magnetohydrodynamics and magnetodynamics’. *A&A*, October 2007, volume 473, 11–30, doi:[10.1051/0004-6361:20077093](https://doi.org/10.1051/0004-6361:20077093), arXiv:[0704.3206](https://arxiv.org/abs/0704.3206).
- [Dobbs et al. 2014] C. L. Dobbs, M. R. Krumholz, J. Ballesteros-Paredes, A. D. Bolatto, Y. Fukui, M. Heyer, M.-M. M. Low, E. C. Ostriker & E. Vázquez-Semadeni, ‘Formation of Molecular Clouds and Global Conditions for Star Formation’. *Protostars and Planets VI*, 2014, pages 3–26, doi:[10.2458/azu_uapress_9780816531240-ch001](https://doi.org/10.2458/azu_uapress_9780816531240-ch001), arXiv:[1312.3223](https://arxiv.org/abs/1312.3223).
- [Draine 2011] B. T. Draine, *Physics of the Interstellar and Intergalactic Medium* (2011).
- [Dunham et al. 2016] M. M. Dunham, S. S. R. Offner, J. E. Pineda, T. L. Bourke, J. J. Tobin, H. G. Arce, X. Chen, J. Di Francesco, D. Johnstone, K. I. Lee, P. C. Myers, D. Price, S. I. Sadavoy & S. Schnee, ‘An ALMA Search for Substructure, Fragmentation, and Hidden Protostars in Starless Cores in Chamaeleon I’. *ApJ*, June 2016, volume 823, 160, doi:[10.3847/0004-637X/823/2/160](https://doi.org/10.3847/0004-637X/823/2/160), arXiv:[1604.04027](https://arxiv.org/abs/1604.04027).
- [Elmegreen 2000] B. G. Elmegreen, ‘Star Formation in a Crossing Time’. *ApJ*, February 2000, volume 530, 277–281, doi:[10.1086/308361](https://doi.org/10.1086/308361), arXiv:[astro-ph/9911172](https://arxiv.org/abs/astro-ph/9911172).
- [Elmegreen & Elmegreen 1987] B. G. Elmegreen & D. M. Elmegreen, ‘H I superclouds in the inner Galaxy’. *ApJ*, September 1987, volume 320, 182–198, doi:[10.1086/165534](https://doi.org/10.1086/165534).
- [Elmegreen & Scalo 2004] B. G. Elmegreen & J. Scalo, ‘Interstellar Turbulence I: Observations and Processes’. *ARA&A*, September 2004, volume 42, 211–273, doi:[10.1146/annurev.astro.41.011802.094859](https://doi.org/10.1146/annurev.astro.41.011802.094859), arXiv:[astro-ph/0404451](https://arxiv.org/abs/astro-ph/0404451).
- [Falgarone et al. 1992] E. Falgarone, J.-L. Puget & M. Perault, ‘The small-scale density and velocity structure of quiescent molecular clouds’. *A&A*, April 1992, volume 257, 715–730.
- [Fatuzzo & Adams 1993] M. Fatuzzo & F. C. Adams, ‘Magnetohydrodynamic wave propagation in one-dimensional nonhomogeneous, self-gravitating clouds’. *ApJ*, July 1993, volume 412, 146–159, doi:[10.1086/172907](https://doi.org/10.1086/172907).
- [Federrath et al. 2010] C. Federrath, R. Banerjee, P. C. Clark & R. S. Klessen, ‘Modeling Collapse and Accretion in Turbulent Gas Clouds: Implementation and Comparison of Sink Particles in AMR and SPH’. *ApJ*, April 2010, volume 713, 269–290, doi:[10.1088/0004-637X/713/1/269](https://doi.org/10.1088/0004-637X/713/1/269), arXiv:[1001.4456](https://arxiv.org/abs/1001.4456).
- [Federrath et al. 2008] C. Federrath, R. S. Klessen & W. Schmidt, ‘The Density Probability Distribution in Compressible Isothermal Turbulence: Solenoidal versus Compressive Forcing’. *ApJLett*, December 2008, volume 688, L79, doi:[10.1086/595280](https://doi.org/10.1086/595280), arXiv:[0808.0605](https://arxiv.org/abs/0808.0605).

- [Fiege & Pudritz 2000] J. D. Fiege & R. E. Pudritz, ‘Helical fields and filamentary molecular clouds - II. Axisymmetric stability and fragmentation’. *MNRAS*, January 2000, volume 311, 105–119, doi:[10.1046/j.1365-8711.2000.03067.x](https://doi.org/10.1046/j.1365-8711.2000.03067.x), arXiv:[astro-ph/9902385](https://arxiv.org/abs/astro-ph/9902385).
- [Field et al. 1969] G. B. Field, D. W. Goldsmith & H. J. Habing, ‘Cosmic-Ray Heating of the Interstellar Gas’. *ApJLett*, March 1969, volume 155, L149, doi:[10.1086/180324](https://doi.org/10.1086/180324).
- [Fischera & Martin 2012] J. Fischera & P. G. Martin, ‘Estimating distance, pressure, and dust opacity using submillimeter observations of self-gravitating filaments’. *A&A*, November 2012, volume 547, A86, doi:[10.1051/0004-6361/201219728](https://doi.org/10.1051/0004-6361/201219728), arXiv:[1209.4111](https://arxiv.org/abs/1209.4111).
- [Fontani et al. 2016] F. Fontani, B. Commerçon, A. Giannetti, M. T. Beltrán, A. Sánchez-Monge, L. Testi, J. Brand, P. Caselli, R. Cesaroni, R. Dodson, S. Longmore, M. Rioja, J. C. Tan & C. M. Walmsley, ‘Magnetically regulated fragmentation of a massive, dense, and turbulent clump’. *A&A*, September 2016, volume 593, L14, doi:[10.1051/0004-6361/201629442](https://doi.org/10.1051/0004-6361/201629442), arXiv:[1608.08083](https://arxiv.org/abs/1608.08083).
- [Franci et al. 2015] L. Franci, S. Landi, L. Matteini, A. Verdini & P. Hellinger, ‘High-resolution Hybrid Simulations of Kinetic Plasma Turbulence at Proton Scales’. *ApJ*, October 2015, volume 812, 21, doi:[10.1088/0004-637X/812/1/21](https://doi.org/10.1088/0004-637X/812/1/21), arXiv:[1506.05999](https://arxiv.org/abs/1506.05999).
- [Frisch & Bec 2001] U. Frisch & J. Bec, ‘Course 7: “Burgulence”’. In M. Lesieur, A. Yaglom & F. David, editors, *New Trends in Turbulence* (2001) page 341.
- [Galli 2005] D. Galli, ‘On the existence of three-dimensional hydrostatic and magnetostatic equilibria of self-gravitating fluid bodies’. *MNRAS*, May 2005, volume 359, 1083–1095, doi:[10.1111/j.1365-2966.2005.08968.x](https://doi.org/10.1111/j.1365-2966.2005.08968.x), arXiv:[astro-ph/0502584](https://arxiv.org/abs/astro-ph/0502584).
- [Galli et al. 1999] D. Galli, S. Lizano, Z. Y. Li, F. C. Adams & F. H. Shu, ‘Scale-free Equilibria of Isopedic Polytropic Clouds’. *ApJ*, August 1999, volume 521, 630–639, doi:[10.1086/307579](https://doi.org/10.1086/307579), arXiv:[astro-ph/9904028](https://arxiv.org/abs/astro-ph/9904028).
- [Galli et al. 2002] D. Galli, M. Walmsley & J. Gonçalves, ‘The structure and stability of molecular cloud cores in external radiation fields’. *A&A*, October 2002, volume 394, 275–284, doi:[10.1051/0004-6361:20021125](https://doi.org/10.1051/0004-6361:20021125), arXiv:[astro-ph/0208416](https://arxiv.org/abs/astro-ph/0208416).
- [Gehman et al. 1996] C. S. Gehman, F. C. Adams & R. Watkins, ‘Linear Gravitational Instability of Filamentary and Sheetlike Molecular Clouds with Magnetic Fields’. *ApJ*, December 1996, volume 472, 673, doi:[10.1086/178098](https://doi.org/10.1086/178098), arXiv:[astro-ph/9607132](https://arxiv.org/abs/astro-ph/9607132).
- [Gibson et al. 2009] D. Gibson, R. Plume, E. Bergin, S. Ragan & N. Evans, ‘Molecular Line Observations of Infrared Dark Clouds. II. Physical Conditions’. *ApJ*, November 2009, volume 705, 123–134, doi:[10.1088/0004-637X/705/1/123](https://doi.org/10.1088/0004-637X/705/1/123), arXiv:[0908.2643](https://arxiv.org/abs/0908.2643).
- [Glover et al. 2015] S. C. O. Glover, P. C. Clark, M. Micic & F. Molina, ‘Modelling [C I] emission from turbulent molecular clouds’. *MNRAS*, April 2015, volume 448, 1607–1627, doi:[10.1093/mnras/stu2699](https://doi.org/10.1093/mnras/stu2699), arXiv:[1403.3530](https://arxiv.org/abs/1403.3530).
- [Godunov 1959] S. K. Godunov, ‘A difference method for numerical calculation of discontinuous solutions of the equations of hydrodynamics’. *Mat. Sb.*, 1959, volume 47, 271–306.

- [Goldreich & Kwan 1974] P. Goldreich & J. Kwan, ‘Molecular Clouds’. *ApJ*, May 1974, volume 189, 441–454, doi:[10.1086/152821](https://doi.org/10.1086/152821).
- [Goldreich & Sridhar 1995] P. Goldreich & S. Sridhar, ‘Toward a theory of interstellar turbulence. 2: Strong alfvenic turbulence’. *ApJ*, January 1995, volume 438, 763–775, doi:[10.1086/175121](https://doi.org/10.1086/175121).
- [Goldsmith et al. 2008] P. F. Goldsmith, M. Heyer, G. Narayanan, R. Snell, D. Li & C. Brunt, ‘Large-Scale Structure of the Molecular Gas in Taurus Revealed by High Linear Dynamic Range Spectral Line Mapping’. *ApJ*, June 2008, volume 680, 428–445, doi:[10.1086/587166](https://doi.org/10.1086/587166), arXiv:[0802.2206](https://arxiv.org/abs/0802.2206).
- [Gómez & Vázquez-Semadeni 2014] G. C. Gómez & E. Vázquez-Semadeni, ‘Filaments in Simulations of Molecular Cloud Formation’. *ApJ*, August 2014, volume 791, 124, doi:[10.1088/0004-637X/791/2/124](https://doi.org/10.1088/0004-637X/791/2/124), arXiv:[1308.6298](https://arxiv.org/abs/1308.6298).
- [Goodman et al. 1998] A. A. Goodman, J. A. Barranco, D. J. Wilner & M. H. Heyer, ‘Coherence in Dense Cores. II. The Transition to Coherence’. *ApJ*, September 1998, volume 504, 223–246, doi:[10.1086/306045](https://doi.org/10.1086/306045).
- [Goodwin et al. 2004] S. P. Goodwin, A. P. Whitworth & D. Ward-Thompson, ‘Simulating star formation in molecular cores. II. The effects of different levels of turbulence’. *A&A*, August 2004, volume 423, 169–182, doi:[10.1051/0004-6361:20040285](https://doi.org/10.1051/0004-6361:20040285), arXiv:[astro-ph/0405117](https://arxiv.org/abs/astro-ph/0405117).
- [Grappin et al. 2016] R. Grappin, W.-C. Müller & A. Verdini, ‘Alfvén-dynamo balance and magnetic excess in magnetohydrodynamic turbulence’. *A&A*, May 2016, volume 589, A131, doi:[10.1051/0004-6361/201628097](https://doi.org/10.1051/0004-6361/201628097), arXiv:[1603.03559](https://arxiv.org/abs/1603.03559).
- [Grappin & Velli 1996] R. Grappin & M. Velli, ‘Waves and streams in the expanding solar wind’. *J. Geophys. Res.*, January 1996, volume 101, 425–444, doi:[10.1029/95JA02147](https://doi.org/10.1029/95JA02147).
- [Grappin et al. 1991] R. Grappin, M. Velli & A. Mangeney, ‘Alfvénic’ versus ‘standard’ turbulence in the solar wind’. *Annales Geophysicae*, June 1991, volume 9, 416–426.
- [Grappin et al. 1993] R. Grappin, M. Velli & A. Mangeney, ‘Nonlinear wave evolution in the expanding solar wind’. *Physical Review Letters*, April 1993, volume 70, 2190–2193, doi:[10.1103/PhysRevLett.70.2190](https://doi.org/10.1103/PhysRevLett.70.2190).
- [Hacar & Tafalla 2011] A. Hacar & M. Tafalla, ‘Dense core formation by fragmentation of velocity-coherent filaments in L1517’. *A&A*, September 2011, volume 533, A34, doi:[10.1051/0004-6361/201117039](https://doi.org/10.1051/0004-6361/201117039), arXiv:[1107.0971](https://arxiv.org/abs/1107.0971).
- [Heiles & Katz 1976] C. Heiles & G. Katz, ‘The absence of systematic kinematics in dust clouds’. *AJ*, January 1976, volume 81, 37–44, doi:[10.1086/111850](https://doi.org/10.1086/111850).
- [Hennebelle & André 2013] P. Hennebelle & P. André, ‘Ion-neutral friction and accretion-driven turbulence in self-gravitating filaments’. *A&A*, December 2013, volume 560, A68, doi:[10.1051/0004-6361/201321761](https://doi.org/10.1051/0004-6361/201321761), arXiv:[1310.3330](https://arxiv.org/abs/1310.3330).
- [Hennebelle & Falgarone 2012] P. Hennebelle & E. Falgarone, ‘Turbulent molecular clouds’. *A&A Rev.*, November 2012, volume 20, 55, doi:[10.1007/s00159-012-0055-y](https://doi.org/10.1007/s00159-012-0055-y), arXiv:[1211.0637](https://arxiv.org/abs/1211.0637).

- [Henshaw et al. 2017] J. D. Henshaw, I. Jiménez-Serra, S. N. Longmore, P. Caselli, J. E. Pineda, A. Avison, A. T. Barnes, J. C. Tan & F. Fontani, ‘Unveiling the early-stage anatomy of a protocluster hub with ALMA’. *MNRAS*, January 2017, volume 464, L31–L35, doi:[10.1093/mnras/slw154](https://doi.org/10.1093/mnras/slw154), arXiv:[1608.00009](https://arxiv.org/abs/1608.00009).
- [Heyer et al. 2009] M. Heyer, C. Krawczyk, J. Duval & J. M. Jackson, ‘Re-Examining Larson’s Scaling Relationships in Galactic Molecular Clouds’. *ApJ*, July 2009, volume 699, 1092–1103, doi:[10.1088/0004-637X/699/2/1092](https://doi.org/10.1088/0004-637X/699/2/1092), arXiv:[0809.1397](https://arxiv.org/abs/0809.1397).
- [Hopf 1950] E. Hopf, ‘The partial differential equation $ut + uux = xx$ ’. *Communications on Pure and Applied Mathematics*, 1950, volume 3(3), 201–230, doi:[10.1002/cpa.3160030302](https://doi.org/10.1002/cpa.3160030302), URL <http://dx.doi.org/10.1002/cpa.3160030302>.
- [Hoyle 1953] F. Hoyle, ‘On the Fragmentation of Gas Clouds Into Galaxies and Stars.’ *ApJ*, November 1953, volume 118, 513, doi:[10.1086/145780](https://doi.org/10.1086/145780).
- [Iroshnikov 1963] P. S. Iroshnikov, ‘Turbulence of a Conducting Fluid in a Strong Magnetic Field’. *AZh*, 1963, volume 40, 742.
- [Jeans 1902] J. H. Jeans, ‘The Stability of a Spherical Nebula’. *Philosophical Transactions of the Royal Society of London Series A*, 1902, volume 199, 1–53, doi:[10.1098/rsta.1902.0012](https://doi.org/10.1098/rsta.1902.0012).
- [Johnstone et al. 2003] D. Johnstone, J. D. Fiege, R. O. Redman, P. A. Feldman & S. J. Carey, ‘The G11.11-0.12 Infrared-dark Cloud: Anomalous Dust and a Nonmagnetic Isothermal Model’. *ApJLett*, May 2003, volume 588, L37–L40, doi:[10.1086/375524](https://doi.org/10.1086/375524), arXiv:[astro-ph/0303651](https://arxiv.org/abs/astro-ph/0303651).
- [Kawachi & Hanawa 1998] T. Kawachi & T. Hanawa, ‘Gravitational Collapse of Filamentary Clouds’. *PASJ*, December 1998, volume 50, 577–586, doi:[10.1093/pasj/50.6.577](https://doi.org/10.1093/pasj/50.6.577).
- [Kennicutt 1989] R. C. Kennicutt, Jr., ‘The star formation law in galactic disks’. *ApJ*, September 1989, volume 344, 685–703, doi:[10.1086/167834](https://doi.org/10.1086/167834).
- [Keto & Caselli 2010] E. Keto & P. Caselli, ‘Dynamics and depletion in thermally supercritical starless cores’. *MNRAS*, March 2010, volume 402, 1625–1634, doi:[10.1111/j.1365-2966.2009.16033.x](https://doi.org/10.1111/j.1365-2966.2009.16033.x), arXiv:[0908.2400](https://arxiv.org/abs/0908.2400).
- [Keto et al. 2015] E. Keto, P. Caselli & J. Rawlings, ‘The dynamics of collapsing cores and star formation’. *MNRAS*, February 2015, volume 446, 3731–3740, doi:[10.1093/mnras/stu2247](https://doi.org/10.1093/mnras/stu2247), arXiv:[1410.5889](https://arxiv.org/abs/1410.5889).
- [Kirk et al. 2017] H. Kirk, R. K. Friesen, J. E. Pineda, E. Rosolowsky, S. S. R. Offner, C. D. Matzner, P. C. Myers, J. Di Francesco, P. Caselli, F. O. Alves, A. Chacón-Tanarro, H.-H. Chen, M. Chun-Yuan Chen, J. Keown, A. Punanova, Y. M. Seo, Y. Shirley, A. Ginsburg, C. Hall, A. Singh, H. G. Arce, A. A. Goodman, P. Martin & E. Redaelli, ‘The Green Bank Ammonia Survey: Dense Cores under Pressure in Orion A’. *ApJ*, September 2017, volume 846, 144, doi:[10.3847/1538-4357/aa8631](https://doi.org/10.3847/1538-4357/aa8631), arXiv:[1708.05426](https://arxiv.org/abs/1708.05426).
- [Klessen & Glover 2016] R. S. Klessen & S. C. O. Glover, ‘Physical Processes in the Interstellar Medium’. *Star Formation in Galaxy Evolution: Connecting Numerical Models to Reality, Saas-Fee Advanced Course, Volume 43. ISBN 978-3-662-47889-9. Springer-Verlag*

- Berlin Heidelberg, 2016, p. 85, 2016, volume 43, 85, doi:10.1007/978-3-662-47890-5_2, arXiv:1412.5182.*
- [**Kolmogorov 1941**] A. Kolmogorov, ‘The Local Structure of Turbulence in Incompressible Viscous Fluid for Very Large Reynolds’ Numbers’. *Akademiia Nauk SSSR Doklady*, 1941, volume 30, 301–305.
- [**Kraichnan & Nagarajan 1967**] R. H. Kraichnan & S. Nagarajan, ‘Growth of Turbulent Magnetic Fields’. *Physics of Fluids*, April 1967, volume 10, 859–870, doi:10.1063/1.1762201.
- [**Landi et al. 2008**] S. Landi, P. Londrillo, M. Velli & L. Bettarini, ‘Three-dimensional simulations of compressible tearing instability’. *Physics of Plasmas*, January 2008, volume 15(1), 012302, doi:10.1063/1.2825006.
- [**Larson 1981**] R. B. Larson, ‘Turbulence and star formation in molecular clouds’. *MNRAS*, March 1981, volume 194, 809–826, doi:10.1093/mnras/194.4.809.
- [**Li & Shu 1996**] Z.-Y. Li & F. H. Shu, ‘Magnetized Singular Isothermal Toroids’. *ApJ*, November 1996, volume 472, 211, doi:10.1086/178056.
- [**Lizano & Shu 1989**] S. Lizano & F. H. Shu, ‘Molecular cloud cores and bimodal star formation’. *ApJ*, July 1989, volume 342, 834–854, doi:10.1086/167640.
- [**Londrillo & Del Zanna 2000**] P. Londrillo & L. Del Zanna, ‘High-Order Upwind Schemes for Multidimensional Magnetohydrodynamics’. *ApJ*, February 2000, volume 530, 508–524, doi:10.1086/308344, arXiv:astro-ph/9910086.
- [**Londrillo & del Zanna 2004**] P. Londrillo & L. del Zanna, ‘On the divergence-free condition in Godunov-type schemes for ideal magnetohydrodynamics: the upwind constrained transport method’. *Journal of Computational Physics*, March 2004, volume 195, 17–48, doi:10.1016/j.jcp.2003.09.016, arXiv:astro-ph/0310183.
- [**Lynden-Bell 1973**] D. Lynden-Bell, *Sources of Cosmic Power*, page 43 (1973).
- [**Mac Low & Klessen 2004**] M.-M. Mac Low & R. S. Klessen, ‘Control of star formation by supersonic turbulence’. *Reviews of Modern Physics*, January 2004, volume 76, 125–194, doi:10.1103/RevModPhys.76.125, arXiv:astro-ph/0301093.
- [**Mathis et al. 1977**] J. S. Mathis, W. Rumpl & K. H. Nordsieck, ‘The size distribution of interstellar grains’. *ApJ*, October 1977, volume 217, 425–433, doi:10.1086/155591.
- [**McCrea 1957**] W. H. McCrea, ‘The formation of Population I Stars. Part I. Gravitational contraction’. *MNRAS*, 1957, volume 117, 562, doi:10.1093/mnras/117.5.562.
- [**McKee & Holliman 1999**] C. F. McKee & J. H. Holliman, II, ‘Multipressure Polytropes as Models for the Structure and Stability of Molecular Clouds. I. Theory’. *ApJ*, September 1999, volume 522, 313–337, doi:10.1086/307613, arXiv:astro-ph/9903213.
- [**McKee & Ostriker 2007**] C. F. McKee & E. C. Ostriker, ‘Theory of Star Formation’. *ARA&A*, September 2007, volume 45, 565–687, doi:10.1146/annurev.astro.45.051806.110602, arXiv:0707.3514.

- [**McKee & Ostriker 1977**] C. F. McKee & J. P. Ostriker, ‘A theory of the interstellar medium - Three components regulated by supernova explosions in an inhomogeneous substrate’. *ApJ*, November 1977, volume 218, 148–169, doi:[10.1086/155667](https://doi.org/10.1086/155667).
- [**Mestel 1966**] L. Mestel, ‘The magnetic field of a contracting gas cloud. I, Strict flux-freezing’. *MNRAS*, 1966, volume 133, 265, doi:[10.1093/mnras/133.2.265](https://doi.org/10.1093/mnras/133.2.265).
- [**Mininni & Pouquet 2009**] P. D. Mininni & A. Pouquet, ‘Finite dissipation and intermittency in magnetohydrodynamics’. *Phys. Rev. E*, August 2009, volume 80(2), 025401, doi:[10.1103/PhysRevE.80.025401](https://doi.org/10.1103/PhysRevE.80.025401), arXiv:[0903.3265](https://arxiv.org/abs/0903.3265).
- [**Miyama et al. 1987**] S. M. Miyama, S. Narita & C. Hayashi, ‘Fragmentation of Isothermal Sheet-Like Clouds. I —Solutions of Linear and Second-Order Perturbation Equations—’. *Progress of Theoretical Physics*, November 1987, volume 78, 1051–1064, doi:[10.1143/PTP.78.1051](https://doi.org/10.1143/PTP.78.1051).
- [**Mouschovias & Spitzer 1976**] T. C. Mouschovias & L. Spitzer, Jr., ‘Note on the collapse of magnetic interstellar clouds’. *ApJ*, December 1976, volume 210, 326, doi:[10.1086/154835](https://doi.org/10.1086/154835).
- [**Myers & Benson 1983**] P. C. Myers & P. J. Benson, ‘Dense cores in dark clouds. II - NH₃ observations and star formation’. *ApJ*, March 1983, volume 266, 309–320, doi:[10.1086/160780](https://doi.org/10.1086/160780).
- [**Nakamura et al. 1995**] F. Nakamura, T. Hanawa & T. Nakano, ‘Fragmentation of filamentary molecular clouds with longitudinal magnetic fields: Formation of disks and their collapse’. *ApJ*, May 1995, volume 444, 770–786, doi:[10.1086/175650](https://doi.org/10.1086/175650).
- [**Narayanan et al. 2008**] G. Narayanan, M. H. Heyer, C. Brunt, P. F. Goldsmith, R. Snell & D. Li, ‘The Five College Radio Astronomy Observatory CO Mapping Survey of the Taurus Molecular Cloud’. *ApJS*, July 2008, volume 177, 341–361, doi:[10.1086/587786](https://doi.org/10.1086/587786), arXiv:[0802.2556](https://arxiv.org/abs/0802.2556).
- [**Narlikar 2002**] J. V. Narlikar, *An introduction to cosmology* (2002).
- [**Olson & Sachs 1973**] D. W. Olson & R. K. Sachs, ‘The Production of Vorticity in an Expanding, Self-Gravitating Fluid’. *ApJ*, October 1973, volume 185, 91–104, doi:[10.1086/152399](https://doi.org/10.1086/152399).
- [**Orlandi 2000**] P. Orlandi, *Fluid flow phenomena: A numerical toolkit*, volume 55 of *Fluid Mechanics and its Applications*, pages 1–345 (2000), doi:[10.1007/978-94-011-4281-6_1](https://doi.org/10.1007/978-94-011-4281-6_1).
- [**Ostriker 1964a**] J. Ostriker, ‘On the Oscillations and the Stability of a Homogeneous Compressible Cylinder.’ *ApJ*, November 1964a, volume 140, 1529, doi:[10.1086/148057](https://doi.org/10.1086/148057).
- [**Ostriker 1964b**] J. Ostriker, ‘The Equilibrium of Polytropic and Isothermal Cylinders.’ *ApJ*, October 1964b, volume 140, 1056, doi:[10.1086/148005](https://doi.org/10.1086/148005).
- [**Padoan et al. 2001**] P. Padoan, M. Juvela, A. A. Goodman & Å. Nordlund, ‘The Turbulent Shock Origin of Proto-Stellar Cores’. *ApJ*, May 2001, volume 553, 227–234, doi:[10.1086/320636](https://doi.org/10.1086/320636), arXiv:[astro-ph/0011122](https://arxiv.org/abs/astro-ph/0011122).
- [**Padoan & Nordlund 1999**] P. Padoan & Å. Nordlund, ‘A Super-Alfvénic Model of Dark Clouds’. *ApJ*, November 1999, volume 526, 279–294, doi:[10.1086/307956](https://doi.org/10.1086/307956), arXiv:[astro-ph/9901288](https://arxiv.org/abs/astro-ph/9901288).

- [Palau et al. 2017] A. Palau, L. A. Zapata, C. G. Roman-Zuniga, A. Sanchez-Monge, R. Estalella, G. Busquet, J. M. Girart, A. Fuente & B. Commercon, ‘Thermal Jeans fragmentation within 1000 AU in OMC-1S’. *ArXiv e-prints*, June 2017, arXiv:1706.04623.
- [Palmeirim et al. 2013] P. Palmeirim, P. André, J. Kirk, D. Ward-Thompson, D. Arzoumanian, V. Könyves, P. Didelon, N. Schneider, M. Benedettini, S. Bontemps, J. Di Francesco, D. Elia, M. Griffin, M. Hennemann, T. Hill, P. G. Martin, A. Men’shchikov, S. Molinari, F. Motte, Q. Nguyen Luong, D. Nutter, N. Peretto, S. Pezzuto, A. Roy, K. L. J. Rygl, L. Spinoglio & G. L. White, ‘Herschel view of the Taurus B211/3 filament and striations: evidence of filamentary growth?’ *A&A*, February 2013, volume 550, A38, doi:10.1051/0004-6361/201220500, arXiv:1211.6360.
- [Peebles 1980] P. J. E. Peebles, *The large-scale structure of the universe* (1980).
- [Peretto et al. 2014] N. Peretto, G. A. Fuller, P. André, D. Arzoumanian, V. M. Rivilla, S. Bardeau, S. Duarte Puertas, J. P. Guzman Fernandez, C. Lenfestey, G.-X. Li, F. A. Olguin, B. R. Röck, H. de Villiers & J. Williams, ‘SDC13 infrared dark clouds: Longitudinally collapsing filaments?’ *A&A*, January 2014, volume 561, A83, doi:10.1051/0004-6361/201322172, arXiv:1311.0203.
- [Pineda et al. 2010] J. E. Pineda, A. A. Goodman, H. G. Arce, P. Caselli, J. B. Foster, P. C. Myers & E. W. Rosolowsky, ‘Direct Observation of a Sharp Transition to Coherence in Dense Cores’. *ApJLett*, March 2010, volume 712, L116–L121, doi:10.1088/2041-8205/712/1/L116, arXiv:1002.2946.
- [Planck Collaboration 2016] Planck Collaboration, ‘Planck intermediate results. XXXV. Probing the role of the magnetic field in the formation of structure in molecular clouds’. *A&A*, February 2016, volume 586, A138, doi:10.1051/0004-6361/201525896, arXiv:1502.04123.
- [Qian et al. 2012] L. Qian, D. Li & P. F. Goldsmith, ‘¹³CO Cores in the Taurus Molecular Cloud’. *ApJ*, December 2012, volume 760, 147, doi:10.1088/0004-637X/760/2/147, arXiv:1206.2115.
- [Reynolds et al. 1973] R. J. Reynolds, F. Scherb & F. L. Roesler, ‘Observations of Diffuse Galactic HA and [n II] Emission’. *ApJ*, November 1973, volume 185, 869–876, doi:10.1086/152461.
- [Richardson 1920] L. F. Richardson, ‘The Supply of Energy from and to Atmospheric Eddies’. *Proceedings of the Royal Society of London Series A*, July 1920, volume 97, 354–373, doi:10.1098/rspa.1920.0039.
- [Robertson & Goldreich 2012] B. Robertson & P. Goldreich, ‘Adiabatic Heating of Contracting Turbulent Fluids’. *ApJLett*, May 2012, volume 750, L31, doi:10.1088/2041-8205/750/2/L31, arXiv:1203.4815.
- [Rozyczka 1983] M. Rozyczka, ‘3-D simulations of the collapse of nonspherical interstellar clouds’. *A&A*, August 1983, volume 125, 45–51.
- [Schmidt 1959] M. Schmidt, ‘The Rate of Star Formation.’ *ApJ*, March 1959, volume 129, 243, doi:10.1086/146614.

- [Schneider et al. 2010] N. Schneider, T. Csengeri, S. Bontemps, F. Motte, R. Simon, P. Hennebelle, C. Federrath & R. Klessen, ‘Dynamic star formation in the massive DR21 filament’. *A&A*, September 2010, volume 520, A49, doi:[10.1051/0004-6361/201014481](https://doi.org/10.1051/0004-6361/201014481), arXiv:[1003.4198](https://arxiv.org/abs/1003.4198).
- [Shu 1977] F. H. Shu, ‘Self-similar collapse of isothermal spheres and star formation’. *ApJ*, June 1977, volume 214, 488–497, doi:[10.1086/155274](https://doi.org/10.1086/155274).
- [Shu 1992] F. H. Shu, *The physics of astrophysics. Volume II: Gas dynamics*. (1992).
- [Shu et al. 1987] F. H. Shu, F. C. Adams & S. Lizano, ‘Star formation in molecular clouds - Observation and theory’. *ARA&A*, 1987, volume 25, 23–81, doi:[10.1146/annurev.aa.25.090187.000323](https://doi.org/10.1146/annurev.aa.25.090187.000323).
- [Shu et al. 1972] F. H. Shu, V. Milione, W. Gebel, C. Yuan, D. W. Goldsmith & W. W. Roberts, ‘Galactic Shocks in an Interstellar Medium with Two Stable Phases’. *ApJ*, May 1972, volume 173, 557, doi:[10.1086/151444](https://doi.org/10.1086/151444).
- [Soler et al. 2016] J. D. Soler, F. Alves, F. Boulanger, A. Bracco, E. Falgarone, G. A. P. Franco, V. Guillet, P. Hennebelle, F. Levrier, P. G. Martin & M.-A. Miville-Deschênes, ‘Magnetic field morphology in nearby molecular clouds as revealed by starlight and submillimetre polarization’. *A&A*, December 2016, volume 596, A93, doi:[10.1051/0004-6361/201628996](https://doi.org/10.1051/0004-6361/201628996), arXiv:[1605.09371](https://arxiv.org/abs/1605.09371).
- [Solomon et al. 1987] P. M. Solomon, A. R. Rivolo, J. Barrett & A. Yahil, ‘Mass, luminosity, and line width relations of Galactic molecular clouds’. *ApJ*, August 1987, volume 319, 730–741, doi:[10.1086/165493](https://doi.org/10.1086/165493).
- [Stahler & Palla 2005] S. W. Stahler & F. Palla, *The Formation of Stars* (2005).
- [Stepnik et al. 2003] B. Stepnik, A. Abergel, J.-P. Bernard, F. Boulanger, L. Cambrésy, M. Giard, A. P. Jones, G. Lagache, J.-M. Lamarre, C. Meny, F. Pajot, F. Le Peintre, I. Ristorcelli, G. Serra & J.-P. Torre, ‘Evolution of dust properties in an interstellar filament’. *A&A*, February 2003, volume 398, 551–563, doi:[10.1051/0004-6361:20021309](https://doi.org/10.1051/0004-6361:20021309).
- [Stodólkiewicz 1963] J. S. Stodólkiewicz, ‘On the Gravitational Instability of Some Magneto-Hydrodynamical Systems of Astrophysical Interest. Part III.’ *actaa*, 1963, volume 13, 30–54.
- [Tenerani & Velli 2013] A. Tenerani & M. Velli, ‘Parametric decay of radial Alfvén waves in the expanding accelerating solar wind’. *Journal of Geophysical Research (Space Physics)*, December 2013, volume 118, 7507–7516, doi:[10.1002/2013JA019293](https://doi.org/10.1002/2013JA019293).
- [Toalá et al. 2015] J. A. Toalá, E. Vázquez-Semadeni, P. Colín & G. C. Gómez, ‘Inverse Hubble flows in molecular clouds’. *MNRAS*, February 2015, volume 446, 3725–3730, doi:[10.1093/mnras/stu2368](https://doi.org/10.1093/mnras/stu2368), arXiv:[1411.1640](https://arxiv.org/abs/1411.1640).
- [Toci & Galli 2015a] C. Toci & D. Galli, ‘Polytropic models of filamentary interstellar clouds - I. Structure and stability’. *MNRAS*, January 2015a, volume 446, 2110–2117, doi:[10.1093/mnras/stu2168](https://doi.org/10.1093/mnras/stu2168), arXiv:[1410.6091](https://arxiv.org/abs/1410.6091).

- [**Toci & Galli 2015b**] C. Toci & D. Galli, ‘Polytropic models of filamentary interstellar clouds - II. Helical magnetic fields’. *MNRAS*, January 2015b, volume 446, 2118–2124, doi:[10.1093/mnras/stu2194](https://doi.org/10.1093/mnras/stu2194), arXiv:[1410.6092](https://arxiv.org/abs/1410.6092).
- [**Toci et al. 2017**] C. Toci, D. Galli, A. Verdini, L. Del Zanna & S. Landi, ‘Sub-structure formation in starless cores’. *ArXiv e-prints*, October 2017, arXiv:[1710.09124](https://arxiv.org/abs/1710.09124).
- [**Tohline 1980**] J. E. Tohline, ‘The gravitational fragmentation of primordial gas clouds’. *ApJ*, July 1980, volume 239, 417–427, doi:[10.1086/158125](https://doi.org/10.1086/158125).
- [**Vazquez-Semadeni 2012**] E. Vazquez-Semadeni, ‘Physical Processes of Interstellar Turbulence’. *ArXiv e-prints*, February 2012, arXiv:[1202.4498](https://arxiv.org/abs/1202.4498).
- [**Vázquez-Semadeni et al. 1998**] E. Vázquez-Semadeni, J. Cantó & S. Lizano, ‘Does Turbulent Pressure Behave as a Logatropé?’ *ApJ*, January 1998, volume 492, 596–602, doi:[10.1086/305064](https://doi.org/10.1086/305064), arXiv:[astro-ph/9708148](https://arxiv.org/abs/astro-ph/9708148).
- [**Vázquez-Semadeni et al. 2010**] E. Vázquez-Semadeni, P. Colín, G. C. Gómez, J. Ballesteros-Paredes & A. W. Watson, ‘Molecular Cloud Evolution. III. Accretion Versus Stellar Feedback’. *ApJ*, June 2010, volume 715, 1302–1317, doi:[10.1088/0004-637X/715/2/1302](https://doi.org/10.1088/0004-637X/715/2/1302), arXiv:[1001.0802](https://arxiv.org/abs/1001.0802).
- [**Verdini & Grappin 2016**] A. Verdini & R. Grappin, ‘Beyond the Maltese Cross: Geometry of Turbulence Between 0.2 and 1 au’. *ApJ*, November 2016, volume 831, 179, doi:[10.3847/0004-637X/831/2/179](https://doi.org/10.3847/0004-637X/831/2/179), arXiv:[1609.09094](https://arxiv.org/abs/1609.09094).
- [**Viala & Horedt 1974a**] Y. Viala & G. P. Horedt, ‘Emden’s functions for polytropes with negative index’. *A&AS*, August 1974a, volume 16, 173.
- [**Viala & Horedt 1974b**] Y. P. Viala & G. Horedt, ‘Polytropic Sheets, Cylinders and Spheres with Negative Index’. *A&A*, July 1974b, volume 33, 195.
- [**Walén 1944**] C. Walén, ‘On the Theory of Sunspots’. *Arkiv for Astronomi*, 1944, volume 30, 1–87.
- [**Whitworth & Ward-Thompson 2001**] A. P. Whitworth & D. Ward-Thompson, ‘An Empirical Model for Protostellar Collapse’. *ApJ*, January 2001, volume 547, 317–322, doi:[10.1086/318373](https://doi.org/10.1086/318373), arXiv:[astro-ph/0009325](https://arxiv.org/abs/astro-ph/0009325).
- [**Williams et al. 2000**] J. P. Williams, L. Blitz & C. F. McKee, ‘The Structure and Evolution of Molecular Clouds: from Clumps to Cores to the IMF’. *Protostars and Planets IV*, May 2000, page 97, arXiv:[astro-ph/9902246](https://arxiv.org/abs/astro-ph/9902246).
- [**Wilson et al. 1970**] R. W. Wilson, K. B. Jefferts & A. A. Penzias, ‘Carbon Monoxide in the Orion Nebula’. *ApJLett*, July 1970, volume 161, L43, doi:[10.1086/180567](https://doi.org/10.1086/180567).
- [**Ysard et al. 2013**] N. Ysard, A. Abergel, I. Ristorcelli, M. Juvela, L. Pagani, V. Könyves, L. Spencer, G. White & A. Zavagno, ‘Variation in dust properties in a dense filament of the Taurus molecular complex (L1506)’. *A&A*, November 2013, volume 559, A133, doi:[10.1051/0004-6361/201322066](https://doi.org/10.1051/0004-6361/201322066), arXiv:[1309.6489](https://arxiv.org/abs/1309.6489).